Dissertation

submitted to the

Combined Faculties for the Natural Sciences and for Mathematics

of the Ruperto-Carola University of Heidelberg, Germany

for the degree of

Doctor of Natural Sciences

Presented by

M.Sc. Mahshid Helia Saber

born in: Shiraz, Iran

Oral examination: June 18th, 2020

Investigation of the physiological role of the electrically silent K2P subunit Task5 in the auditory brainstem

Referees: Prof. Dr. Thomas Kuner
Prof. Dr. Christoph Schuster

Abstract

The TWIK-related acid-sensitive potassium channel 5 (Task5) is a two-pore domain potassium channel (K2P) member. This potassium channel family forms leak channels, which are crucial for the setting of the resting membrane potential (RMP) and neuronal excitability. K2P channels are widely distributed throughout the body and are involved in a variety of biological functions such as ion homeostasis, neuroprotection and tumor progression. Shortly after its identification 19 years ago, Task5 was labeled as non-functional due to its lack of channel activity in heterologous expression systems. Among the K2P family members, Task5 has a very special expression pattern, as it is almost exclusively expressed within the auditory brainstem. In consideration of Task5's restriction to auditory neurons, its upregulation during postnatal development and its deafness-associated downregulation, it appears quite probable that Task5 acts in developmental processes required for mature firing properties within the auditory brainstem circuitry and thus proper processing of auditory information.

The present work investigated the physiological role of Task5 within two prominent auditory brainstem nuclei, the ventral cochlear nucleus (VCN) and the medial nucleus of the trapezoid body (MNTB). Special attention was laid on the functional relevance of Task5 in the regulation of neuronal excitability. To address this issue, the level of Task5 expression was manipulated either by its constitutive knockout or acute shRNA-mediated knockdown restricted to the VCN or the MNTB. Investigations were carried out mostly using various electrophysiological techniques. ShRNA-mediated knockdown showed a role for Task5 in contributing to the phasic firing pattern in VCN neurons, the RMP, cell excitability and regulation of the action potential (AP) waveform. Furthermore, we confirmed the developmental upregulation of Task5 around hearing onset in the VCN as well as in the MNTB. Interestingly and rather surprisingly, the results could not be replicated in constitutive Task5-knockout (KO) mice. Neurons in these mice were able to compensate for the loss of Task5 by adjusting their ion channel expression profile. However, Task5-KO mice showed alterations in auditory processing as shown by auditory brainstem recordings (ABRs). Furthermore, synaptic transmission at the endbulbs of Held, the output synapses of the auditory nerve (AN), was altered. Both results suggested independently of each other a perturbed signal propagation from the AN to the cochlear nucleus.

These results suggest that Task5, despite its lack of channel activity in heterologous expression systems, performs an important function in physiological settings. Task5 contributes to the regulation of neuronal excitability, spike width, the establishment of the typical firing pattern of auditory neurons and the ultra-precise synaptic transmission. It can thus be concluded that Task5 plays an important role in the processing of auditory stimuli in the central auditory system.

Zusammenfassung

Der TWIK-related acid-sensitive Kaliumkanal 5 (Task5) gehört zu der Familie der Zwei-Porendomänen-Kaliumkanäle (K2P), einer Kaliumkanalfamilie, die Leckkanäle bildet, die im Bereich des Ruhemembranpotentials erregbarer Zellen geöffnet sind. Damit spielen diese Kaliumkanäle eine entscheidende Rolle bei der Einstellung des Ruhemembranpotentials und der neuronalen Erregbarkeit. K2P-Kanäle sind im gesamten Körper weit verbreitet und besitzen neben den oben genannten eine Vielzahl weiterer biologischer Funktionen, wie z.B. Ionenhomöostase, Neuroprotektion und Tumorprogression. Task5 wurde vor zwei Jahrzehnten identifiziert. Da aber keine Ionenkanalaktivität in heterologen Expressionssystemen nachgewiesen werden konnte, ließ das Interesse an Task5 stark nach, sodass seine Funktion bis heute nicht bekannt ist. Eine Besonderheit von Task5 innerhalb der K2P-Familie ist seine sehr spezifische Expression im zentralen Nervensystem, die fast ausschließlich auf die Kerne des auditorischen Hirnstamms bis zu den Colliculi inferiores beschränkt ist. In Anbetracht der Beschränkung des Task5-Vorkommens auf Neurone des auditorischen Systems, seiner Hochregulierung während der Erlangung der auditorischen Wahrnehmung sowie seiner Herunterregulierung bei Taubheit, erscheint es sehr wahrscheinlich, dass die physiologische Rolle von Task5 stark mit der Verarbeitung auditorischer Sinneseindrücke verknüpft ist. Eine besondere Rolle spielt hierbei die Etablierung der ultraschnellen und ultrapräzisen Signalverarbeitung.

Die vorliegende Arbeit untersuchte die physiologische Rolle von Task5 innerhalb des ventralen Nucleus cochlearis (VCN) und des medialen Kerns des Trapezkörpers (MNTB), zwei prominenten auditorischen Hirnstammkernen. Ein besonderer Schwerpunkt wurde auf die funktionelle Relevanz von Task5 für die Regulation der neuronalen Erregbarkeit, und daraus resultierend auf das Feuerverhalten der auditorischen Neurone gelegt. Hierzu wurde der Grad der Task5-Expression mit zwei verschiedenen genetischen Methoden verändert. Zum einen wurde eine konstitutive Knockoutmaus generiert, in der Task5 zu keinem Zeitpunkt exprimiert wird, zum anderen wurde die Task5-Expression durch einen shRNA-vermittelten Knockdown akut und nur innerhalb der beiden untersuchten Hirnstamm Nuclei vermindert. Für funktionelle Untersuchungen wurden hauptsächlich elektrophysiologische Methoden eingesetzt. Durch akute Verminderung der Task5-Expression mittels shRNA, konnte gezeigt werden, dass Task5 beim Einstellen der Erregbarkeit der Zellen, der Regulierung der Breite der Aktionspotentiale (AP) und

der Etablierung des phasischen Feuerverhaltens in VCN Neuronen eine entscheidende Rolle spielt. Außerdem konnte die Hochregulierung von Task5 mRNA zum Zeitpunkt des Hörbeginns in beiden untersuchten Hirnstammkernen bestätigt werden. Interessanterweise und eher überraschend konnten diese Effekte bei einem völligen Fehlen von Task5 in den Neuronen der konstitutiven Task5-Knockoutmäuse nicht reproduziert werden. Viel mehr waren diese Neurone in der Lage, den Verlust von Task5 durch Anpassung ihres Ionenkanalexpressionsmusters zu kompensieren. Trotzdem konnten Effekte des Knockouts von Task5 auf die Verarbeitung auditorischer Signale mittels „Auditory brainstem response"-Messung (ABR) gezeigt werden. Außerdem zeigten Task5-Knockoutmäuse eine Störung der Transmission an den Ausgangssynapsen des Nervus cochlearis, die den sogenannten Held'schen Endbulbi, zugeordnet werden. Beide Ergebnisse deuten unabhängig voneinander auf eine Veränderung der Verbindungsbahn vom Hörnerv zum Nucleus cochlearis hin.

Diese Ergebnisse lassen darauf schließen, dass Task5, trotz seiner fehlenden Kanalfunktion in heterologen Expressionssystemen, im physiologischen Kontext eine wichtige Funktion ausübt. Task5 trägt zur Regulierung der neuronalen Erregbarkeit, der Breite der APs, der Etablierung des typischen Feuerverhaltens auditorischer Neurone und der ultrapräzisen synaptischen Übertragung bei. Damit spielt es eine wichtige Rolle bei der Verarbeitung auditorischer Wahrnehmungen im zentralen auditorischen System.

Declaration

I, Mahshid Helia Saber, hereby declare that the work in this thesis represents my original research results. The thesis has been written by myself using the references and resources indicated. Any work of other has been appropriately marked. The work has been conducted under the supervision of Prof. Dr. Thomas Kuner and Dr. Christoph Körber at the Institute of Anatomy and Cell Biology, Department of Functional Neuroanatomy, Medical Faculty, Heidelberg University, Germany.

This thesis is being submitted for the degree of Doctor of Natural Sciences at Heidelberg University, Germany, and has not been presented to any other university as part of an examination or degree.

Heidelberg, ...

Mahshid Helia Saber

Abbreviations

AAV	adeno-associated virus
ABR	auditory brainstem recording
ACSF	artificial cerebrospinal fluid
AN	auditory nerve
ANR	auditory nerve root
AP	action potential
ATP	adenosine-5'-triphosphate
AUC	area under the curve
AVCN	anteroventral cochlear nucleus
CAG	cytomegalovirus early enhancer/chicken β actin
CN	cochlear nucleus
DIV	days *in vitro*
DMEM	Dulbecco's Modified Eagle's Medium
DPOAE	distortion product otoacoustic emission
EGFP	enhanced green fluorescent protein
EPSC	excitatory postsynaptic current
ER	endoplasmic reticulum
ES	embryonic stem
f-ABR	frequency-specific-evoked ABR
FCS	fetal calve serum
FISH	Fluorescence *in situ* hybridization
FWHM	full-width-at-half maximum
GBC	globular bushy cell
HCN	hyperpolarization-activated cyclic nucleotide-gated cation channel
HEK	human embryonic kidney
ILD	interaural level difference
I/O	input/output

ITD	interaural time difference
ITR	inverted terminal repeats
I-V	current-voltage
K2P	Two-pore domain potassium channel
KD	knockdown
KO	knockout
Kv	voltage-gated potassium channel
LSO	lateral superior olive
MNTB	medial nucleus of the trapezoid body
MSO	medial superior olive
NGS	normal goat serum
P	postnatal day
P1	first pore-forming domain
P2	second pore-forming domain
PBS	Phosphate Buffered Saline
PDI	Protein disulfide isomerase
P-domain	pore-forming domain
PEI	polyethylenimine
PFA	paraformaldehyde
PPR	paired pulse ratio
RMP	Resting membrane potential
RRP	readily releasable pool
RT	room temperature
RT-PCR	real-time polymerase chain reaction
SD	standard deviation
SEM	standard error of the mean
shRNA	short hairpin RNA
SOC	superior olivary complex
SPL	sound pressure level

STD	short-term depression
Task5	TWIK-related acid-sensitive potassium channel 5
TGN	trans golgi network
TM	transmembrane domain
TTX	Tetrodotoxin
VCN	ventral cochlear nucleus
V-I	voltage-current
WPRE	Woodchuck Hepatitis Virus Posttranscriptional Regulatory Element
WT	wild-type

Table of content

1. Introduction

Sensory information processing is a fundamental task of the brain. To accomplish this task accurately, neural circuits with their unique set of specialized neuronal subtypes are a prerequisite. A particularly interesting model system for studying precise and ultrafast sensory information processing is the mammalian central auditory system. One task of the auditory system is sound localization, which is indispensable for predator and prey in the animal kingdom in terms of spatial orientation and survival, but also just as important for us humans to navigate and communicate. In order to carry out sound source localization, the auditory system is capable of detecting time differences of arriving sound at the two ears with sub-millisecond precision. Simultaneous processing of inhibitory- and excitatory signals and the spatial arrangement of these inputs enables ultrafast computation of the location of sound. The present study deals with this complex system to unravel some of its unsolved mysteries.

1.1. The mammalian auditory system

1.1.1. The central auditory pathway

The mammalian auditory system consists of the peripheral structures of the outer ear, middle ear, and inner ear and the central auditory system, namely the ascending auditory pathway terminating in the auditory cortex. The AN relays information from the peripheral auditory system to central auditory nuclei, which include the cochlear nucleus (CN), the superior olivary complex (SOC), the lateral lemniscus, the inferior colliculus and the medial geniculate nuclei (Felix et al., 2018). The ascending auditory pathway transmits acoustic information to the auditory cortex for further processing (Warrier et al., 2009). The auditory brainstem represents the first stage of information processing with the SOC being the first stage receiving converging input from both ears (Wernick and Starr, 1968). In the SOC, a clear distinction can be made between three well-structured primary nuclei, the medial- and lateral superior olive (MSO and LSO) and the MNTB. The interaction between this set of nuclei enables accurate sound localization. Interaural level differences (ILD) and interaural time differences (ITD) are the two most important binaural cues for sound source localization. It is well known that MSO neurons encode ITDs, whereas neurons in the LSO detect ILDs. To do so, precisely timed inhibition is a prerequisite for guaranteeing ultrafast acoustic information processing. Inhibition is provided by the MNTB, which converts incoming excitatory input from the contralateral ear into precisely timed inhibition. Together,

these four nuclei represent the early stage of the ascending auditory pathway, initiating "binaural communication" via the CN-to-contralateral-MNTB connection.

1.1.2. Globular bushy cells in the anteroventral cochlear nucleus (AVCN)

The CN represents the first processing station of acoustic information in the mammalian central auditory system. Information coming from the inner ear is transmitted to AN fibers, which convey the incoming information to the CN. Based on cytoarchitecture, the CN is subdivided into the dorsal- and ventral cochlear nucleus (DCN and VCN, respectively). The VCN can be further divided into two major parts, the posteroventral- and the anteroventral cochlear nucleus (Harrison and Warr, 1962). The neuron population in the AVCN consists of a heterogeneous population of several different cell types (Osen, 1969). The two main types are stellate- and bushy cells. As indicated by the name, bushy cells typically have a short, highly branched dendritic tree architecture (Rhode et al., 1983) and are categorized into spherical- and globular bushy cells (SBCs and GBCs), based on the shape of their soma (Smith et al., 1993). GBCs receive numerous excitatory inputs from the so-called modified endbulbs of Held (Harrison and Irving, 1965; Spirou et al., 2005), which arise from the AN fibers. These nerve terminals represent the first synapse within the central auditory system and are among the largest nerve terminals in the mammalian brain (O'Neil et al., 2011). The endbulb of Held terminals form axosomatic synapses on the postsynaptic GBC and transmit acoustic information with high-fidelity and temporal precision (Nicol and Walmsley, 2002). In order that GBCs elicit an AP, multiple subthreshold synaptic inputs from AN fibers must coincide (Rothman et al., 1993). Due to the convergence of incoming input from multiple AN fibers, the temporal precision of APs elicited by GBCs is enhanced and exceeds that from single AN fibers (Rothman et al., 1993).

In vitro experiments at the endbulb-GBC synapse revealed activity-dependent synaptic short-term depression (STD) with the level of depression being dependent on the applied stimulation frequency. This form of synaptic plasticity is suggested to occur due to presynaptic neurotransmitter depletion (Yang and Xu-Friedman, 2008; Friauf et al., 2015). It is believed that synaptic depression at the endbulb-GBC synapses serves to preserve temporal precision and might even contribute to increased precision (Yang and Xu-Friedman, 2009). GBCs send excitatory axonal projections to the contralateral MNTB, forming an axosomatic synapse onto the glycinergic MNTB neurons. This GBC-to-MNTB pathway creates a fundamental basis for the temporal precision, for which the central auditory system is well known for (Fig. 1).

1.1.3. The medial nucleus of the trapezoid body

The synaptic endings that rise from the contralateral GBCs, are well-known as the calyces of Held, probably the largest synaptic terminal in the mammalian central nervous system (Schneggenburger and Forsythe, 2006). The large size enables the calyx to contain hundreds of active zones with a high total number of readily releasable docked vesicles (Borst and Soria v. Hoeve, 2012), meeting the conditions needed to rapidly depolarize MNTB cells via high-frequency signaling. Anatomical studies revealed that each MNTB cell receives a single calyx synapse, which covers wide parts of the MNTB principal cell's surface (Sätzler et al., 2002; von Gersdorff and Borst, 2002; Bergsman et al., 2004). The MNTB converts the contralateral excitatory input into glycinergic inhibition to the ipsilateral MSO and LSO (Grothe et al., 1992; Grothe et al., 2010), forming the basis for binaural sound source localization. Furthermore, literature provides evidence that the MNTB not only receives input from its major excitatory input, the calyx of Held, but also excitatory- and inhibitory input of non-calyceal origin (Hamann et al., 2003; Awatramani et al., 2004). The cell population in the MNTB is homogenous, consisting of the MNTB principal cells only (Zook and DiCaprio, 1988). The MNTB principal cells have round cell bodies and appear to have rather short dendrites. Of note, the existence of the MNTB in humans was questioned for a long time, raising questions about the general concept of sound localization. However, evidence was recently provided for the existence of a human MNTB (Richter et al., 1983; Kulesza and Grothe, 2015).

1.1.4. Development of intrinsic neuronal properties of the auditory system

Before the onset of hearing, the circuitry for transmitting acoustic information already exists in the auditory brainstem. At this pre-hearing stage, the developing auditory system is driven by

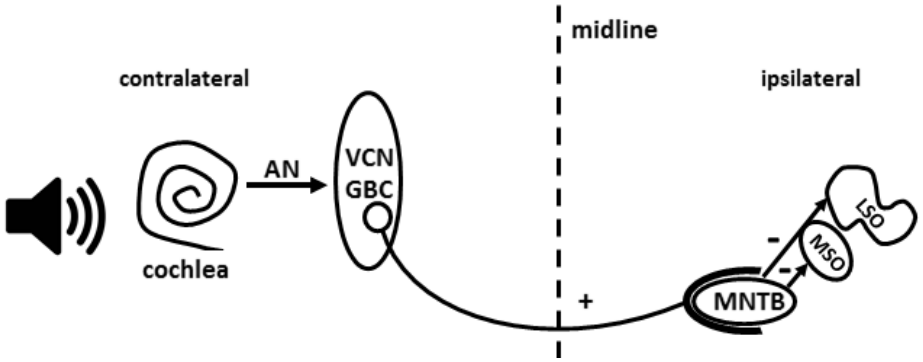

Figure 1: Schematic drawing of the connections in the auditory brainstem.
AN: auditory nerve, VCN: ventral cochlear nucleus, MNTB: medial nucleus of the trapezoid body; MSO: medial superior olive, LSO: lateral superior olive. Excitatory input is shown with plus (+) sign, inhibitory inputs are indicated by minus (-) sign.

spontaneous activity. Spontaneous release of Adenosine-5'-triphosphate (ATP) is thought to initiate waves of neuronal activity in the cochlea that travel through the auditory system all the way up to the inferior colliculus. These waves support neuronal survival and functional refinement of the central auditory pathway (Tritsch et al., 2007). This spontaneous activity is limited to the pre-sensory phase when auditory input is yet absent. When the ear canal opens around postnatal day (P) 12 (Anthwal and Thompson, 2016), defined as the time of hearing onset, the auditory system becomes susceptible to sound stimulation. During hearing onset, spontaneous ATP-dependent signaling diminishes almost completely (Tritsch et al., 2007). After hearing onset, neurons within the central auditory pathway are already equipped with mature-like firing properties. However, they are still undergoing functional "refinement", ensuring auditory fine-tuning of the synaptic network at least till the end of the third postnatal week (Nothwang et al., 2015).

During postnatal maturation of auditory brainstem nuclei, passive and active properties such as RMP, input resistance and spike onset undergo marked changes until mature-like properties are established right before hearing onset. These intrinsic membrane properties determine the neuronal firing behavior (Kandler and Friauf, 1995; Hoffpauir et al., 2010; Franzen et al., 2015). For example, the input resistance becomes lower during development, most likely due to increased cell size (Wu and Oertel, 1987), which supports precisely-timed integration. Furthermore, RMP and AP firing properties undergo changes due to a developmental redistribution of voltage-gated potassium channels (Gittelman and Temple, 2006; Johnston et al., 2010). Thus, these neuronal modifications in the auditory brainstem, during the first two postnatal weeks, tune response properties and promote high-fidelity transmission, one of the most defining features of the auditory brainstem.

Adult-like mono-innervation of MNTB principal cells by the calyx of Held, hence the establishment of a mature-like GBC-MNTB pathway, occurs during early postnatal development between P2 and P4 (Hoffpauir et al., 2006). From that point onwards, the calyx undergoes substantial changes, transforming into the well-known highly fenestrated structure. This characteristic morphological maturation occurs during early postnatal life and reaches mature-like dynamics shortly after hearing onset (Hoffpauir et al., 2006; Sonntag et al., 2011; Nakamura and Cramer, 2011). Concurrently with the transformation of the calyx, the VCN and MNTB neurons undergo functional maturation, establishing mature biophysical properties around P14 in

rodents (Wu and Oertel, 1987; Hoffpauir et al., 2010). By the onset of hearing, these neurons have undergone the transition from multiple AP-firing to the characteristic single spike onset firing (Wu and Oertel, 1984; Banks and Smith, 1992; Hoffpauir et al., 2010). Moreover, AP shortening is a common feature during the maturation of biophysical properties, enabling high-frequency firing. Also, the RMP reaches more hyperpolarized values while AP amplitude decreases, exhibiting undershoot APs (Wu and Oertel, 1987; Hoffpauir et al., 2010). The latter is particularly characteristic of GBCs in the AVCN. These functional changes are caused by developmental modulation of both, sodium and potassium channels, on a molecular level. Furthermore, increasing postnatal expression of "leak channels", as well as low- and high voltage-activated potassium channels, are associated with the acquisition of mature AP kinetics (Hoffpauir et al., 2010; Rusu and Borst, 2011; Müller et al., 2019). The mixed subset of potassium channel types has major impact on mature biophysical properties of auditory brainstem neurons, promoting ultrafast and temporally precise transmission, which is a prerequisite for proper sound source localization. The nature and extent of potassium channels, influencing the way neurons in central auditory nuclei respond to stimuli, is described in more detail hereafter.

1.2. Potassium channels

Ion channels enable extremely fast flow of about 10^6 - 10^8 ions per second through the cell membrane (Egger and Feldmeyer, 2013), making them the fastest transporters across the cell membrane. They can be further categorized as anion-, cation- and non-selective ion channels. Moreover, they are expressed in all cells and cell organelles, providing ion homeostasis required for various cellular processes. Selectivity for one type of ion enables fundamental biological functions such as the generation and propagation of APs in neurons. This selective membrane permeability is the basis for the maintenance of the negative membrane potential, mainly due to the relatively high basal potassium permeability of the plasma membrane (Wright, 2004; Enyedi and Czirják, 2010), leading to high inside and low outside concentrations of potassium ions. Due to high potassium permeability, the RMP of excitable cells is close to the equilibrium potential of potassium. The RMP can vary between different cell types as different cell types express different repertoires of ion channels. Typically, the RMP in neurons ranges between -60 and -80 mV. The largest group among the ion channels are the potassium-selective channels, which are encoded by more than 80 genes in the human genome (Amin and Wilde, 2016). Additionally, their functional diversity is increased by heteromerization, splice variants and regulatory subunits

(Jentsch, 2000; Gutman et al., 2005). This outstanding diversity indicates the high importance of potassium channels with fine-tuned biophysical properties for proper cellular function. Based on sequence homology and function, potassium channels can be subdivided into voltage-gated- (Kv), calcium-activated- (KCa), inwardly-rectifying- (Kir) and two-pore domain (K2P) potassium channels (Guéguinou et al., 2014). These channels contain two- (Kir), four- (K2P) or six- (Kv, KCa) transmembrane domains (TMs) (Patel and Honoré, 2001; Kuang et al., 2015). The four potassium channel families exhibit substantial differences in their biophysical- and pharmacological properties, regulation and tissue distribution.

Research has provided insight into the importance of potassium channels in setting the response characteristics of neurons in central auditory nuclei. Response properties of GBCs in the AVCN can be largely ascribed to the properties of their voltage-gated potassium channels (Oertel, 1991; Manis and Marx, 1991; Trussell, 1999). The composition of potassium channels enables GBCs to respond with high-fidelity to the incoming acoustic information from the peripheral auditory system, which is encoded by APs at high-frequency. The communication between GBCs in the AVCN and MNTB principal cells is one example for the importance of potassium channels in the auditory brainstem. The preservation of precisely timed transmission of acoustic information within this pathway is assured, as GBCs and MNTB neurons can spike at high rates (Wu and Kelly, 1993; Roberts et al., 2014). These APs are phase-locked to sinusoidal auditory stimuli at frequencies of up to ~ 5-6 kHz in mammals (Rothman et al., 1993; Kopp-Scheinpflug et al., 2003). This high-frequency activity is mainly achieved by high voltage-activated potassium channels of the Kv3 family, which shorten AP duration and enable high-frequency activity due to rapid repolarization and thus limited time of voltage-gated sodium channels in the inactivated state (Brew and Forsythe, 1995).

In addition to the Kv3 family, low voltage-activated Kv1 channels were found to shape the release pattern of neurons in auditory brainstem nuclei by limiting the firing of the neuron to only one or few APs at the onset of the cell depolarization, enabling temporal precision required for phase-locking and the detection of coincident activity underlying spatial hearing (Manis and Marx, 1991; Oertel, 1999; Trussel, 1999; Huguet et al., 2017).

The involvement of K2P members in setting the RMP and consequently determining the distance to the threshold-potential for APs, is another example of how potassium channels control the cell's electrical properties.

In summary, neuronal electrical characteristics are determined to a large extend by the types of potassium channels present. These channels affect most of the cell's biophysical and electrophysiological properties such as firing pattern, intrinsic membrane properties, RMP and AP waveform.

1.3. Two-pore domain potassium channels

In 1995, the yeast potassium channel TOK1 (YORK) was the first cloned channel, showing the two pore-forming domains, which today are known as defining features of K2Ps (Ketchum et al., 1995; Lesage et al., 1996a). In addition to the two pore-forming domains (P-domain), TOK1 comprised eight TMs (2P/8TM). Shortly after, ORK1 was cloned from *Drosophila melanogaster*, likewise displaying two P-domains, but only four TMs (Goldstein et al., 1996). The first mammalian K2P, TWIK1, was identified the same year with the characteristic 2P/4TM structure (Lesage et al., 1996b). To date, 15 mammalian K2P channels have been described, which are encoded by the KCNK genes (KCNK1-18). Based on sequence homology, their regulatory mechanisms and their electrophysiological properties, they were further subdivided in the six subfamilies TWIK, THIK, TASK, TREK, TALK and TRESK (Djillani et al., 2019). In addition to the 2P/4TM-structure, K2P channels exhibit a relatively short intracellular amino- and a more extended intracellular carboxyl terminus. The first two TMs (M1 and M2) are connected via a long extracellular loop, which also contains the first P-domain (P1). The second P-domain (P2) is found in the second loop between M3 and M4. The P-domains P1 and P2 are crucial for the formation of the channel pore and provide the selectivity filters for potassium (Djillani et al., 2019; Fig. 2). This architecture of the two P-domains is unique among the potassium channels, after which they were named. Functional K2P channels only exist as dimers. Dimerization occurs via a cysteine residue (C69) of the TM1-P1 linker through which two monomers are covalently bound via a disulfide bridge (Lesage et al., 1996c). This formation can take place between two identical (homodimers) or two different subunits (heterodimers) (Lesage et al., 1996b; Czirjak and Enyedi, 2001). Each subunit contributes with two P-domains to form a functional selectivity filter, which requires four P-domains (Doyle et al., 1998). P1 contains the amino acid triplet glycine-tyrosine (or phenylalanine)-glycine (Gly-Tyr(Phe)-Gly) and P2 the amino acid triplet glycine-phenylalanine (or leucine)-glycine (Gly-Leu(Phe)-Gly) (Fig. 2). This signature sequence determines potassium selectivity (Honoré, 2007; Djillani et al., 2019).

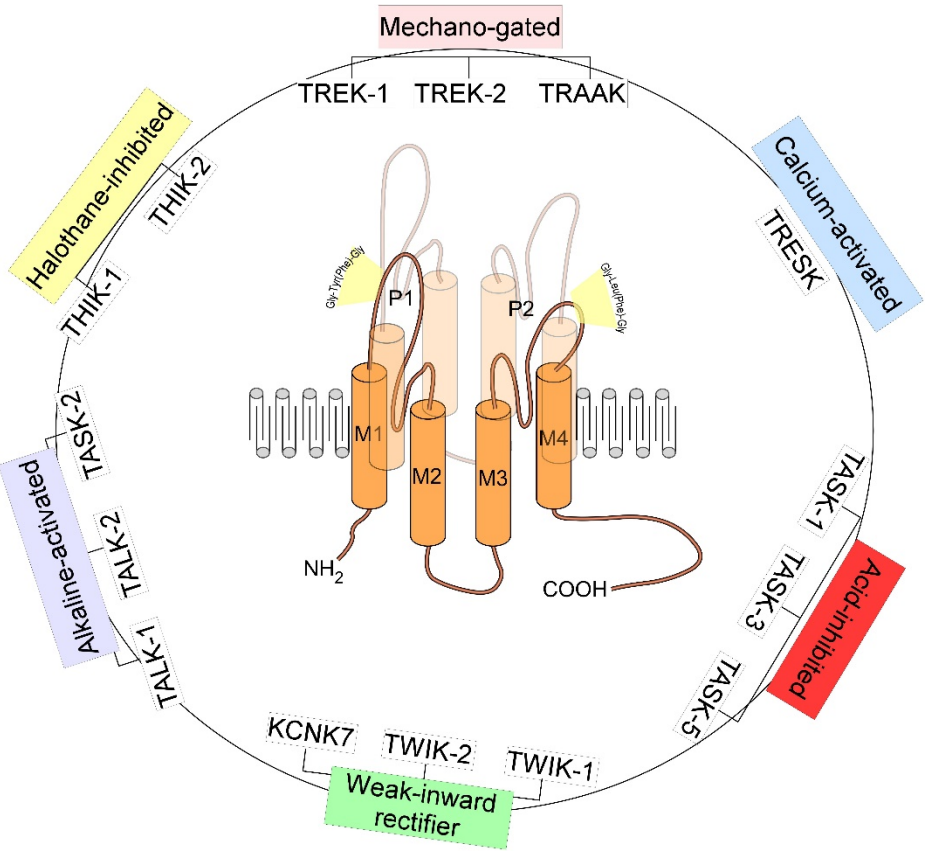

Figure 2: K2P channel family classification and structure.
The six structurally and functionally different subfamilies are shown together with their members and the regulatory properties. K2P channels typically consist of two pore-forming domains (P1 and P2) and four (M1-M4) TMs (2P/4TM). P1 and P2 often exhibit different sequences, as P1 usually contains the glycine-tyrosine (or phenylalanine)-glycine (Gly-Tyr(Phe)-Gly) and P2 the glycine-phenylalanine (or leucine)-glycine (Gly-Leu(Phe)-Gly) triplet. (adapted from Djillani et al., 2019).

K2P channels are activated by a variety of chemical and physical stimuli such as temperature, mechanical tension, membrane lipids (e.g. Phosphatidylinositol 4,5-bisphosphate (PIP2)), polyunsaturated fatty acids (e.g. Arachidonic acid), phosphorylation, volatile anesthetics (e.g. halothane) and changes in extracellular pH (Feliciangeli et al., 2015). They are insensitive to the usually applied potassium channel blockers, such as tetraethylammonium (TEA), Ba^{2+}, Cs^{+} and 4-aminopyridine (4-AP), which diminishes the ability to isolate native K2P channel currents via specific pharmacology (Feliciangeli et al., 2015). For a long time, K2P channels were described as background- or “leak” channels and their only function was thought to be to set the RMP. As a matter of fact, they generate current that is almost independent of membrane voltage and show Goldman-Hodgkin-Katz open rectification (Honoré, 2007), thereby revealing open state at rest. This way, K2P channels enable potassium ions to pass through the cell membrane even at the RMP. However, not all K2P channels meet these criteria. Modifications from this electrical

behavior have been observed in the TWIK subfamily as TWIK2 current was found to show a slow inactivating component (Patel et al., 2000). In addition, K2P function is not limited to maintain the negative RMP as MacKenzie and colleagues showed that K2P channels are capable of AP repolarization and even support AP generation in the absence of Kv channels (MacKenzie et al., 2015).

K2P channel expression has been detected in many different regions of the central- and peripheral nervous system as well as in many non-neuronal tissues such as the heart, pancreas, lung, liver, ovary, prostate and kidney (Lesage and Lazdunski, 2000). In addition to the functions described above, K2P channels have been implicated in a variety of physiological and pathophysiological processes such as anesthesia (Patel et al., 1999), bicarbonate transport in the kidney to regulate the acid-base balance (Warth et al., 2004), neuroprotection (Heurteaux et al., 2004), depression (Heurteaux et al., 2006), pain perception (Alloui et al., 2006), cancer (Williams et al., 2013) and microglia motility (Madry et al., 2018).

1.4. The Task (TWIK-related acid-sensitive potassium channel) family

The TWIK-related acid-sensitive potassium channel (Task) subfamily of K2Ps takes its name from its sensitivity to changes in extracellular pH and the structural similarity to TWIK channels. Due to low amino acid homology between Task and TWIK subfamilies (25-28%), it was decided that Task represents an independent subfamily. Task1 (also known as KCNK3) was the first member discovered in human kidney (Duprat et al., 1997). Its expression is quite ubiquitous and has also been detected in the pancreas, lung, uterus, placenta, small intestine and the brain (Duprat et al., 1997). This channel exhibits all the criteria to be classified as a so-called leak channel, as its activity is independent from membrane voltage, does not change over time and the current-voltage (I-V) relationship exhibits outward rectification, following Goldman-Hodgkin-Katz open rectification.

Task channel activity can be modulated by extracellular acidification (Duprat et al., 1997). It is highly presumed that a histidine residue (His98) within P1 is responsible for the sensitivity to extracellular pH changes. Interestingly, a histidine-to-tyrosine mutation in rodents abolished channel functionality (Lotshaw, 2007). However, this sensitivity to extracellular pH changes is not limited to Task channels, which eliminates the possibility to use pH sensitivity to isolate Task channels from other K2P channel subfamilies (Lotshaw, 2007). In addition, it can be activated via

volatile anesthetics (e.g. halothane and isoflurane) that hyperpolarize the membrane and thereby prevent the neuron from generating APs (Enyedi and Czirják, 2015).

Members of the Task subfamily are Task1, Task3 (also known as KCNK9) and Task5 (KCNK15) consisting of 394 (Task1; Duprat et al., 1997), 374 (Task3; Rajan et al., 2000) and 330 (Task5; Kim and Gnatenco, 2001) amino acids, respectively. The conserved cysteine that is reported in the literature (Duprat et al., 1997) to form the covalent binding of two monomers in most K2P channels is not present in the Task subfamily. Rat Task1 and Task3 share 54% amino acid sequence identity (Kim et al., 2000). Both also share 51% identity with Task5 (Kim and Gnatenco, 2001). Rat Task members and their human homologues exhibit a high degree of amino acid sequence identity (Task1 and Task3 ~94%, Task5 90%; Kim et al., 2000; Karschin et al., 2001). Among the Task subfamily, Task5 is assigned to the Task subfamily simply due to structural similarities. To date, the biophysiological and pharmacological characteristics of Task5 are unknown.

1.5. Task5 channel

1.5.1. Task5 structure and tissue expression

Task5 was discovered in 2001 by four different research groups, while cloning Task3 (Kim and Gnatenco, 2001; Ashmole et al., 2001; Karschin et al., 2001; Vega-Saenz de Miera et al., 2001). Based on its 2P/4TM structure and the intracellularly located amino- and carboxyl termini, it was classified as a K2P channel. Its open reading frame was found to be 990 nucleotides long, encoding a protein of 330 amino acids (Kim and Gnatenco, 2001) and resulting in a protein of 32 kDa. Human Task5 DNA consists of exon I (283 bp) and exon II (708 bp), separated by an intervening sequence (4.98 kb). Similar to Task1 and Task3, Task5 possesses a histidine residue in the first extracellular domain, responsible for extracellular pH sensitivity. Hence, Task5 might exhibit the same characteristic Task-subfamily sensitivity to extracellular pH alterations (Kim and Gnatenco, 2001).

First investigations of Task5 expression in human tissue by RT-PCR and Northern blot, revealed high Task5 expression in adrenal glands and the pancreas, moderate expression in liver, kidney, lung, ovary, testis and heart and rather low or even no expression in brain and skeletal muscle (Kim and Gnatenco, 2001; Ashmole et al., 2001). Later the same year, Karschin and colleagues detected high amounts of Task5 in the rat brain via RT-PCR. Further analysis of Task5

expression in the central nervous system via *in situ* hybridization revealed Task5 expression almost exclusively in the central auditory pathway, the olfactory external plexiform layer and in cerebellar Purkinje cells in the posterior lobe (Karschin et al., 2001). Lately, Ehmann et al. made an interesting observation, which may serve as an indication of Task5's functional relevance during postnatal development of the central auditory system. They not only confirmed the presence of significant amounts of Task5 within the SOC, but also revealed developmental upregulation of Task5 around hearing onset (Ehmann et al., 2013). Of note, Task5 exhibits the most restricted expression pattern among the Task members, whereas Task1 and Task3 display a far more widespread tissue distribution. To date, it was not possible to assess Task5 expression at protein level due to the lack of an adequate antibody.

1.5.2. Biophysical properties and functional expression

Unlike Task1 and Task3, Task5 failed to show functional expression in various heterologous systems including HEK293 and COS-7 cells (Fig. 3), HeLa cells (Kim and Gnatenco, 2001; Ashmole et al., 2001) and *Xenopus laevis* oocytes (Karschin et al., 2001).

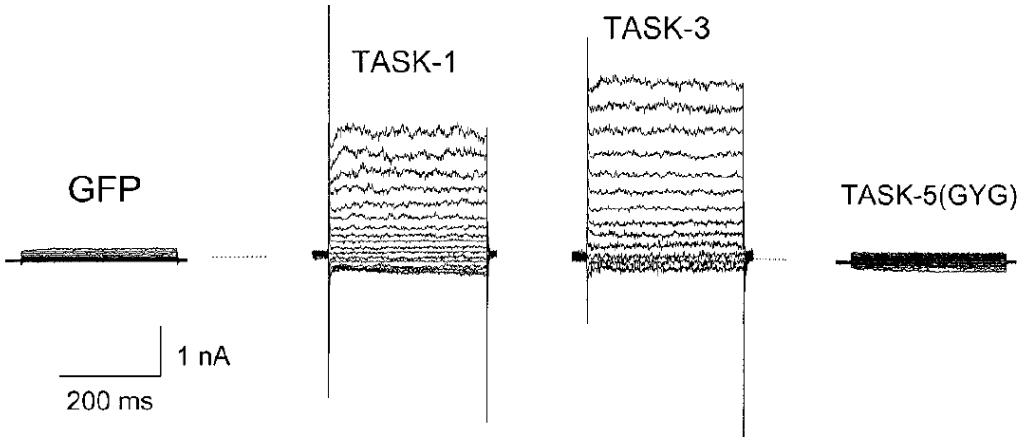

Figure 3: Comparison of whole-cell recordings of transfected COS-7 cells with Task subfamily members.

COS-7 cells transfected with Task5 did not exhibit measurable currents, which was comparable to the transfection of COS-7 cells with GFP only. Same recordings performed under same conditions produced large potassium currents in Task1- and Task3 transfected cells. (adapted from Kim and Gnatenco, 2001).

Sequence analysis of human Task5 revealed the presence of four polymorphisms in the coding region of Task5 (at codons 95,260,261 and 323). Particularly interesting is the single nucleotide polymorphism in the P1 domain (at codon 95), leading to an exchange of glycine to glutamate (from GGG to GAG), which is hypothesized to be responsible for the failure of Task5 to induce

measurable potassium currents (Kim and Gnatenco, 2001; Karschin et al., 2001). Further attempts to examine functional expression of Task5 failed as well. Expression of enhanced green fluorescent protein (EGFP)-tagged Task5 in HEK293 cells and *Xenopus* oocytes failed to show surface membrane localization (Ashmole et al., 2001; Karschin et al., 2001). This incorrect targeting of Task5 could explain the absence of measurable currents in these expression systems.

These failed attempts to functionally express Task5 and the lack of channel activity led to two theories of Task5 function: first, Task5 might be reliant on a yet unidentified partner for proper targeting to the plasma membrane. Otherwise it would be retained intracellularly. As a matter of fact, the Task5 sequence possesses a di-arginine motif at the amino terminus, which could lead to the retention of Task5 at the endoplasmic reticulum (ER) (Ashmole et al., 2001). However, the expression of a Task5 mutant, in which the retention motif was replaced with sequences from Task1 and Task3, similarly failed to evoke currents in HEK293 cells and *Xenopus* oocytes (Ashmole et al., 2001). Nonetheless, Karschin and colleagues achieved success by the construction of Task5/Task3 chimeric constructs, in which Task5's TM1-TM3 region was replaced with that of Task3. By doing so, they successfully induced measurable current responses (Karschin et al., 2001). This achievement gave rise to the second hypothesis, which suggests that Task5 fails to gate current due to its specific sequence of the region between TM1-TM3.

The predominant expression of Task5 mRNA in auditory brainstem nuclei highly indicates a possible involvement of Task5 in acoustic information processing, which is in line with three studies, investigating deafness associated changes in Task5 expression (Holt et al., 2006; Cui et al., 2007; Dong et al., 2009). Bilateral deafening in the rat resulted in tremendous decrease of Task5 mRNA amounts in the CN (Holt et al., 2006) and the inferior colliculus (Cui et al., 2007), which was found to be the strongest deafness-associated decrease of all investigated K2P channels. Similarly, Dong and colleagues discovered a significant decrease of Task5 mRNA expression in the ipsilateral CN and in both inferior colliculi following unilateral deafening in guinea-pigs (Dong et al., 2009).

1.6. Aim of the study

Since the discovery of Task5 in 2001, not much has been found out about its function and previous studies on Task5 raised more questions than they offered answers. In consideration of Task5's high and restrictive expression in auditory brainstem nuclei and its deafness-associated

downregulation within the CN and the inferior colliculus, two nuclei of the ascending auditory pathway, it appears rather unlikely that Task5 is indeed non-functional. For this reason, the main goal of this study is to elucidate the role of Task5 within the auditory brainstem circuit with particular focus on the VCN and the MNTB. These nuclei were chosen because of their high Task5 abundance (Karschin et al., 2001; Ehmann et al., 2013; GSE49599, Körber et al., 2014), and due to the extraordinary specialized features within this pathway, enabling ultra-fast and precise processing of acoustic information. For this purpose, the physiological role of Task5 is examined in rats and mice, using different methods of genetic perturbation. This approach offers the advantage over previous studies that Task5 as well as possible interaction partners necessary to assert its physiological role are present. In a first set of experiments, the physiological relevance of Task5 within the VCN and the MNTB of rats is examined by short hairpin RNA (shRNA)-mediated downregulation of Task5 expression in either nuclei. This genetic perturbation is relatively acute and leaves Task5 expression intact in the rest of the brain. A second set of experiments takes advantage of the generation of constitutive Task5 knockout mice, which do not express Task5 in any brain region at any time point.

The prime objectives of this study, regarding the function of Task5, are to determine
(I) the subcellular localization of Task5 to identify the environment, in which Task5 performs a specific function.
(II) whether Task5 complies with the characteristic biophysical properties of K2P channels, such as the regulation of cell excitability, setting the RMP, contributing to AP waveform and affecting firing pattern.
(III) whether and how potential alterations in AP waveform and firing pattern in response to Task5 knockdown and knockout influence high-frequency synaptic neurotransmitter release.
(IV) whether Task5 plays a role in the processing of auditory signals at the network level, by investigating ABRs and distortion product otoacoustic emissions (DPOAEs) in Task5 knockout mice.

2. Materials and Methods

2.1. Animals and housing

Timed pregnant Sprague-Dawley CD rats acquired from Charles River Laboratories, were housed individually in Makrolon type IV cages (58,5 × 37,5 × 20 cm) and had access to food and water *ad libitum.* They were kept under a non-inverted 12-hour light-dark cycle (lights off at 8 am and on at 8 pm). The litter was reduced to seven pups at P4.

Constitutive Task5 knockout mice were generated from the VGB6-derived (C57BL/6NTac strain) embryonic stem (ES) cell clone 10341A-F11 (Regeneron Pharmaceutica; Eastview, NY, USA). ES cells were injected into C57BL/6 eight-cell stage embryos by the Knockout Mouse Project (KOMP; University of California, Davis, CA, USA) Repository. Constitutive knockout of the Task5 gene, located on chromosome 2, was achieved using the VelociGene technology as described previously (Valenzuela et al., 2003). Cryopreserved sperm, purchased from the KOMP Repository to generate the Task5-KO mouse line, was used for *in vitro* fertilization of C57BL/6 oocytes, performed by the Interfacultary Biomedical Faculty (IBF) of the Heidelberg University to generate healthy F0 generation mice. For the generation of homozygous (-/-) mice, heterozygous mice were further crossed between each other. Genotyping was performed by Polymerase chain reaction (PCR) in one reaction for the WT and KO allele with the following primers: WT: forward (Reg-wtF) 5'- ATTCTGTGCATCCTGTCCTACCTGC-3' and reverse (Reg-wtR) 5'- GATGACCGTGATGGCGAAGTAGAAG-3', Task5-KO: forward (Reg-Neo-F) 5'- GCAGCCTCTGTTCCACATACACTTCA-3' and reverse (Reg-R) 5'- CATAAGGATGCTTGACCTGGGTATCG-3'. The resulting PCR product is 240 bp for WT mice and 386 bp for Task5-KO mice. The PCR mixture contained 1 µl genomic DNA sample, 10 µl 2xMyTaq Red Mix (#BIO-25043, Bioline), 0.3 µl (10 µM) forward and reverse primers and 7.8 µl dH_2O (final volume of 20 µl). The PCR program used was: 1x 95 °C for 3 minutes (hot start) and 35 cycles of 95 °C for 20 s, 67 °C for 20 s, 72 °C for 30 s, with a final extension at 72 °C for 5 minutes.

Task5-KO mice were group-housed in Makrolon type II cages (22 × 16 × 14 cm) with *ad libitum* access to food and water. They were kept on a 12h-12h day-night cycle. The housing and breeding of the mouse colony was carried out at the IBF of the Heidelberg University. Testing animals were picked up on the day of an experiment and transported to the laboratory. All

animals were kept and tested in accordance with the German welfare guidelines and were approved by the Regierungspräsidium Karlsruhe (Protocols: G160/15, T34/18).

2.2. Constructs and adeno-associated viruses (AAV) design

A 21 bp shRNA sequence directed against endogenous Task5 mRNA (GCCCAGAAGCAGTGCATGATT) was designed by Michaela Kaiser (Institute for Anatomy and Cell Biology, Heidelberg University) using the online tool BLOCK-iT™ RNAi Designer (ThermoFisher Scientific, https://rnaidesigner.thermofisher.com/rnaiexpress/). ShRNA oligonucleotides containing the target sequence were ligated downstream of the U6 promoter in the pStrataBlunt vector (subcloning vector). For AAV production the U6 promoter-shRNA cassette was further subcloned into the pAM vector (pAM vector: Klugmann et al., 2005) backbone expressing the fluorescent reporter mOrange. The fluorescent protein mOrange was driven under the cytomegalovirus early enhancer/chicken β actin (CAG) promoter *in cis*. The expression cassette contained the Woodchuck Hepatitis Virus Posttranscriptional Regulatory Element (WPRE) and the bovine growth hormone poly-A (pA) sequence and was flanked by inverted terminal repeats (ITR) (Fig. 4A). As a control for shRNA specificity, a rescue construct was generated by introducing silent point mutations in the shRNA target region of the Task5-mRNA. In this way, the shRNA will knock down the endogenous Task5, while the exogenously expressed protein will rescue the knockdown phenotype. To outcompete the knockdown, the rescue Task5 is overexpressed. The exogenous Task5 was driven by a second CAG promoter (Fig. 4B). To examine the subcellular localization of Task5, the Task5 protein was GFP-tagged, either c-terminally (Fig. 4D) or near the second pore domain (Fig. 4C). Both constructs were subcloned into the pAM vector backbone as described above.

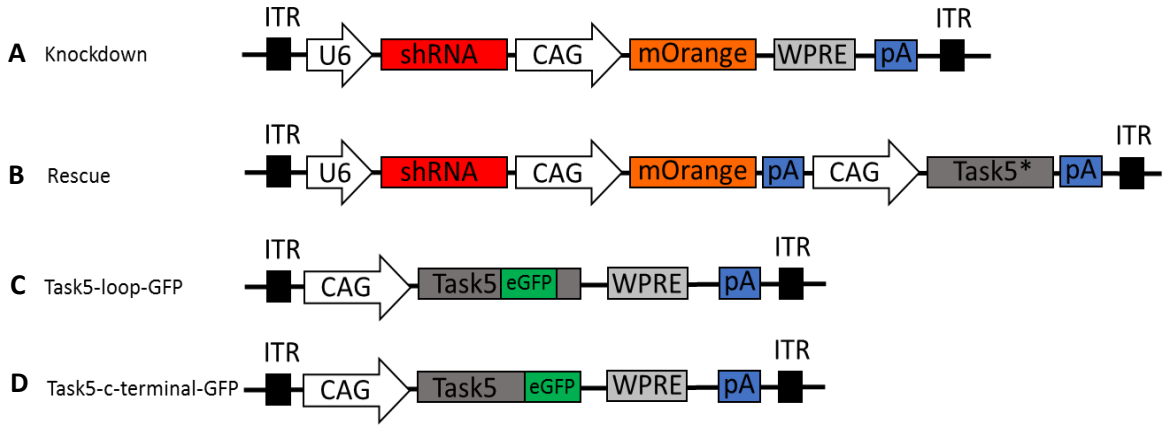

Figure 4: Construction map of AAVs.
AAV vector maps depicting the knockdown (**A**) and rescue (**B**) constructs as well as the P2-domain- (**C**) and the c-terminally-GFP-tagged (**D**) Task5 viral constructs. The asterisk* indicates overexpression of Task5.

2.3. Adeno-associated virus production

Cell culture for AAV production purposes was performed by Claudia Kocksch (Institute for Anatomy and Cell Biology, Heidelberg University). AAVs were produced as chimeras of serotype 1 and 2 with helper plasmids pDP1rs and pDP2rs (PlasmidFactory, Bielefeld, Germany) as described by Grimm et al. (Grimm et al., 2003). The AAV production was achieved in HEK293 cells (293AAV, Agilent Technologies, Santa Clara, California, USA). 4 x 10^6 HEK cells were seeded in 10 cm cell culture dishes in 10 ml Dulbecco's Modified Eagle's Medium (DMEM; Anprotec, Bruckberg, Germany, #AC-LM-0014), per 500 ml supplemented with 10% FCS (Gibco #10500-064), 0.2 mM non-essential amino acids (Gibco, #11140-035), 2 mM Na-pyruvate and 1% penicillin/streptomycin (Anprotec, #AC-AB-0024). After 24 hours, the cells were transfected with equimolar amounts of pAM plasmids, pDP1rs, and pDP2rs using polyethylenimine (PEI, Sigma, #408727) based transfection method. 2.5 ml of the transfection mixture composed of 1 mg/ml PEI in OptiMEM (Gibco #31985-062) and 37.5 µg DNA was added drop-wise to each culture dish. To stop the transfection, the medium was exchanged after 2 – 4 h. Three days post-transfection, virus particles were harvested and purified. For this purpose, cells were harvested with a cell scraper, pelleted (200g, 10 min, 4 °C), resuspended in TNT buffer (in mM: 150 NaCl, 50 Tris-HCl, pH 8.5) and were lysed via one freeze-thaw cycle. To remove genomic DNA, it was digested by the application of 50 U of benzonase nuclease (Sigma, #E1014) at 37 °C for 1 h. Cell debris was pelleted via centrifugation at 2500 rpm for 15 min at 4 °C. The supernatant was filtered by pushing the solution through a 0.45-µm filter (Millex, 13 mm, #SLHV013SL) into a 15 ml falcon tube to collect the crude lysate. Crude lysate was further purified by centrifugation (2000 rpm, 10 min) together with 40 ml DMEM. Supernatant was filtered using 0.45 µm pore-size filters (Millex, #SLHP033RS) and directly applied to a 1 ml HiTrap Heparin column, used with the ÄKTAprime plus fast protein liquid chromatography (FPLC) system (GE Healthcare, UK). The columns were washed with 20 ml equilibration buffer and the viral particles were eluted with 15 ml elution buffer (10 mM Na_3PO_4, 1-2 M NaCl in PBS, pH 7) to be collected in an Amicon-ULTRA filter (100000 MWCO, Millipore). The Amicon filter was washed twice with 5 ml sterile Phosphate Buffered Saline (PBS, pH 7.4). The

virus solution was filtered through a 0.22 µm (Millex, #SLGV004SL) filter and stored at 4 °C in 100 - 120 µl aliquots until further usage.

2.4. Stereotaxic injections

After removing the rat pups from their mother, the animals were kept on a precision heating plate (H. Saur, Laborbedarf, Reutlingen, Germany) set to 37 °C until injection. Before each injection procedure, the stereotaxic setup was calibrated according to the manufacturer's protocols. P3 rats of either sex received anesthesia using 5% isoflurane (Baxter, Deerfield, IL, USA) inhalation in O_2 (Vaporizer: Isotec4, Surgivet, Dublin, OH, USA) and placed into a stereotaxic frame (basic model: 1900, David Kopf Instruments, Tujunga, CA, USA). Approximately after five minutes the isoflurane concentration was lowered and maintained between 1 and 0.7% throughout surgery. Body temperature was controlled using a feedback-regulated temperature control system (Stoelting) during the entire surgical procedure and breathing rate was monitored by visual inspection. Proper anesthesia was checked by pinching the interdigital skin. The lack of withdrawal reflexes of the hindlimbs shows anesthetic depth. Lidocain (product name: Xylocain 1%, AstraZeneca, Wedel, Germany) was administered subcutaneously to numb the skin prior to incision. A straight cut was performed on the skull and the skin was retracted to expose the skull. Skull and tissue were kept moist with Ringer's solution (in mM: 135 NaCl, 5.4 KCl, 5 HEPES, 1.8 $CaCl_2$, 1 $MgCl_2$) during the entire surgery. Two marks were set as reference points at lambda and bregma and the distance between lambda and bregma was determined. Craniectomy was performed directly above injection target sites, defined by injection coordinates, using a dental drill (Osada). The head was levelled in the sagittal and coronal plane by bringing lambda and bregma on the same dorso-ventral and medio-lateral planes. Injection capillaries were pulled from micropipettes (#708707, Brand, Wertheim, Germany; volume range of 1-5 µl) on a horizontal puller (P97, Sutter Instruments, Novato, CA, USA) and either placed in a custom-built manipulator (Wimmer et al., 2004) for VCN or a straight pipette holder (Kopf, Model 1975) for MNTB injections. 2.5 µl of the virus solution was loaded into the capillary by a 50 ml syringe using a plastic tube that was attached to the flat end of the injection capillary. For VCN injections the virus was evenly distributed between injection sites (Table 1). In the MNTB the entire volume was injected into the single injection site (X, Y, Z [mm]: 0.65, 1.2 x distance Bregma-Lambda, -5.7). After injection, the incision was sutured (B|Braun, Dafilon DSMP11, #0936022) and after a quick recovery from anesthesia the animals were returned to the mother.

Table 1: Injection coordinates for P3 rats in the VCN. Distances are given in millimeters relative to bregma and midline.

X	Y	Z	Depth Ax.
0.7	-7.2	0.3	6.5
0.7	-6.8	0.3	6.5
0.7	-6.4	0.3	6.5
0.9	-6.6	0.35	6.5
0.9	-7.0	0.35	6.5

2.5. Preparation of fixed brain slices

After *in vivo* incubation of ~10 days of the injected virus, P12-P14 rats were deeply anesthetized with intraperitoneal injection of Narcoren (50 mg/kg bodyweight; Merial GmbH, Germany). Proper anesthesia was checked by pinching the interdigital skin before perfusion was performed. A lateral incision was made through the abdomen and the diaphragm was separated from the chest wall to expose the heart. A 22G injection needle (BD Microlance ^{TM}) was passed through the left ventricle and a small cut was made through the right atrium. The animals were perfused transcardially with ~20 ml 1x PBS followed by 20 ml 4% paraformaldehyde (PFA, 4% in PBS). Subsequently, the brain was removed by carefully opening the skull and post-fixed in 4% PFA for 4 hours at 4 °C. Finally, perfused brains were stored in 1x PBS at 4 °C until further usage. Free floating 100 µm thick coronal sections containing the VCN and the MNTB were cut on a vibratome slicer HR2 (Sigmann Elektronik, Hüffenhardt, Germany) and kept in PBS at 4 °C.

2.6. Immunofluorescence labeling

2.6.1. Cortical neuronal culture

Primary cultures of rat cortical neurons were prepared and kindly provided by Marion Schmitt (Institute for Anatomy and Cell Biology, Heidelberg University) as described by Dresbach and colleagues (Dresbach et al., 2003) with some modifications. In brief, cortical neurons were dissected from embryonic day 19-20 (E19-29) Wistar rat embryos, dissociated, resuspended in neurobasal media (ThermoFisher) supplemented with 1% Penicillin/Streptomycin solution, 2% B27 and 0.5 mM glutamine and seeded at approximately 60000 cells/ml (with each 24-well plate

containing 0.5 ml) onto coverslips coated with poly-L-lysine in 24-well plates. Plates were kept at 37 °C in a humidified CO_2 incubator with 5% CO_2.

2.6.2. Immunocytochemistry

Cortical cultured neurons were transduced with rAAVs after 14 days *in vitro* (DIV) by adding 1 µl virus solution to each well. On DIV4 (Task5-c-terminal-GFP) and DIV7 (Task5-P2domain-GFP) cells were briefly washed in 1x PBS, fixed in 4% PFA in PBS (20 minutes at room temperature (RT)), blocked and permeabilized in blocking solution (5% sucrose, 5% bovine serum albumin, 5% FCS and 0.3% Triton X-100 in 1x PBS; 2 hours at RT) on a rocking shaker (Neolab). Subsequently, cells were incubated overnight with primary antibodies at 4 °C on an orbital shaker (Neolab). The day after, cells were washed in 1x PBS (3x10 minutes at RT) and incubated with secondary antibodies in blocking solution for 45 minutes under light protection on a rocking shaker at RT. Finally, cells were washed in 1x PBS (3x10 minutes at RT), mounted in Mowiol and kept at 4 °C until imaging.

2.6.3. Immunohistochemistry

Fixed brainstem slices were permeabilized in blocking buffer containing 5% normal goat serum (NGS; Jackson Immunoresearch Laboratories) and 1% Triton X-100 in PBS. Sections were incubated overnight at 4 °C on an orbital shaker in primary antibodies diluted in antibody buffer (1% NGS and 0.2% Triton X-100 in 1x PBS). Prior to secondary antibody staining on the next day, sections were washed three times for 10 minutes in washing buffer 1 containing 2% NGS in 1x PBS. Sections were incubated in the appropriate secondary antibodies diluted in blocking buffer for ~2-3 hours at RT under light protection. After washing the slices three times for 15 minutes in washing buffer 2 containing 1% NGS in 1x PBS and another three washing steps of 10 minutes each in 1x PBS at RT, the slices were mounted on Menzel X50 Microscope Slides (ThermoFisher) and embedded in Slow Fade Gold (ThermoFisher, #S36936). Coverslips were sealed with clear nail polish and the slides were stored at 4 °C.

Table 2: Primary Antibodies

Target Antigen	Host Species	Clone	Dilution	Source	Cat. No.
PDI	mouse	monoclonal	1:500	Santa Cruz	ADI-SPA891
GFP	chicken	polyclonal	1:500	Abcam	Ab 13970
Tom20	rabbit	polyclonal	1:500	Santa Cruz	Sc-11415
TGN38	rabbit	polyclonal	1:500	NBPT	03495

Table 3: Secondary Antibodies

Target Antigen	Host Species	Conjugated fluorophore	Dilution	Source	Cat. No.
mouse	goat	Alexa Fluor 647	1:1000	Invitrogen	A-21235
chicken	goat	Alexa Fluor 647	1:1000	Invitrogen	A-21449
rabbit	goat	Alexa Fluor 647	1:1000	Invitrogen	A-21245
mouse	goat	Alexa Fluor 532	1:1000	Invitrogen	A-11002
rabbit	goat	Alexa Fluor 532	1:1000	Invitrogen	A-11009

2.6.4. Confocal imaging

Confocal images were acquired on a Leica TCS SP5 microscope equipped with a 10x/0.4NA HC PL APO multi-immersion (Leica Microsystems, # 11506293) and a 63x/1.3NA HCX PL APO glycerol-immersion (Leica Microsystems, #11506194) objective. Single images were acquired at scan speed of 100 Hz and image stacks at 400 Hz unidirectional with a resolution of 512 x 512 pixels; pin hole was set to 1 airy unit. Sequential scanning was used to avoid bleed-through. All images were processed with Image J.

2.7. RNAscope Technology and tissue processing

2.7.1. Preparation of fresh frozen tissues

Prior to tissue preparation, the work area and all tools were wiped with RNaseZAP (Sigma, #R2020) to remove RNase contamination. Task5 deficient mice at prehearing stages (~P7), at the

onset of hearing (~P14) and at adult hearing stages (~6 weeks) were decapitated, the brain was quickly removed, snap frozen on aluminum foil on dry ice and stored at -80 °C until sectioned. Immediately before sectioning, the brains were snap frozen in cryomolds made of aluminum foil containing Tissue-Tek O.C.T. compound (Sakura, Japan, #4583). 20 µm auditory brainstem sections were cut using a Microm HM 560 cryostat (ThermoFisher). Sections were transferred to Super Frost Plus slides (R. Langenbrinck GmbH) by gently pressing the slide onto the tissue. Mounted sections were dried within the cryostat for ~60 minutes at -20 °C and stored at -80 °C until processing.

2.7.2. RNAscope *in situ* hybridization method

The RNAscope Multiplex Fluorescent Reagent Kit (Advanced Cell Diagnostics, Newark, USA; Probes: Mm-Rbfox3-C1, Mm-Kcnk15-C2, #320850) is a novel fluorescence *in situ* hybridization (FISH) technique to detect target RNA in freshly frozen tissue (Wang et al., 2012). The RNAscope assay was performed to confirm successful Task5 knockout, on the one hand, and on the other hand to detect Task5 mRNA expression (Mm-Kcnk15-C2 probe, #528421-C2) in auditory brainstem slices. The Mm-Rbfox3-C1 (#313311) probe was used to test for neuron specific Task5 expression. All FISH procedures were performed following the manufacturer's instructions. Briefly, slides were removed from -80 °C storage and immediately immersed in cooled 4% PFA (Alfa Aesar, # J61899) on ice for 15 minutes. The slides were quickly rinsed with sterile 1x PBS followed by four dehydration steps of 5 minutes in 50%, 70% and two times in 100% EtOH at RT. Slides were air dried on whatman paper (GE Healthcare, #3030-917) for 5 minutes. A barrier was drawn around each section with a hydrophobic barrier pen (Advanced Cell Diagnostics, #310018) and Protease IV treatment was performed for 15 minutes at RT. After two quick washing steps in sterile 1x PBS the sections were covered in the appropriate probe mix and the probes were hybridized in the HybEZ Hybridization Oven (Advanced Cell Diagnostics) for 2 hours at 40 °C. The hybridization step was followed by four amplification steps with two washing steps prior to each amplification step. The sections were incubated with Amp 1-FL for 30 minutes, Amp 2-FL for 15 minutes, Amp 3-FL for 30 minutes and Amp 4B-FL for 15 minutes at 40 °C. After the last two washing steps, the sections were briefly incubated in DAPI, coverslipped with Slow Fade Gold and stored at 4 °C until imaging.

2.7.3. Confocal imaging

Confocal images were acquired on a Leica SP8 microscope with a 20x/0.75NA HC PL APO multi-immersion (Leica Microsystems, #11506343), a 40x/1.3NA HC PL APO (Leica Microsystems, #11506358) oil-immersion and a 63x/1.4NA HC PL APO oil-immersion (Leica Microsystems, #11506350) objective. Scan speed was set to 100 Hz unidirectional and a resolution of 1024 x 1024 pixels. Sequential scanning was used to avoid bleed-through. The Amp AltB solution, used in the last amplification step of the RNAscope, resulted in probe labeling of C1 with Atto 550 (Rbfox3) and C2 with Alexa 488 (Task5). All images were processed with Image J.

2.8. Electrophysiology

2.8.1. Preparation of acute brain slices

Mice and rats at the age of P12-P14 were rapidly decapitated. Brains were immediately transferred to ice-cold slicing solution oxygenated by carbogen (95% O_2 and 5% CO_2) containing (in mM): 125 NaCl, 25 $NaHCO_3$, 2.5 KCl, 1.25 NaH_2PO_4, 3 myoinositol, 2 Na-pyruvate, 0.4 ascorbic acid, 0.1 $CaCl_2$, 3 $MgCl_2$, 25 glucose. For current clamp and outward K^+ current recordings, 300 µm transverse slices containing the MNTB and the VCN were made on a vibratome (VT1200S, Leica). For electrical stimulation of the auditory nerve root (ANR), 200-250 µm parasagittal slices containing the CN were cut. Slicing was carried out at 0.08 mm/s forward blade feed rate and 1 mm amplitude. During the whole slicing procedure, the slicing solution was constantly aerated with carbogen. Slices were stored at 37 °C in ACSF, constantly oxygenated by carbogen containing (in mM): 125 NaCl, 25 $NaHCO_3$, 2.5 KCl, 1.25 NaH_2PO_4, 2 $CaCl_2$, 1 $MgCl_2$ and 25 glucose. After 30 - 45 minutes, slices were kept at RT.

2.8.2. Current clamp and outward K^+ current recordings

All experiments were performed in carbogen aerated ACSF at RT containing (in mM): 125 NaCl, 25 $NaHCO_3$, 2.5 KCl, 1.25 NaH_2PO_4, 2 $CaCl_2$, 1 $MgCl_2$ and 25 glucose. To record outward K^+ currents, 1 µM Tetrodotoxin (TTX, hellobio, Bristol, UK; #HB1035) and 250 µM cadmium chloride ($CdCl_2$, #C3141) were added to the ACSF. Patch pipettes (3-8 MΩ) were pulled from thin-walled borosilicate glass capillaries (outer diameter 1.5 mm, inner diameter 0.84 mm; #1B150F-4, World Precision Instruments, Sarasota, Florida, USA) on a horizontal puller (P97, Sutter Instruments, Novato, CA, USA). The pipette intracellular solution contained (in mM): 130 K-gluconate, 4 KCl, 5 Na_2-phosphocreatine, 10 HEPES, 0.1 EGTA and 4 Mg-ATP, pH was

adjusted to 7.2 using KOH and the final osmolarity was ~283 mOsm. For some measurements, the solution was supplemented with Biocytin (1.5 mg/mL; Sigma-Aldrich, #B4261) for morphological identification of GBCs. MNTB principal cells and GBCs were identified under an Olympus BX51WI upright microscope equipped with Dodt gradient contrast optics (Luigs und Neumann, Ratingen, Germany) using a C-CCD camera (Spot RT, Diagnostic Instruments, Sterling Heights, MI). Cells expressing knockdown (KD) and Rescue constructs were identified by the fluorescent protein mOrange using a Cell^{tool} Illumination System MT10_D (Olympus). Whole-cell voltage- or current clamp recordings were acquired from MNTB principal cells and GBCs in the VCN using a HEKA EPC-10/2 amplifier controlled by PATCHMASTER software (HEKA, Lambrecht, Germany). Recordings were Bessel-filtered at 2.9 kHz and 10 kHz and sampled at 40-100 kHz. Recorded cells were clamped at -70 mV. Input resistance was assessed in current clamp mode as the slope of the linear regression of the voltage-current (V-I) curves in response to 20 pA steps from -100 pA to 20 pA. Data was collected at the steady-state voltage close to the end of the injected current pulse.

To assess the AP waveform, APs were evoked by injecting current for 5 ms starting at -100 pA with an increasing factor of 50 pA (in total 20 sweeps). Firing pattern was examined by long current injections for 200 ms starting at -200 pA in 20 pA increments (in total 60 sweeps). Voltage gated outward potassium currents were elicited in response to 100 ms voltage steps at potentials between -100 mV and 45 mV in 5 mV voltage steps from a holding potential of -70 mV.

2.8.3. Recordings from GBCs upon ANR stimulation

Excitatory postsynaptic currents (EPSC) were evoked by electrical stimulation of the ANR. A parallel Pt-Ir bipolar electrode (200 µm distance; FHC, Bowdoin ME; #PBSA0275) was placed on the ANR (6-8 V stimuli, 100 µs duration) and recordings were performed from GBCs in the AVCN at RT. Recording pipettes were pulled to have an open-tip resistance of 2 - 3 MΩ and backfilled with intracellular solution containing (in mM): 130 Cs-gluconate, 10 CsCl, 10 HEPES, 10 TEA-Cl, 5 Na_2 -phosphocreatine, 5 EGTA, 4 Mg-ATP and 0.3 GTP, adjusted to pH 7.2 using KOH and the final osmolarity was ~353 mOsm. The AVCN was identified at low magnification. Whole-cell access resistance was less than 15 MΩ and was corrected automatically by 30-80% at a time constant of 100 µs. Leak current was in most cases less than 100 pA and did not exceed 200 pA. EPSCs were evoked by applying trains of stimuli (20 stimuli at 10 Hz; 50 stimuli at 100,

200 and 300 Hz) using a custom-built bipolar-isolator (Max-Planck-Institute for Medical Research, Heidelberg, Germany). Low-frequency stimulation at 0.1 Hz was delivered by brief stimuli, at 10 s interval (10 times).

2.8.4. Data analysis

Data analysis was performed using either macros written for Igor Pro 6 Software (WaveMetrics, USA; provided by Darius Schwenger and Christoph Körber) or by using AxoGraph 1.7.6 (Axograph Scientific (John Clements)).

2.8.5. Biocytin histology

Immediately after recordings, acute brainstem slices with biocytin-filled MNTB principal cells and GBCs were fixed in 4% PFA in PBS overnight. Slices were washed in 1x PBS (3x5 minutes, RT) and incubated in blocking buffer (5% NGS and 1% Triton X-100 in PBS) for 3 hours. To label Biocytin, the slices were then treated with streptavidin coupled to Alexa647 (ThermoFisher, #S21374) in antibody buffer (1% NGS and 0.2% Triton X-100 in 1x PBS) at a dilution of 1:1000. Following three washing steps in 1x PBS (3x10 minutes, RT), slices were mounted in Slow Fade Gold on coverslips. Z-stacks were acquired to assess GBC and MNTB cell morphology with the laser-scanning confocal microscope Leica TCS SP5 as described in 6.4. Maximum intensity Z-projections of confocal image stacks were created using ImageJ.

2.9. Acoustic Measurements

All acoustic measurements were carried out with the help of Prof. Dr. Lukas Rüttiger at the Department of Otolaryngology, Head & Neck Surgery at the University of Tübingen. For acoustic measurements, ~6-8 weeks old WT and Task5 deficient mice of both sexes were tested. All procedures were approved by the local authorities (Regierungspräsidium Tübingen and Karlsruhe) and were performed in accordance with the guidelines of the European Union Directive 2010/63/EU for animal experiments. Prior to acoustic measurements, the mice were anesthetized by intraperitoneal administration of a mixture of 0.05 mg/kg bodyweight fentanyl dihydrogen citrate (Ratiopharm, Ulm, Germany), 5 mg/kg midazolam (Dormicum, Roche Pharma AG, Grenzach-Wyhlen, Germany) and 0.5 mg/kg medetomidin hydrochloride (Sedator, Eurovet Animal Health B.V., Aulendorf Germany). To maintain stable heartbeat, 0.2 mg/kg bodyweight atropine sulfate (B.Braun, Melsungen, Germany) was added to the mixture. Heart- and breathing rate were monitored to predict the depth of anesthesia. If required, additional doses

of anesthesia mix were administered by subcutaneous injection. In case measurements needed to be continued the next day, the anesthesia was terminated by subcutaneous injection of the antidote mix Naloxone (0.03 mg/kg bodyweight; Hameln Pharma Plus GmbH, Hameln, Germany), Flumazenil (0.1 mg/kg bodyweight; Fresenius Kabi Deutschland GmbH, Bad Homburg, Germany) and Atipamezole (1 mg/kg bodyweight; Elanco Animal Health, Bad Homburg; Germany).

2.9.1. Auditory brainstem recordings (ABR)

ABR and distortion product otoacoustic emission (DPOAE) measurements were recorded in a soundproof chamber (IAC, Niederkrüchten, Germany). ABR recordings provide information about hearing thresholds. To avoid hyperthermia of the experimental animals during the measurements, body temperature was maintained by heating pads and lamps. The generation of the stimuli and the recordings was computer-controlled (CAP/ABR, HNO-Universitätsklinik Tübingen; IBM). The sound pressure level of the generated stimuli was controlled automatically by an amplifier and an attenuator (Wulff Elektronik, Frankfurt, Deutschland). The generated stimuli were presented to the experimental animals via a loudspeaker placed approximately 3 cm lateral to the mouse pinna. To measure brainstem evoked potentials three subdermal silver wire electrodes were positioned: the reference electrode centrally in the scalp, the active electrode below the pinna of the recorded ear and the ground electrode at the back of the mouse. To determine the actual sound pressure, an additional high precision microphone (Brüel and Kjaer, type 4191, Naerum, Denmark) with a preamplifier (Brüel and Kjaer 2670, 1/4", 5 mV/Pa, Naerum, Denmark) was placed over the measured ear. Auditory evoked responses to click (100 ms), noise-burst (1 ms, random phase frozen noise) or pure tone stimuli (2–45.25 kHz, 3 ms) were recorded. Signals were amplified 100,000 times, bandpass filtered (0.2–5 kHz 6-pole Butterworth filter, Wulff Elektronik, Frankfurt, Germany) and averaged for 64-256 repetitions at each sound pressure level (SPL) presented. The auditory threshold was defined as the lowest SPL with clearly visible acoustically evoked potentials.

2.9.2. ABR waveform analysis

To perform waveform analysis, wave functions of each mouse were averaged and the response to 90 dB SPL click-, noise-burst and 16 kHz stimulation was analyzed. ABR waves were analyzed for peak amplitudes and latencies by customized computer programs. An ABR wave was defined as the voltage deflection from a starting negative peak to the following positive peak (peak-to-

peak amplitude). ABR wave amplitude and latency growth functions represent normalized thresholds. In addition, amplitude growth functions were determined by calculating the peak-to-peak amplitudes for increasing stimulus levels.

2.9.3. DPOAE Measurements

Cochlear outer hair cell function was investigated by the determination of thresholds and growth behavior of the cubic ($2f_1 - f_2$) distortion products of the otoacoustic emissions measured for f2 = 1.24×f1 and L2 = L1−10 dB. In brief, frequency pairs of tones (f2 = 4 kHz and 32 kHz) were sent directly into the ear canal by a speaker connected to a metal coupler under visual control. Sound pressure changes were recorded by a microphone, connected to the metal coupler as well. A DPOAE was considered to be valid if its level was 5 dB or more above that of the related noise floor range.

2.10. Statistics

The statistical software Prism 5.02 (GraphPad Software, La Jolla, CA, USA) was used for all statistical analyzes. Statistical test is stated either in the figure legend or in the results text. Data is displayed as mean ± SEM unless stated otherwise. For all statistical comparisons, p-values less than 0.05 were considered as significant.

3. Results

3.1. Task5 mRNA expression in auditory brainstem slices

In order to assess Task5 distribution in the auditory brainstem, and in particular in the MNTB and the VCN, the RNAscope Fluorescent Multiplex Assay (ACD Bio) was applied. Furthermore, the RNAscope FISH assay was used to visually confirm deletion of Task5 in KO mouse brains.

Task5 expression was detected in the VCN of WT mice at all phases of hearing (Fig. 5). Visual characterization of the expression pattern and relative abundance of Task5 suggests low Task5 expression at a pre-hearing stage (P7) with a sharp upregulation at hearing onset (P14). This strong expression is maintained at adult hearing (6 weeks), however creating the impression of a slightly weaker adult Task5 expression. The neuronal probe against Rbfox3 (a neuronal marker gene encoding NeuN) is detected in the cytoplasm, making it difficult to assign Rbfox3 expression to its respective nucleus. Sparse colocalization between Task5 and Rbfox3 was subjectively determined by visual inspection and is indicated by white arrows. Also, it is to be noted that with elevated Task5 expression, Rbfox3 expression appears to be less abundant. In addition, the essay confirmed successful knockout of Task5 in the mouse VCN. No Task5 positive signal could be detected in Task5-KO mice at any timepoint examined.

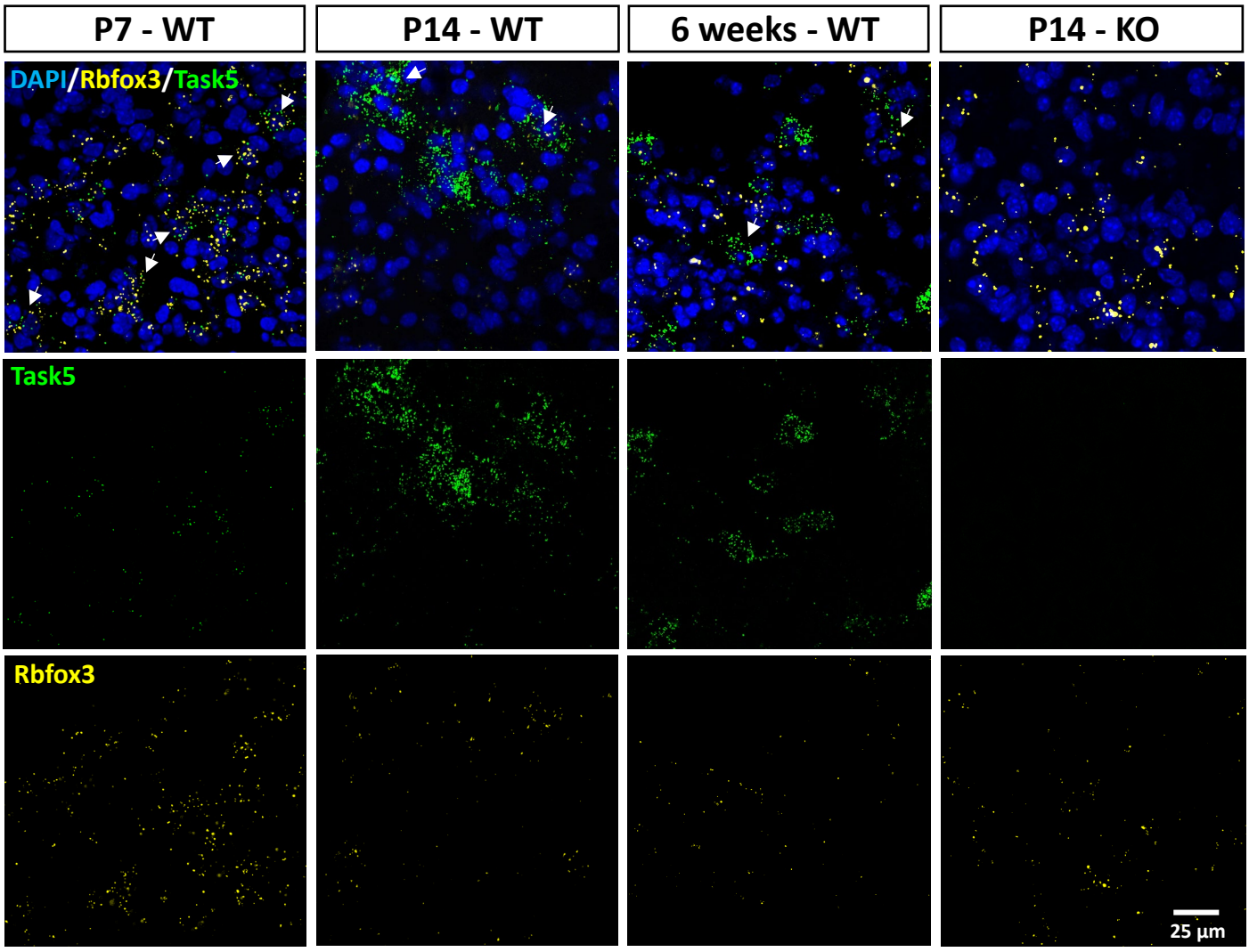

Figure 5: Task5 expression in the VCN during auditory maturation.
In situ hybridization patterns were obtained by the RNAscope assay with double "Z" oligo probes specific for Task5 and Rbfox3. Confocal images of mouse brainstem slices demonstrate differential Task5 expression. Task5 expression was found to be low at pre-hearing stages (P7) with a considerable upregulation at the onset of hearing (P14), which was maintained into adult hearing. Task5 knockout was successfully confirmed. Arrows indicate colocalization between Task5 and Rbfox3. Scale bar = 25 µm.

Contrary to Karschin and colleagues (Karschin et al., 2001), Task5 expression was detected in the MNTB of mice (Fig. 6). Similar to the VCN, expression was found at all timepoints examined, however to a much lesser extent. At P7, Task5 expression is hardly detectable, but increases at the onset of hearing and is maintained into adulthood, however still weaker than in the VCN. Colocalization between Task5 and Rbfox3 was found at all timepoints examined and is indicated

by white arrows. No Task5 expression was observed in the MNTB of KO mice, verifying successful deletion of Task5 as it did in the VCN.

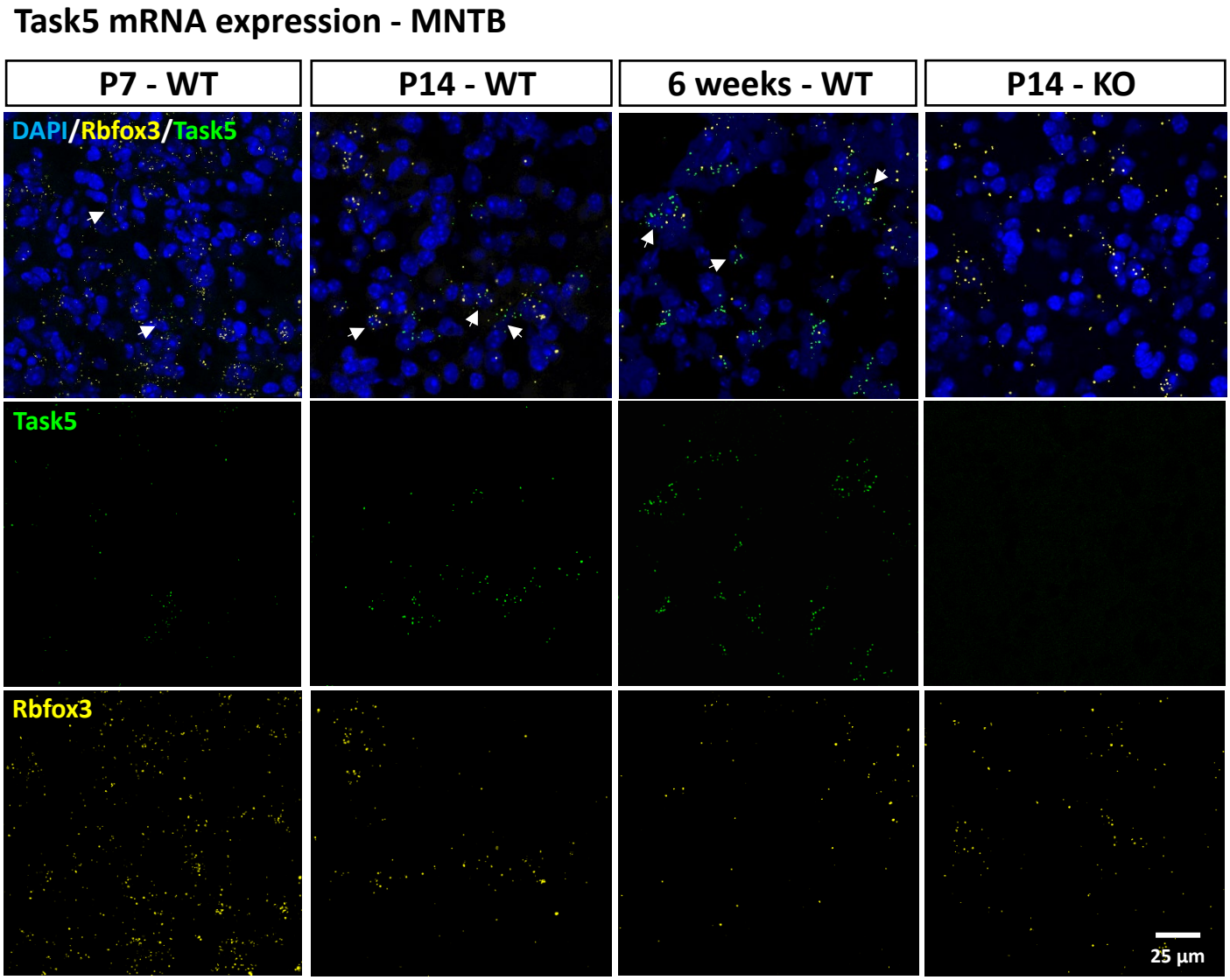

Figure 6: Task5 expression in the MNTB during auditory maturation.
Confocal images of the mouse MNTB show Task5 mRNA is weakly expressed at P7. As observed in the VCN, Task5 expression is upregulated at the onset of hearing and retains this level of expression into ahulthood. Task5 knockout is further confirmed. Arrows indicate colocalization between Task5 and Rbfox3. Scale bar = 25 µm.

3.2. Analysis of antibody-based localization data

3.2.1. Subcellular localization of EGFP-tagged Task5 in cortical neurons

Until today, functional expression of Task5 in heterologous expression systems has not yet been detected (Ashmole et al., 2001; Karschin et al., 2001; Kim and Gnatenco, 2001), and the lack of working antibodies constitutes a major additional difficulty to investigate Task5 expression. To address this issue, Task5 protein was tagged with EGFP at the C-terminus and the second pore domain (P-loop) to trace the subcellular localization by confocal microscopy by co-staining with organelle markers. The failure in detecting Task5 expression could arise from incomplete targeting to the plasma membrane due to intracellular retention. Of special interest is the ER due to a retention motif localized in the amino-terminal part (N-terminal) of the channel (Rajan et al., 2002; Mathie et al., 2010; Zuzarte et al., 2009). Additionally, Task5 localization in mitochondria and the Golgi apparatus was examined. GFP-expression was found in the entire cytoplasm, the nucleus remained devoid of signal. Expression of tagged Task5 protein in primary rat cortical neurons and colocalization with organelle markers revealed poor localization to mitochondria (Fig. 7B) and no localization to the trans-Golgi network (Fig. 7D). Immunostaining against GFP was applied as quality control and demonstrated high colocalization (Fig. 7A). Interestingly, Task5 shows partial localization to the ER (Fig. 7C). In addition to the visual examination of the localization pattern for selected organelle markers, colocalization was quantified by analyzing the plot profile (ImageJ 1.51f), which represents the spatial intensity profile of the region indicated by the white arrow for both fluorescence channels. The arrows have been positioned in such a way that they cover fluorescent signals of both channels to validate potential overlap of elevated fluorescence intensity between channels in relation to background. The plot profile analysis supports the visual evaluation of the immunofluorescence images. The fluorescence intensity plot of immunofluorescence labeling against GFP revealed a very similar intensity pattern. It demonstrates simultaneous increase and decrease in fluorescence intensity. Different intensity patterns were found for immunolabeling against mitochondria and the Golgi apparatus. Partial overlap was found between the fluorescence intensity plots of C-terminal tagged Task5 protein and the ER marker Protein disulfide isomerase (PDI). Same results were obtained with the P2-domain-EGFP-tagged Task5 protein (data not shown).

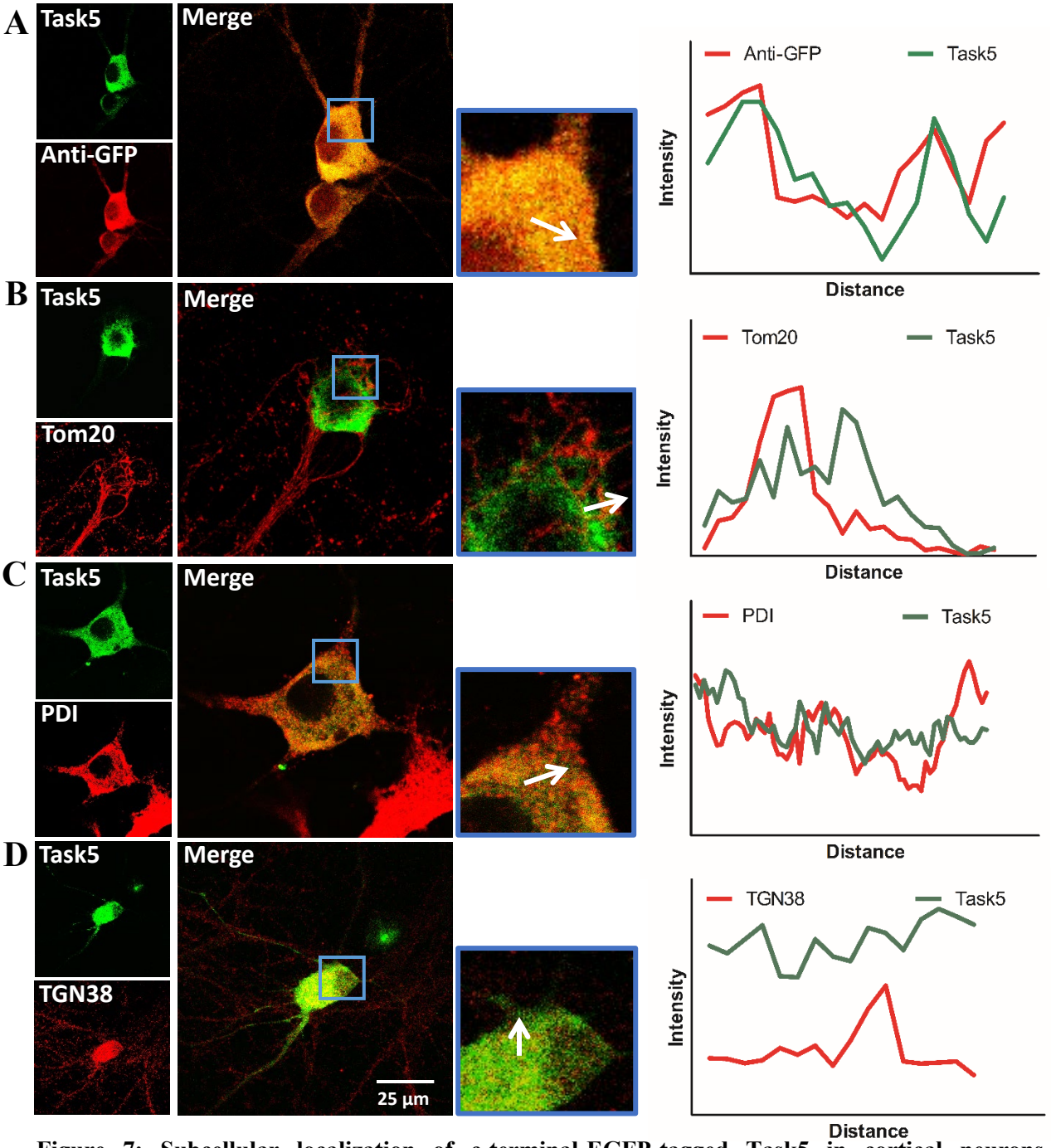

Figure 7: Subcellular localization of c-terminal-EGFP-tagged Task5 in cortical neurons. Primary rat cortical neurons transfected with c-terminal-EGFP-tagged Task5 were immunostained with (**A**) anti-GPF (quality control), (**B**) anti-Tom20 (mitochondrial marker), (**C**) anti-PDI (ER marker) and (**D**) anti-TGN38 (trans Golgi network marker). Images were taken with a Leica TCS SP5 Confocal Laser Scanning Microscope. The middle panel represents magnified views of the blue boxed area in the merged images. The fluorescence intensity profiles across the white arrows in the magnified images are shown in the right panel. Scale bar = 25 µm.

3.2.2. Subcellular localization of EGFP-tagged Task5 in VCN neurons in brain tissue

After examining the distribution pattern of EGFP-tagged Task5 in primary rat cortical neurons, the next logical step consisted of determining the subcellular localization of EGFP-tagged Task5 in brain tissue by expression of the constructs in the VCN of P3 rats. Naturally, Task5 is highly expressed in auditory brainstem neurons but not in the rest of the brain with the exception of the olfactory bulb and the cerebellum (Karschin et al., 2001; Holt et al., 2006). Further, the RNAscope FISH data revealed particularly high Task5 expression in VCN neurons during the onset of hearing at ~P14 (Fig. 5). Representative confocal images show a distribution pattern of EGFP-tagged Task5 that is similar to the distribution pattern in primary rat cortical neurons (Fig. 8). Strong expression is found in the cytoplasm, the nucleus remained unlabeled. Immunolabeling against GFP performed as quality control revealed great overlap between channels (Fig. 8A). As in cultured cortical neurons, no colocalization was found between EGFP-tagged Task5 and the organelle markers Tom20 and TGN38, as evident from the fluorescence intensity profiles across the white arrows (Fig. 8B&D). Unlike previously in primary rat cortical neurons, where the intensity profiles of the ER marker PDI and EGFP-tagged Task5 showed partial overlap, no overlap was detected in the VCN (Fig. 8C). The P2-domain-tagged construct did not functionally express in VCN neurons (data not shown).

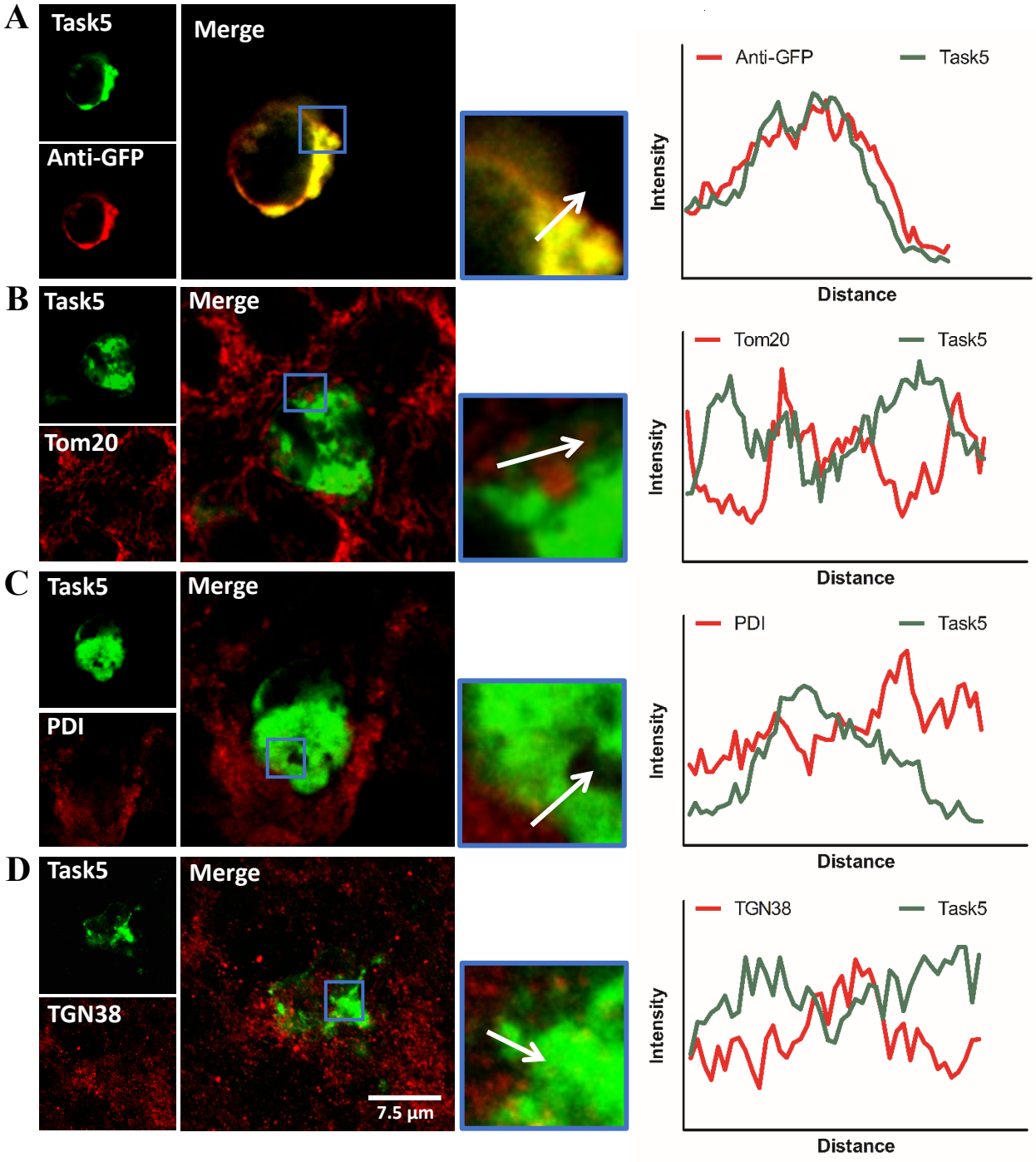

Figure 8: Subcellular localization of c-terminal-EGFP-tagged Task5 in the VCN. C-terminal-EGFP-tagged Task5 was injected into the VCN of P3 rats. Immunolabeling with organelle markers was conducted at P14 against: (**A**) anti-GPF (quality control), (**B**) Tom20 (mitochondrial marker), (**C**) PDI (ER marker) and (**D**) TGN38 (trans Golgi network marker). Images were taken with a Leica TCS SP5 Confocal Laser Scanning Microscope. The middle panel represents magnified views of the blue boxed area in the merged images. The fluorescence intensity profiles across the white arrows in the magnified images are shown in the right panel. Scale bar = 7.5 µm.

3.3. Electrophysiological characterization of Task5

3.3.1. Effects of shRNA-mediated Task5 knockdown on AP waveform generation

To investigate a possible role of Task5 in setting the AP waveform in the MNTB and the VCN, two auditory brainstem nuclei with varying Task5 expression (VCN = high, MNTB = medium-low), Task5 expression was reduced by shRNA expression in the MNTB and the VCN of rats at P3. The effects of shRNA-mediated Task5 knockdown were examined by whole-cell current clamp recordings in acute brainstem slices of P12-P14 rats after the onset of hearing. Moreover, firing pattern phenotype was characterized to further investigate the impact of Task5 on the biophysical properties of auditory neurons. APs were elicited by depolarizing current injections (50 pA step increment, 5 ms duration) and the first AP, which could be induced at threshold current, was quantified. Task5 knockdown in the VCN resulted in changes in the shape of the AP waveform, recorded from GBCs in the VCN. AP amplitude (WT = 79.56 ± 3.635 mV N=20; KD = 65.99 ± 3.583 mV N=18; p = 0.0119; unpaired t-test; Fig. 9E) was significantly reduced, while time to peak (WT = 4.281 ± 0.2184 ms N=20; KD = 5.209 ± 0.3181 ms N=18; p = 0.0194; unpaired t-test; Fig. 9D) and full-width-at-half maximum (FWHM; WT = 1.193 ± 0.06349 ms N=20; KD = 1.670 ± 0.1429 ms N=18; p = 0.0032; unpaired t-test; Fig. 9F) were significantly increased after knockdown of Task5 in the GBCs. Moreover, the RMP was more depolarized (WT = -52.17 ± 1.863 mV N=20; KD = -46.81 ± 1.428 mV N=18; p = 0.0312; unpaired t-test; Fig. 9C). The shift towards a more positive RMP after Task5 knockdown is in line with the conventional role of K2P channels, which is the maintenance of the negative resting membrane potential (O'Connell et al., 2002). GBCs were identified via their large size, as well as the characteristic dendritic branching and their localization in the AVCN (Smith et al., 1991; Bazwinsky et al., 2008). Task5 knockdown phenotype could be rescued successfully by exogenous shRNA resistant Task5 protein. Biocytin-filled GBCs in the AVCN labeled with streptavidin coupled to Alexa647 are shown in Fig. 9A and meet the criteria described before, confirming their identity as GBCs.

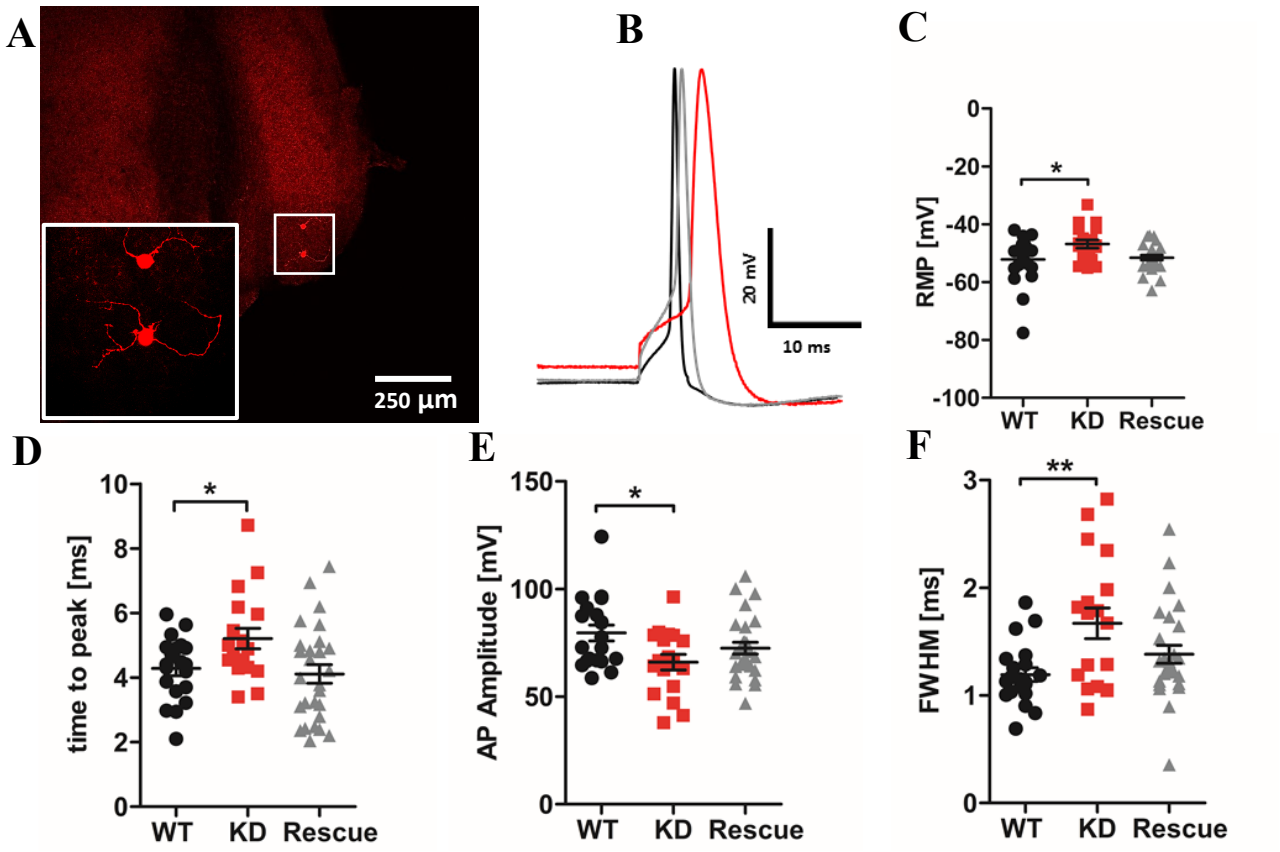

Figure 9: AP waveform properties of GBCs after Task5 knockdown. Task5 knockdown in the VCN results in changes in the AP waveform. (**A**) The inset shows the magnified view of the boxed area in the single confocal image, representing the maximum projection of confocal stack of the AVCN of two GBCs filled with biocytin during intracellular recordings. Scale bar = 250 µm. (**B**) Representative evoked single APs in response to depolarizing current steps. (**C-F**) In the VCN, the GBCs (n = WT [20], KD [18], Rescue [27]) exhibited significantly increased time to peak and FWHM while AP amplitude was significantly reduced following knockdown. RMP was found to be more depolarized. Data is displayed as mean ± SEM. * $p < 0.05$ and ** $p < 0.01$.

Similar results were obtained from MNTB principal cells after Task5 knockdown (Fig. 10). RMP was significantly depolarized (WT = -53.79 ± 1.194 mV N=27; KD = -49.30 ± 1.953 mV N=17; p = 0.0437; unpaired t-test; Fig. 10B) whereas time to peak (WT = 4.322 ± 0.2844 ms N=27; KD = 5.284 ± 0.3347 ms N=17; p = 0.0369; unpaired t-test; Fig. 10C) and FWHM (WT = 4.322 ± 0.2844 ms N=27; KD = 5.284 ± 0.3347 ms N=17; p = 0.0369; unpaired t-test; Fig. 10E) significantly increased after knockdown. Unlike in the VCN, AP amplitude remained statistically unchanged (Fig. 10D). The MNTB contains a homogeneous population of neurons, hence it is not required to distinguish MNTB principal cells from other cell types of the MNTB. In general, the effects of Task5 knockdown were more pronounced in the VCN as compared to the MNTB.

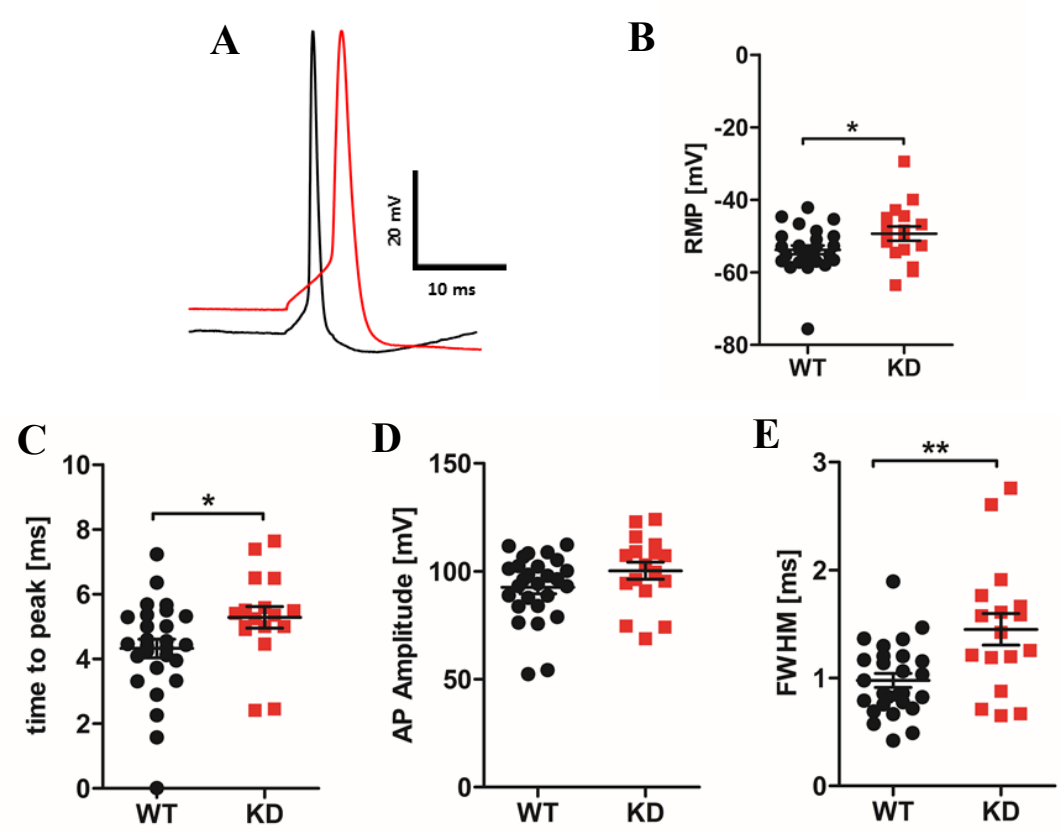

Figure 10: AP waveform properties of MNTB principal cells after Task5 knockdown. Task5 knockdown changed AP waveform properties in the MNTB. (**A**) Representative evoked single APs in response to depolarizing current steps. (**B-E**) In the MNTB (n = WT [27], KD [17]), the knockdown of Task5 significantly increased time to peak and FWHM and significantly depolarized RMP. AP amplitude remained unchanged. Data is displayed as mean ± SEM. * $p < 0.05$ and ** $p < 0.01$.

3.3.2. Effects of shRNA-mediated Task5 knockdown on firing pattern generation

To determine if Task5 knockdown leads to changes in firing pattern, long depolarizing current injections (20 pA steps) were delivered (Fig. 11). After Task5 knockdown in the VCN, GBCs required less injected current to fire an AP (WT = 91.76 ± 12.25 pA N=17; KD = 53.75 ± 7.465 pA N=16; p = 0.0138; unpaired t-test; Fig. 11B) and exhibited increased number of APs 60 pA above threshold (WT = 3.579 ± 0.6227 N=19; KD = 4.889 ± 0.7579 N=18; p = 0.1884; unpaired t-test; Fig. 11C), but the latter difference was not statistically significant. Due to this trend towards increased AP firing in response to Task5 knockdown, the input (the intensity of injected current)/output (Nr. of APs) (I/O) curve was determined (Fig. 11A). Comparison of I/O curves was assessed using two-way ANOVA followed by Bonferroni's post hoc test at each magnitude of current injection. The I/O curve revealed that more APs are fired with increasing current

injection and the shift towards increased AP firing was found to be statistically significant, suggesting increased neuronal activity. Most interestingly, the initial onset-AP firing pattern upon depolarization of the GBCs (Wu and Oertel, 1984) was disrupted in the absence of Task5. GBCs predominantly fired tonically after the knockdown of Task5 (Fig. 11D-F). About 58% of the GBCs fired tonically prior to Task5 knockdown. After Task5 knockdown, the percentage of tonic firing increased from 58% to 89%. Rescue experiments highlight this effect of Task5 knockdown on the firing pattern. The rescue construct not only restored the balance between tonic and phasic release, but it even shifted the release pattern in the opposite direction of the acquired results in the absence of Task5. Merely 31% of rescued GBCs fired tonically. Furthermore, rheobase current (minimal current injected to evoke an AP) (108.3 ± 13.72 pA) and APs at 60 pA above threshold (2.692 ± 0.5226) were rescued (Fig. 11B&C). The number of APs with increasing current injection decreased to even smaller values than WT (Fig. 11A).

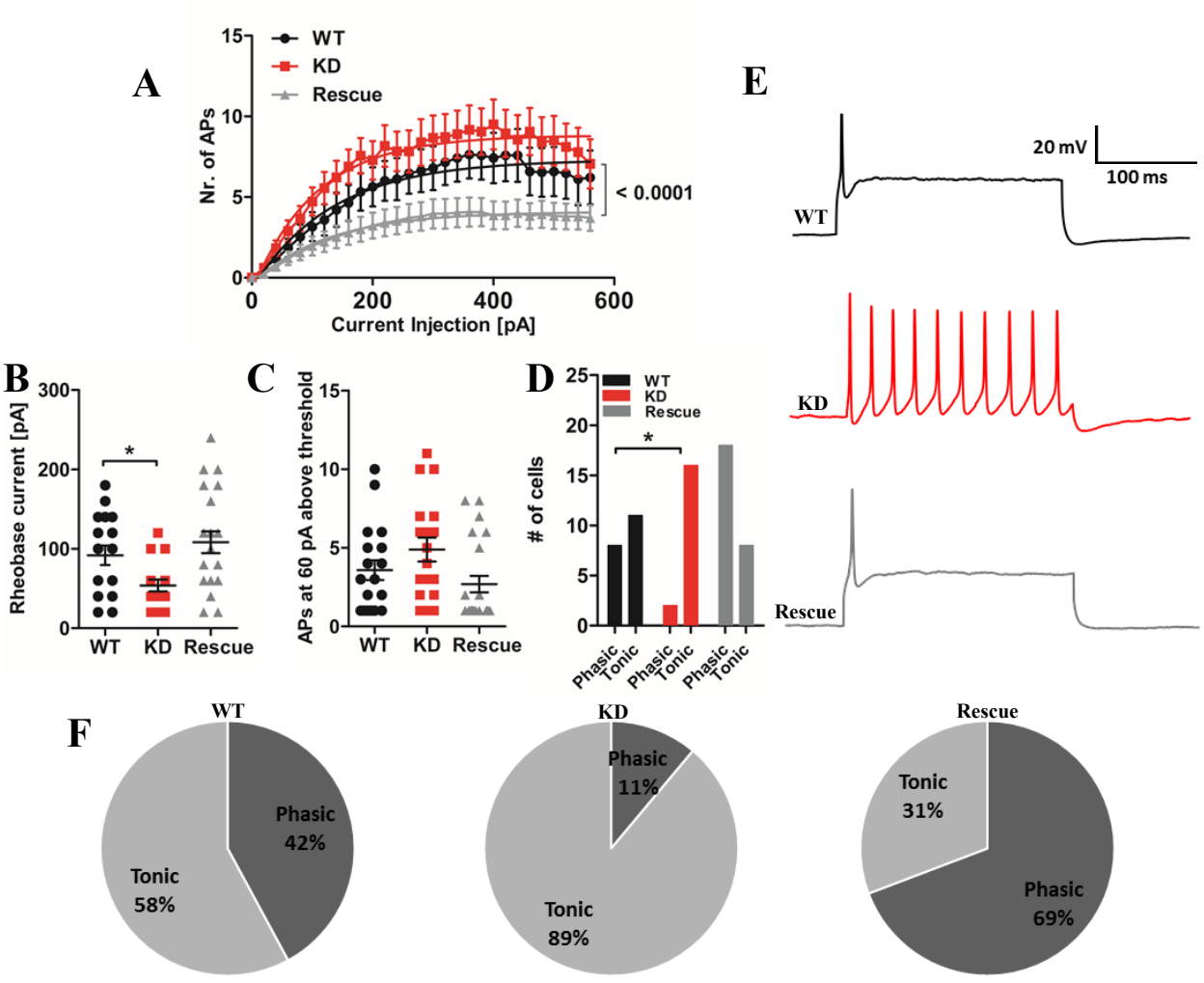

Figure 11: Firing pattern analysis of GBCs after Task5 knockdown.
(A) I/O curves are significantly different between groups. (**B**) Depolarizing long current injection (20 pA steps) in GBCs revealed reduced threshold to fire the first AP after knockdown. (**C**) No significant difference was found in the number of APs at 60 pA above threshold in the VCN. (**D**) In the absence of Task5, GBCs preferentially fired tonically. This change in firing pattern behavior was successfully rescued. (**E**) Representative AP traces from 200 pA depolarizing current injection in WT, KD and rescued GBCs. (**F**) After knockdown, more GBCs fired tonically (89%) compared to WT neurons (58%). (n = WT [17-19], KD [16-18], Rescue [24-26]). Data is displayed as mean ± SEM. * $p < 0.05$.

Contrary to the VCN, the effects of Task5 knockdown on firing behavior in the MNTB were almost non-existent (Fig. 12). Task5 knockdown in the MNTB resulted in a reduction of rheobase current (WT = 96.67 ± 13.76 pA N=24; KD = 58.57 ± 9.713 pA N=14; p = 0.0592; unpaired t-test; Fig. 12A). However, it failed to demonstrate statistical significance. Equally, APs at 60 pA above threshold were very comparable between genotypes (WT = 5.179 ± 0.8730 N=28; KD = 5.700 ± 1.140 N=20; p = 0.7137; unpaired t-test; Fig. 12B). Unlike in previous studies (Banks and Smith, 1992), MNTB principal cells exhibited increased tonic firing and this release pattern was maintained after knockdown of Task5. About 79% of WT MNTB cells fired tonically and this value increased to 90% without reaching statistical significance (Fig. 12C&D).

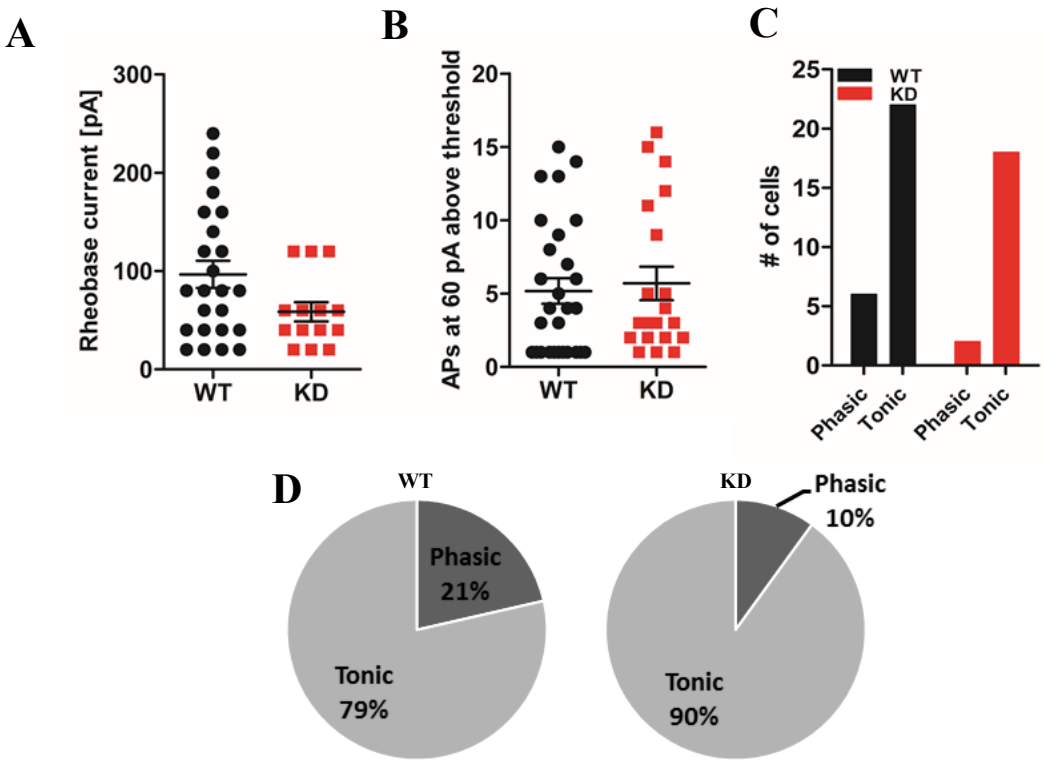

Figure 12: Firing pattern analysis of MNTB principal cells after Task5 knockdown. (**A**) Depolarizing long current injection (20 pA steps) in MNTB principal cells (n = WT [24], KD [14]) reveals reduced threshold to fire the first AP after knockdown without statistical significance. (**B**) No significant difference was found in the number of APs at 60 pA above threshold. (**C-D**) WT tonic release pattern is maintained after knockdown of Task5. Data is displayed as mean ± SEM.

3.3.3. Identification of the Task5-knockout mouse

To investigate the relevance of Task5 in addition to the knockdown, a Task5-KO mouse-line was generated using mutant (mutation = Velocigene deletion of the entire Task5 gene) sperm purchased from the Knockout Mouse Project (KOMP) Repository. Successful Task5 knockout was confirmed by PCR analysis (Fig. 13). Additionally, successful generation of homozygous mice lacking functional Task5 gene was confirmed by the RNAscope assay, the results of which are presented in 3.1.

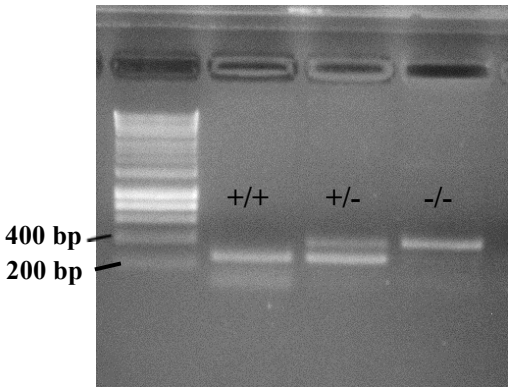

Figure 13: Genotyping of the Task5 knockout mouse.
PCR genotyping of Task5 WT (+/+), heterozygous (+/-) and homozygous (-/-) mice.

3.3.4. Effects of Task5 knockout on AP waveform generation

After examining the effects of Task5 knockdown in the VCN and MNTB on AP waveform generation and firing pattern behavior, the next step was to investigate the impact of permanently inactivated Task5 in the whole animal. Constitutive Task5-KO mice were generated using ES cells with deleted Task5 gene. Differently than expected, the same current clamp recordings as performed in KD rats revealed no effects of Task5 deletion on AP waveform generation in Task5-KO VCN neurons (Fig. 14), which is in stark contrast to Task5 knockdown (Fig. 9). RMP (WT = -54 ± 0.9820 mV N=30; KO = -51.37 ± 1.053 mV N=31; p = 0.0730; unpaired t-test; Fig. 14B), time to peak (WT = 4.106 ± 0.2179 ms N=30; KO = 3.910 ± 0.1602 ms N=31; p = 0.4709; unpaired t-test; Fig. 14C), AP amplitude (WT = 72.03 ± 3.490 mV N=30; KO = 64.52 ± 3.621 mV N=31; p = 0.1413; unpaired t-test; Fig. 14D) and FWHM (WT = 1.163 ± 0.08986 ms N=30; KO = 1.162 ± 0.09277 ms N=31; p = 0.9903; unpaired t-test; Fig. 14E) remained unaffected by Task5 knockout.

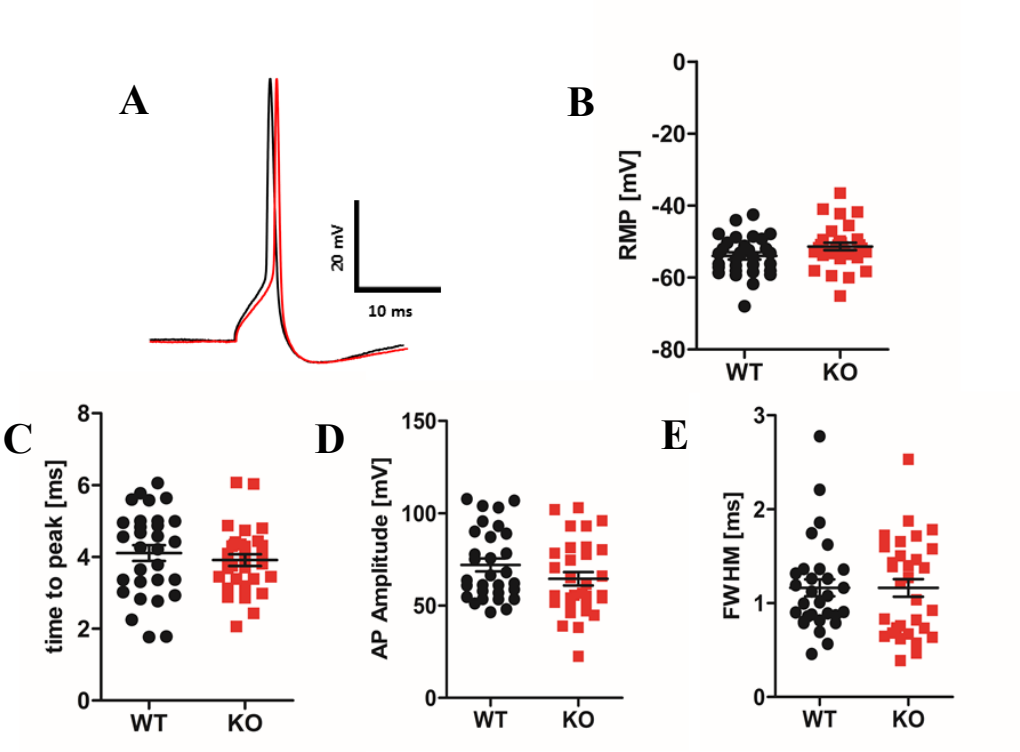

Figure 14: AP waveform properties of GBCs after Task5 knockout. Task5 knockout exhibited no changes in AP waveform properties in the VCN when Task5 was deleted. (**A**) Representative evoked single APs in response to depolarizing current steps. (**B-E**) Task5 knockout in the VCN did not affect AP waveform (RMP, time to peak, AP amplitude and FWHM) of recorded GBCs (n = WT [30], KO [31]). Data is displayed as mean ± SEM.

Similar results were obtained from recordings in the MNTB (Fig. 15). Task5 knockout had no impact on RMP (WT = -58.24 ± 0.8286 mV N=32; KO = -57.48 ± 1.038 mV N=28; p = 0.5645; unpaired t-test; Fig. 15B), time to peak (WT = 3.928 ± 0.1705 ms N=32; KO = 4.067 ± 0.2307 ms N=28; p = 0.6237; unpaired t-test; Fig. 15C), AP amplitude (WT = 90.38 ± 2.062 mV N=32; KO = 89.07 ± 2.585 mV N=29; p = 0.6927; unpaired t-test; Fig. 15D) and FWHM (WT = 0.6955 ± 0.03434 ms N=30; KO = 0.6542 ± 0.03566 ms N=29; p = 0.4079; unpaired t-test; Fig. 15E). These results suggest differential behaviors of auditory brainstem nuclei cells after Task5 knockdown and knockout.

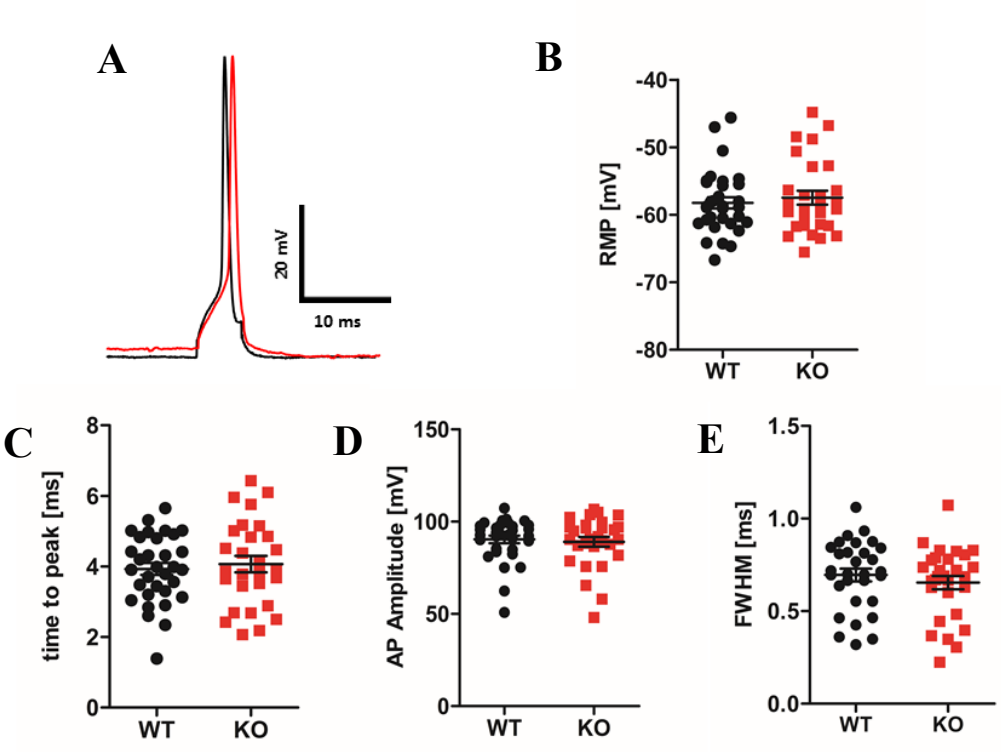

Figure 15: AP waveform properties of MNTB principal cells after Task5 knockout. Task5 knockout exhibited no changes in AP waveform properties in the MNTB when Task5 was deleted. (**A**) Representative evoked single APs in response to depolarizing current steps. (**B-E**) Task5 knockout in the MNTB did not affect AP waveform (RMP, time to peak, AP amplitude and FWHM) of recorded MNTB cells (n = WT [30-32], KO [28-29]). Data is displayed as mean ± SEM.

3.3.5. Effects of Task5 knockout on firing pattern generation

Task5 knockdown in the VCN resulted in changes of intrinsic electrical properties of GBCs, visible in altered firing pattern behavior (Fig. 11). The results obtained from the AP waveform analysis of Task5-KO mice already gave us some idea of the effects of Task5 deletion on the release pattern. As expected, Task5 knockout did neither affect the rheobase current (WT = 121.3 ± 12.24 pA N=30; KO = 122.4 ± 12.45 pA N=33; p = 0.9505; unpaired t-test; Fig. 16A) nor the number of APs at 60 pA above threshold (WT = 4.767 ± 1.027 N=30; 4.515 ± 0.9762 N=33; p = 0.8597; unpaired t-test; Fig. 16B) suggesting no impact of Task5 on cell excitability after complete Task5 gene loss. The I/O relation shows almost perfect overlap between WT and KO (Fig. 16C) cells. As previously observed after Task5 knockdown (Fig. 11D-F), the firing pattern shifted from a balanced phasic-tonic firing behavior to a more dominant tonic firing. Tonic firing increased from 50% to 70%, but this difference was not found to be statistically significant (Fig. 16D&E).

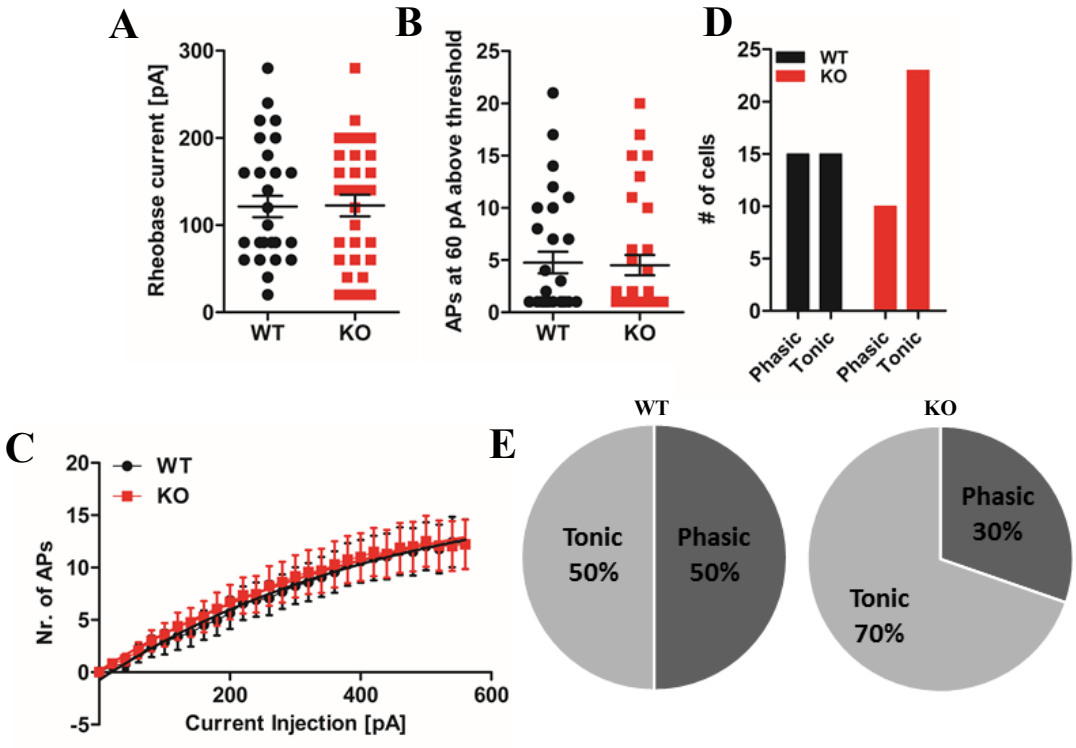

Figure 16: Firing pattern analysis of GBCs after Task5 knockout. (**A**) The rheobase current, (**B**) APs at 60 pA above threshold and (**C**) the number of APs with increasing current intensity recorded from GBCs (n = WT [30], KO [33]) in the VCN were not different. (**D-E**) The release pattern shifted to a more tonic firing pattern. Data is displayed as mean ± SEM.

The effects of Task5 knockdown on MNTB principal cells were comparatively moderate (Fig. 10 &12), therefore it came as no surprise that Task5 knockout did not change their response pattern (Fig. 17), especially after we found that the GBCs remained unaffected by complete Task5 deletion (Fig. 14&16). Both, the rheobase current (WT = 79.35 ± 8.822 pA N=31; KO = 66.21 ± 7.301 pA N=29; p = 0.2591; unpaired t-test; Fig. 17A) and APs at 60 pA above threshold (WT = 6.344 ± 1.052 N=32; KO = 6.071 ± 1.076 N=28; p = 0.8574; unpaired t-test; Fig. 17B) were not different between WT and KO cells. Unlike previous reports of single AP response pattern of MNTB cells (Banks and Smith, 1992; Wang et al., 1998), the already existing tonic firing in WT cells was maintained after Task5 knockout (Fig. 17C&D).

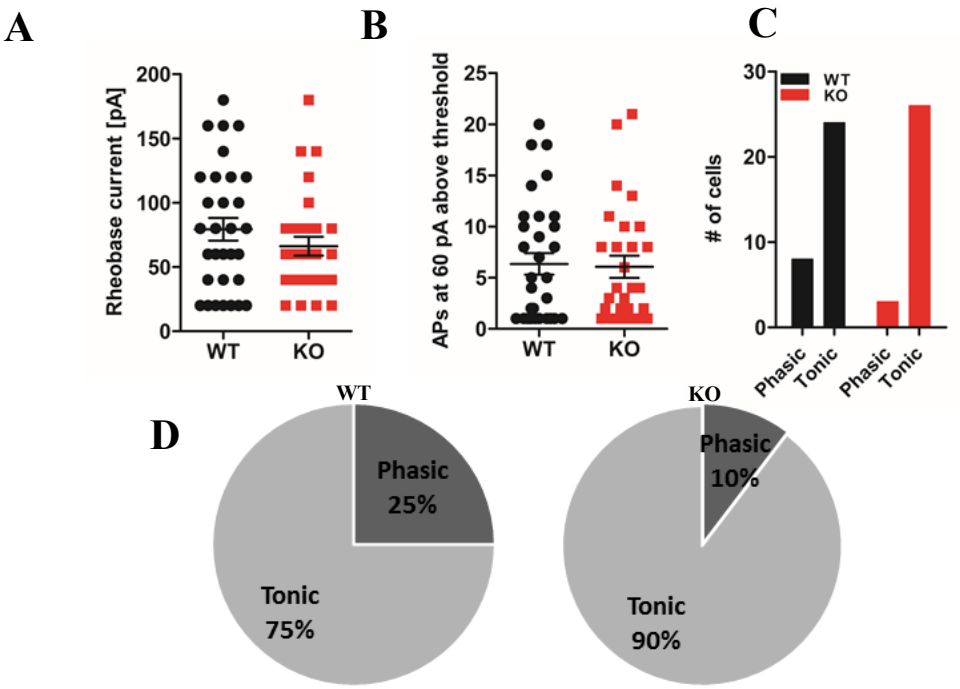

Figure 17: Firing pattern analysis of MNTB principal cells after Task5 knockout. (**A**) Rheobase current and (**B**) APs at 60 pA above threshold were not different in the MNTB (n = WT [31-32], KO [28-29]). (**C&D**) The increase from 75% to 90% tonic firing did not meet statistical significance. Data is displayed as mean ± SEM.

3.3.6. Input Resistance as a measurement for genetic compensation in response to gene knockout

The obtained results from firing pattern and AP waveform analysis revealed significant changes in firing behavior in the MNTB (Fig. 10) and the VCN (Fig. 9&11), when Task5 expression was downregulated by shRNA-mediated gene silencing in the respective auditory brainstem nuclei. Yet, the same type of recordings from the MNTB and the VCN after constitutive Task5 knockout revealed no influence of Task5 on the recorded properties (Fig. 14-17). This discrepancy between KD and KO results suggests genetic compensation, which is a well-known phenomenon (e.g. El-Brolosy and Stainier, 2017). However, its underlying mechanisms are not well enough studied. It seems likely, that genetic compensation in response to Task5 knockout may arise from another potassium channel that has overlapping functions and/or expression pattern within the auditory brainstem. As a first approach to answer the question whether genetic compensation is in fact the reason for these contradictory observations between the two types of genetic manipulation, the input resistance was measured to compare the extent of open channels between genotypes (Fig. 18). Input resistance was assessed in current clamp mode as the slope of the linear regression of the V-I curves, determined from subthreshold current injection. Data was collected at the end of the voltage response. The linear regression of the V-I curve demonstrated huge difference between WT and KO neurons (Fig. 18B). Input resistance was found to be significantly reduced in the absence of Task5 in the VCN recorded from GBCs (WT = 186.3 ± 24.44 MΩ N=29; KO = 107.8 ± 10.16 MΩ N=27; p = 0.0055; unpaired t-test; Fig. 18B), indicating more open channels in Task5 deficient cells. These findings support the assumption that genetic compensation led to diminishing any effect of Task5 knockout on electrophysiological properties.

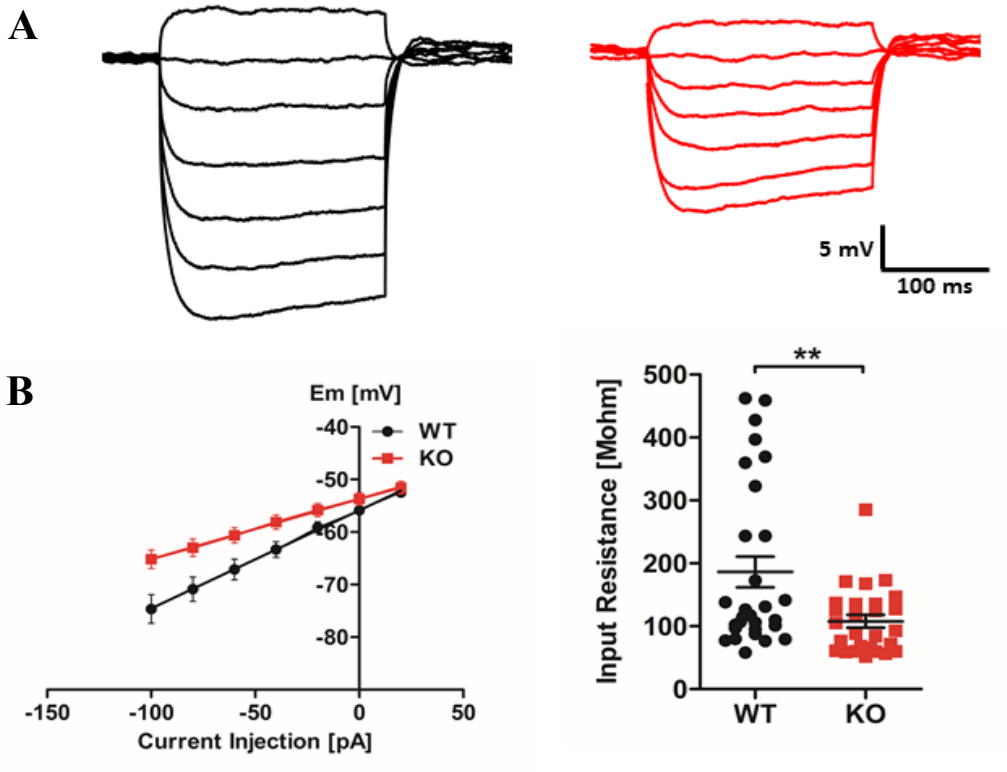

Figure 18: Comparison of membrane input resistance of GBCs between WT and Task5-KO cells. (**A**) Examples of the membrane response of a WT (black trace) and Task5-KO (red trace) GBC in response to current injection from -100 pA to 20 pA in 20 pA steps. (**B**) Membrane V-I relationship was examined in WT [n = 29] and Task5-KO [n = 28] cells. Task5 deficient GBCs exhibited significantly lower input resistance, indicating more open channels. Data is displayed as mean ± SEM. ** $p < 0.01$.

3.3.7. Measurement of isolated outward K^+ currents

Based on the significant reduction of input resistance in the absence of Task5 in the GBCs (Fig. 18B), which suggests more open channels, we sought to find out, whether another potassium channel might be involved in compensating for the loss of Task5. For this purpose, voltage-gated outward K^+ currents were evoked during 100 ms depolarizing voltage steps at potentials between -100 mV and 45 mV in 5 mV voltage steps from a holding potential of -70 mV (Fig. 19). Potassium currents were isolated by blocking voltage-activated Na^+ currents using TTX (1 µM) and voltage-activated Ca^{2+} currents using $CdCl_2$ (250 µM). WT and Task5-KO cells exhibited robust outward rectification. Typical current traces for WT and KO GBCs are presented in figure 19A. Both genotypes exhibited rapidly activating outward K^+ currents, that steadily increased with depolarization. The majority of WT GBCs showed a biphasic outward current consisting of a transient inactivating component probably mediated by Kv1 channels followed by a non-

inactivating component mediated by Kv3 channels (Rothman and Manis, 2003a;b). In most KO cells, the transient outward component was less pronounced or completely absent. Currents were normalized to current density (pA/pF) and plotted against the membrane potential. Both, peak- and steady-state I-V relationships were plotted. I-V curves show very similar properties with the difference that KO cells already reached a plateau at ~ 25 mV, whereas WT I-V curves were still rising (Fig. 19B). Furthermore, the steady-state/peak ratio was calculated (WT = 0.7314 ± 0.02214 N=22; KO = 0.8496 ± 0.01698 N=23; p = 0.0001; unpaired t-test), which revealed a significantly increased ratio for KO cells (Fig. 19C). An increased ratio indicates that peak- and steady-state values are closer together. This finding suggests that, the composition of voltage-activated potassium channels is significantly different in Task5 deficient GBCs.

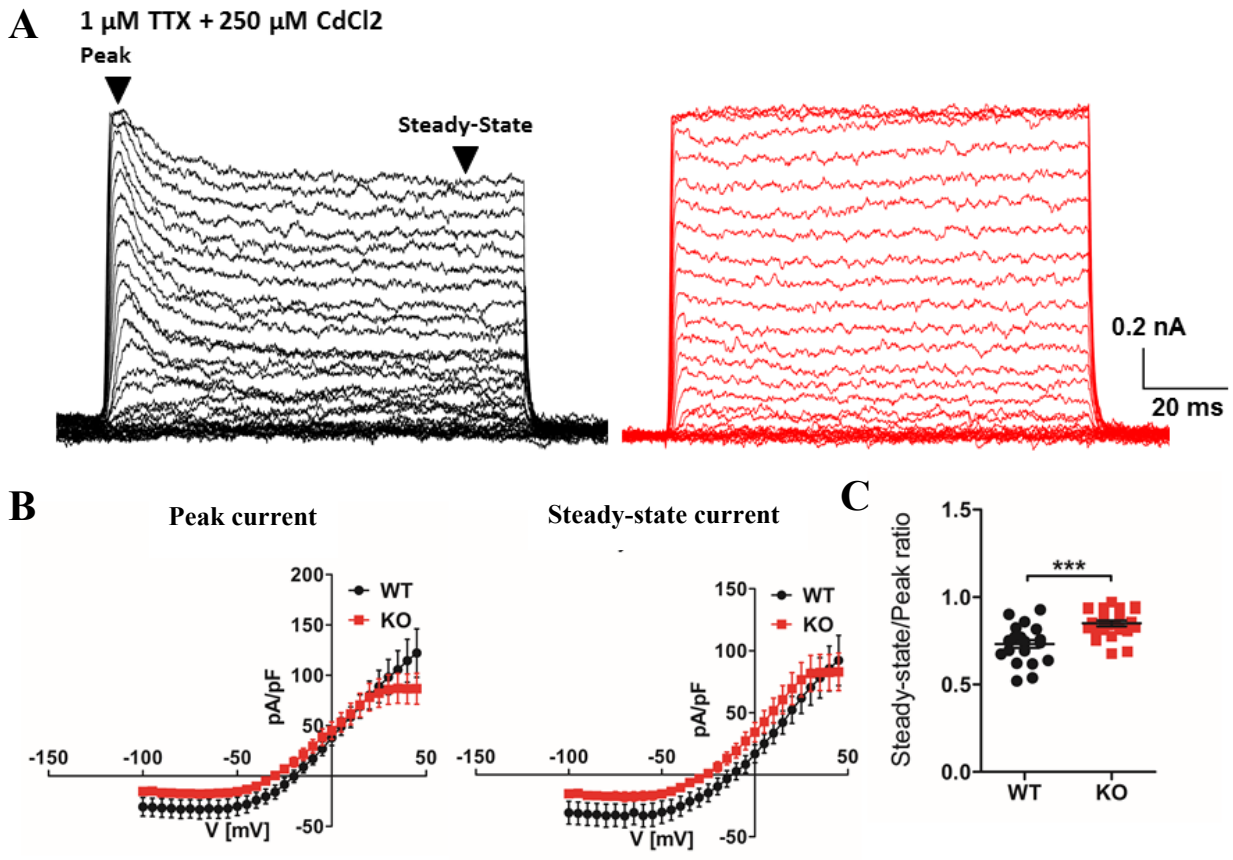

Figure 19: K^+ currents recorded from GBCs.
(A) Representative recordings of outward K^+ currents from WT and Task5-KO GBCs in the presence of TTX (1 µM) and $CdCl_2$ (250 µM). **(B)** I-V relationships of the peak- and steady-state outward K^+ current indicated by the black arrowheads in A (n = WT [22], KO [25]). **(C)** Steady-state/Peak-ratio is significantly increased in KO cells. Data is displayed as mean ± SEM. *** $p < 0.001$.

3.3.8. HCN channel activation by membrane hyperpolarization

The members of the hyperpolarization-activated cyclic nucleotide-gated cation channel (HCN) family contribute to setting the resting membrane potential by hyperpolarization-activated cation currents (Banks et al., 1993; Bal and Oertel, 2000) and are expressed in the VCN (Koch et al., 2004). These overlapping functions and the expression within the auditory brainstem raise suspicion of HCN channels compensating for the loss of Task5. In order to examine the involvement of the HCN family in compensating for the loss of Task5, GBCs were injected with hyperpolarizing current of -200 pA (200 ms) to induce hyperpolarization evoked sag potentials. The sag ratio (Fig. 20B) was calculated by dividing the steady state voltage by the maximum voltage deflection (peak sag). The percentage of cells displaying a voltage sag was identical between genotypes (Fig. 20A). 31% of both, WT and KO GBCs, failed to show the classical voltage sag. The sag ratio was slightly reduced in Task5 deficient cells, however without reaching statistical significance (WT = 1.188 ± 0.02633 N=20; KO = 1.138 ± 0.01946 N=24; p = 0.1246; unpaired t- test). Based on these findings, it seems unlikely that HCN channels are compensating for the loss of Task5.

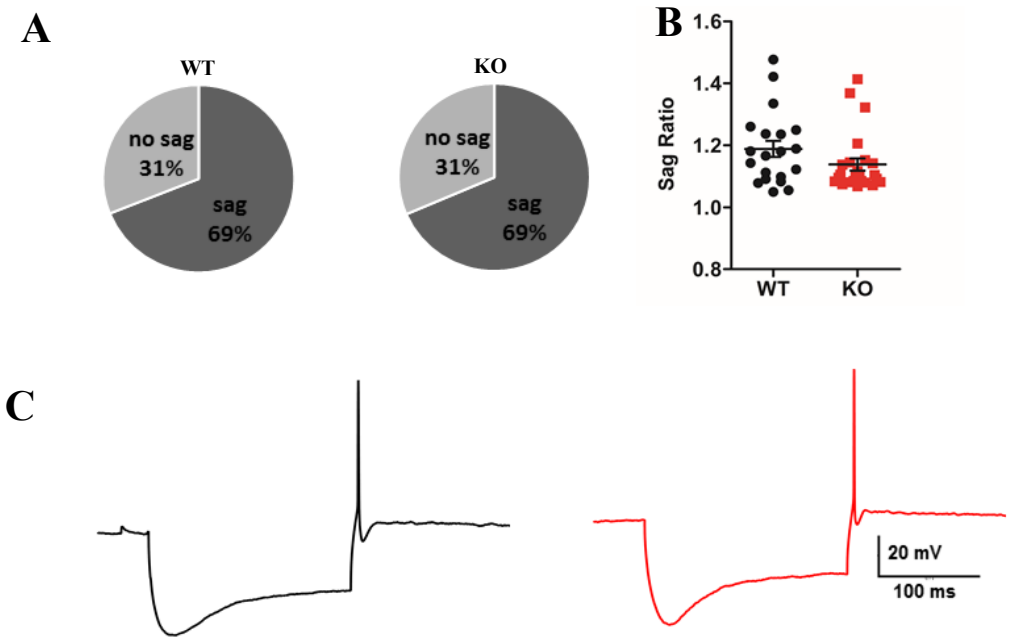

Figure 20: Effects of hyperpolarizing current on GBCs in the VCN.
(**A**) The majority of GBCs of both genotypes exhibited a prominent voltage sag in response to hyperpolarizing current. The distribution percentage of cells showing a voltage sag was identical between WT and Task5 deficient GBCs. (**B**) Sag ratio was not significantly different between genotypes (n = WT [20], KO [24]). (**C**) Whole-cell current clamp responses from a WT (black) and Task5-KO (red) GBC to hyperpolarizing current injection of -200 pA. Data is displayed as mean ± SEM.

3.4. Hearing assessments

3.4.1. Auditory brainstem responses in Task5 deficient mice

To gain insight into the role of Task5 in auditory function and hearing sensitivity, we assessed the functional consequences of the loss of Task5 for acoustic information processing in adult mice (6-8 weeks of age; WT: n = 6 mice, 12 ears; KO: n = 7 mice, 14 ears). For this reason, we measured ABRs and DPOAEs. Figure 21 shows averaged ABR waveforms at 90 dB SPL in the first 10 ms after stimulation, evoked by click-, noise-burst- and high frequency (16 kHz) stimuli. Each positive peak of the generated ABR wave reflects activity in different parts of the ascending auditory pathway and is numbered with Roman numerals I-VI; wave I is generated by the AN, wave II by the CN, wave III by the SOC and wave IV by the lateral lemniscus (Melcher and Kiang, 1996; Rüttiger et al., 2017). In addition, the wave I/O growth function was generated with reference to ABR thresholds (from 0 to a maximum of 90 dB above threshold in 5 dB steps) to assess possible differences in wave development with increasing stimulus level. Compared to noise-burst stimuli, which contain higher frequencies (>10 kHz) of the hearing range of a mouse, click stimuli contain lower frequencies (Wolter et al., 2018). 16 kHz stimuli were applied to test the most sensitive hearing frequency for mice (Koay et al., 2002). Noise-burst stimuli generated the highest wave amplitudes closely followed by click stimuli, whereas 16 kHz stimuli generated the lowest wave amplitudes. The super-imposed averaged click-, noise-burst- and 16 kHz-evoked ABRs show overlap of wave amplitudes between WT and Task5-KO mice with exception of the commencing waves and in particularly wave I for all three testing conditions (Fig. 21 A-C left panel). The wave I/O growth functions for noise-burst- and 16 kHz stimuli exhibit high overlap between genotypes, whereas the growth functions for click stimuli suggest potential alterations in Task5 deficient mice (Fig. 21A-C right panel).

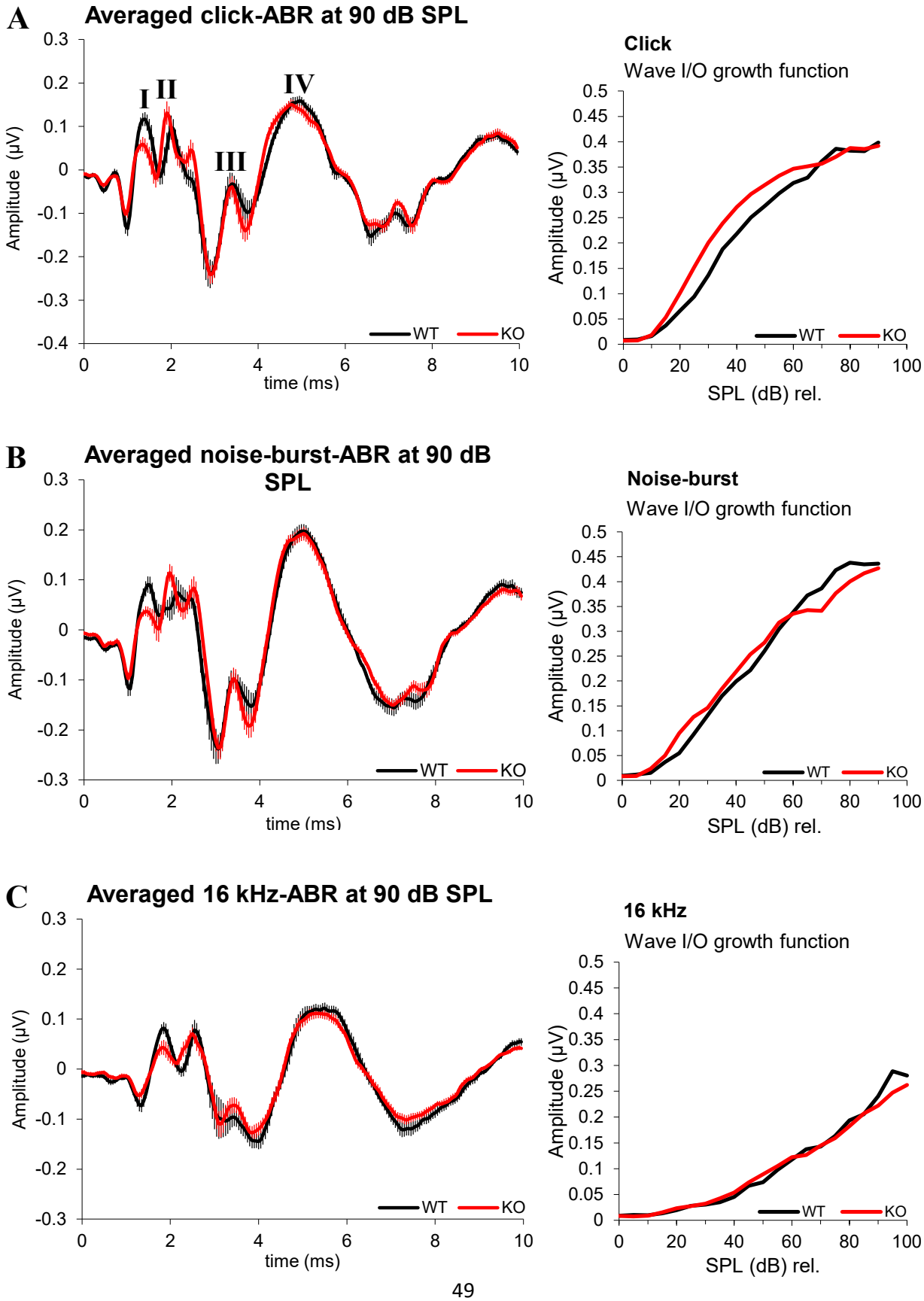
A
Averaged click-ABR at 90 dB SPL
I
II
III
IV
Amplitude (µV)
time (ms)
WT
KO
Click
Wave I/O growth function
Amplitude (µV)
SPL (dB) rel.
WT
KO
B
Averaged noise-burst-ABR at 90 dB SPL
Amplitude (µV)
time (ms)
WT
KO
Noise-burst
Wave I/O growth function
Amplitude (µV)
SPL (dB) rel.
WT
KO
C
Averaged 16 kHz-ABR at 90 dB SPL
Amplitude (µV)
time (ms)
WT
KO
16 kHz
Wave I/O growth function
Amplitude (µV)
SPL (dB) rel.
WT
KO

Figure 21: ABR waveform generation in response to sound exposure.
(**A-C**) Average ABR waveforms (n = WT [6 mice, 12 ears], KO [7 mice, 14 ears]) in response to click-, noise-burst- and 16 kHz stimuli at stimulation level 90 dB SPL (left panel) and the corresponding wave I/O growth functions. Data is displayed as mean ± SEM.

To determine differences between genotypes, ABR wave amplitudes were analyzed from click-, noise-burst- and 16 kHz-evoked ABRs for increasing stimulus levels. ABR wave amplitude growth functions were constructed for increasing stimulus levels, normalized to the individual ABR threshold (from -40 to a maximum of 90 dB above threshold). Strength and slope of each growth function was compared between genotypes (Fig. 22) with strength representing the maximum amplitude. The slope of the growth functions above threshold was assessed via linear regression. Growth functions of click-evoked ABR wave I, III and IV amplitudes were significantly different between genotypes (Fig. 22A-D left panel; ABR wave I: $p = 0.0007$, $F(1,376) = 11.55$; ABR wave III: $p = 0.0433$, $F(1,357) = 4.11$; ABR wave IV: $p = 0.0021$, $F(1,391) = 9.56$; two-way ANOVA). However, strength and slope of the growth functions were found to be significantly different only for click-evoked ABR wave I (Fig. 22A middle and right panel; strength: WT = 2.663 ± 0.2505 µV N=11; KO = 2.001 ± 0.1472 µV N=15; $p = 0.0238$; slope: WT = 0.03364 ± 0.003636 N=11, KO = 0.0240 ± 0.002350 N=15; $p = 0.0288$; unpaired t-test). Noise- burst-evoked ABR wave I and III amplitude growth functions were significantly reduced in Task5-KO mice, whereas wave II and IV growth functions remained unchanged between genotypes (Fig. 22E-H left panel; ABR wave I: $p = 0.0002$, $F = (1,259) = 14.66$; ABR wave III: $p = 0.0055$, $F = (1,325) = 7.83$; two-way ANOVA). All waves displayed unaltered strength and slope (Fig. 22E-H middle and right panel). As previously in the click- and noise-burst-evoked ABRs, wave I amplitude growth function was significantly reduced for 16 kHz stimuli (Fig. 22I left panel; ABR wave I: $p = 0.0199$, $F(1,292) = 5.48$; two-way ANOVA) with a significant reduction of slope (Fig. 22I right panel; WT = 0.02083 ± 0.001930 µV/dB N=12; 0.01462 ± 0.001831 µV/dB N=13; $p = 0.0284$; unpaired t-test). Significant differences in wave amplitude were limited to wave I only for 16 kHz stimuli. Interestingly, all significant alterations between genotypes show a significant reduction of Task5-KO mice ABR wave amplitudes (Fig. 22A, C, E, G& I) except for wave IV evoked by click stimuli. This wave reflects activity in the lateral lemniscus and is significantly elevated in Task5 deficient mice (Fig. 22D). Taken together, these results suggest a reduction in AN function.

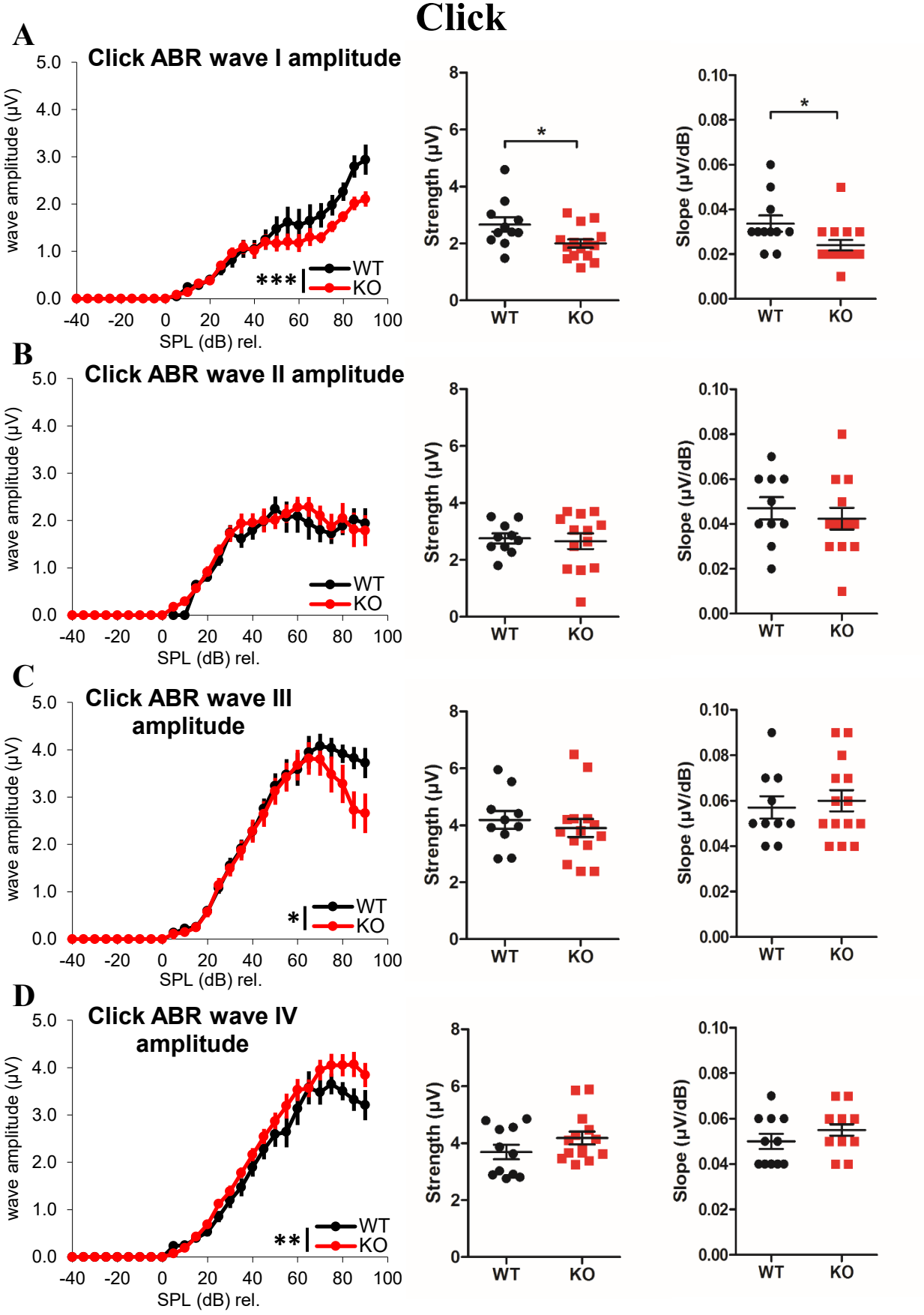
Click
A
Click ABR wave I amplitude
wave amplitude (μV)
SPL (dB) rel.
***
WT
KO
Strength (μV)
*
Slope (μV/dB)
*
B
Click ABR wave II amplitude
C
Click ABR wave III amplitude
*
D
Click ABR wave IV amplitude
**

Noise-burst

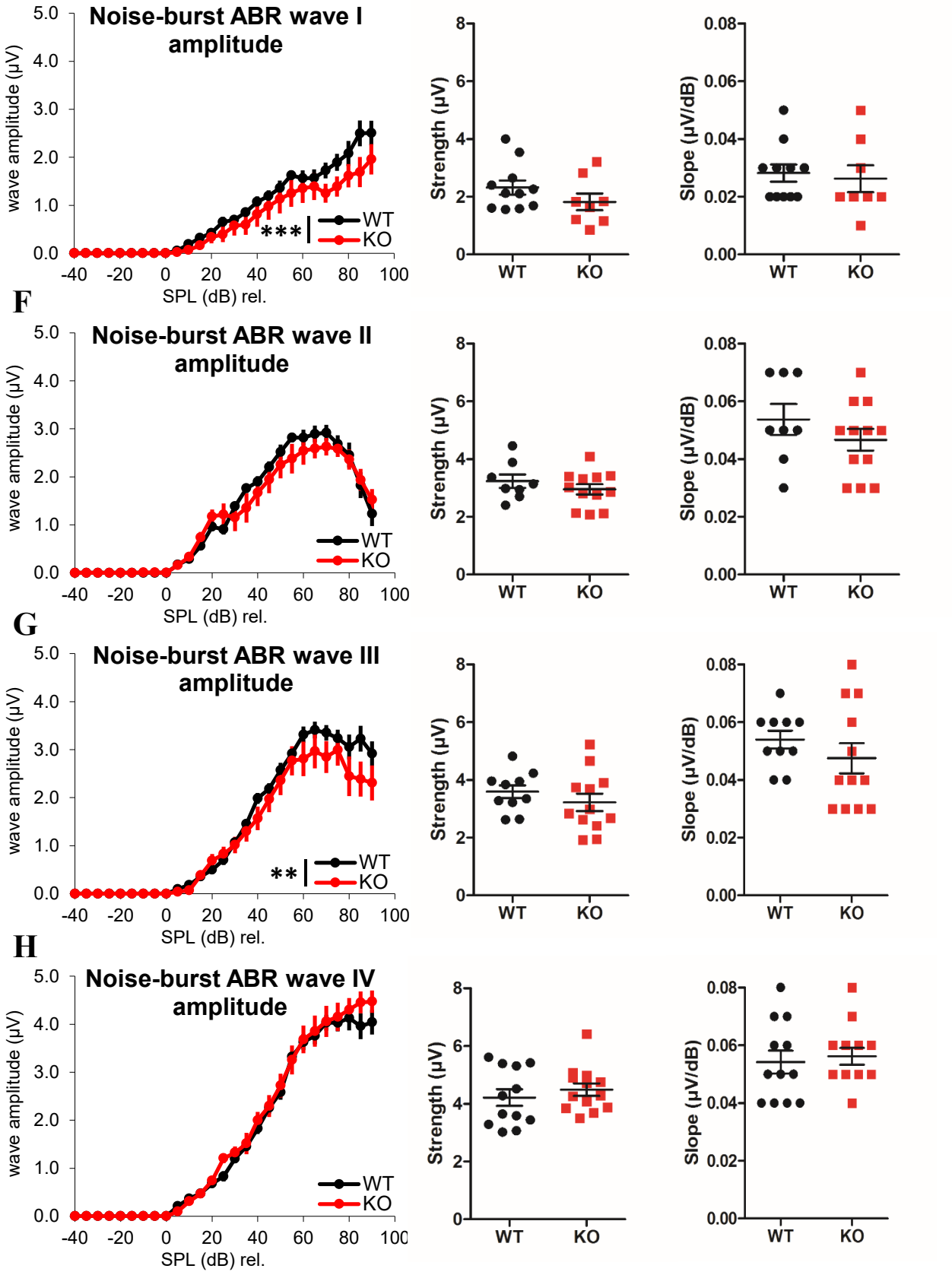
E
Noise-burst ABR wave I amplitude
wave amplitude (µV)
SPL (dB) rel.
***
WT
KO
Strength (µV)
Slope (µV/dB)
F
Noise-burst ABR wave II amplitude
wave amplitude (µV)
SPL (dB) rel.
WT
KO
Strength (µV)
Slope (µV/dB)
G
Noise-burst ABR wave III amplitude
wave amplitude (µV)
SPL (dB) rel.
**
WT
KO
Strength (µV)
Slope (µV/dB)
H
Noise-burst ABR wave IV amplitude
wave amplitude (µV)
SPL (dB) rel.
WT
KO
Strength (µV)
Slope (µV/dB)

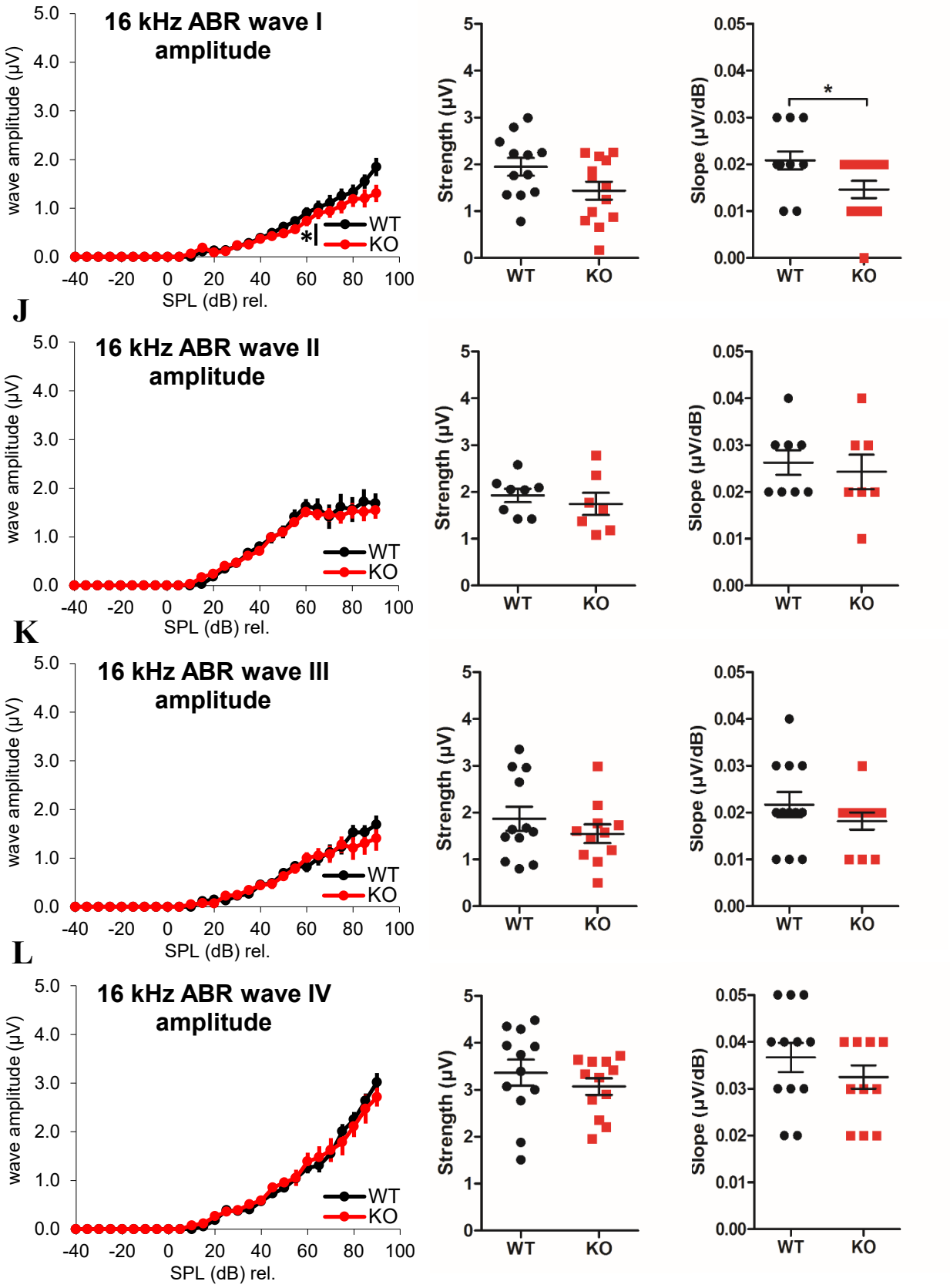
I
16 kHz
16 kHz ABR wave I amplitude
wave amplitude (μV)
SPL (dB) rel.
WT
KO
Strength (μV)
Slope (μV/dB)
J
16 kHz ABR wave II amplitude
K
16 kHz ABR wave III amplitude
L
16 kHz ABR wave IV amplitude

Figure 22: Sound-evoked ABR wave I–IV amplitudes in Task5-KO mice.
(**A-D,** left panel) Click-, (**E-H,** left panel) noise-burst- (**I-L**, left panel) and 16 kHz-evoked ABR wave I-IV amplitude growth functions of WT [n = 6 mice, 12 ears] and Task5-KO [n = 7 mice, 14 ears] mice and the corresponding strength and slope of each growth function (middle & right panel). Data is displayed as mean ± SEM. * $p < 0.05$, ** $p < 0.01$ and *** $p < 0.001$.

In addition to wave amplitudes, wave latencies were determined for all three (click-, noise-burst- and 16 kHz-evoked ABRs) stimuli, which reflect the speed of transmission. We found significant alterations in latency growth functions between genotypes (Fig. 23). For click stimuli, wave II and III latencies were significantly different between WT and Task5-KO mice (Fig. 23B&C left panel; ABR wave II: $p = 0.0115$, $F(1,650) = 6.43$; ABR wave III: $p = < 0.0001$, $F(1,327) = 34.28$; two-way ANOVA). For noise-burst-evoked ABRs, wave II, III and IV latencies were found to be significantly different between genotypes (Fig. 23B-D middle panel; ABR wave II: $p = 0.0159$, $F(1,310) = 5.88$; ABR wave III: $p = < 0.0001$, $F(1,325) = 26.37$; ABR wave IV: $p = < 0.0001$, $F(1,332) = 27.93$; two-way ANOVA). 16 kHz-evoked ABR wave latencies were significantly different for wave I, II and IV (Fig. 23A, B & D right panel; ABR wave I: $p = 0.0042$, $F(1,340) = 8.29$; ABR wave II: $p = < 0.0001$, $F(1,366) = 33.52$; ABR wave IV: $p = 0.0323$, $F(1,341) = 4.62$; two-way ANOVA). Latency differences were determined for all three stimuli revealing mostly shorter latencies for KO mice. The greatest changes in latency were observed for wave II, which reflects the CN, for all three stimuli. Surprisingly, wave I latency differences were limited to 16 kHz-evoked ABRs only, whereas wave I amplitude displayed the most pronounced differences between WT and KO mice (Fig. 22A, E & I). The observed differences between genotypes predominantly showed a decrease in latency growth functions for Task5 deficient mice, with the exception of wave II latency for noise-burst stimuli. The differences were not limited to a certain stimulus level, but rather seemed to have similar effects on low and high stimulus levels.

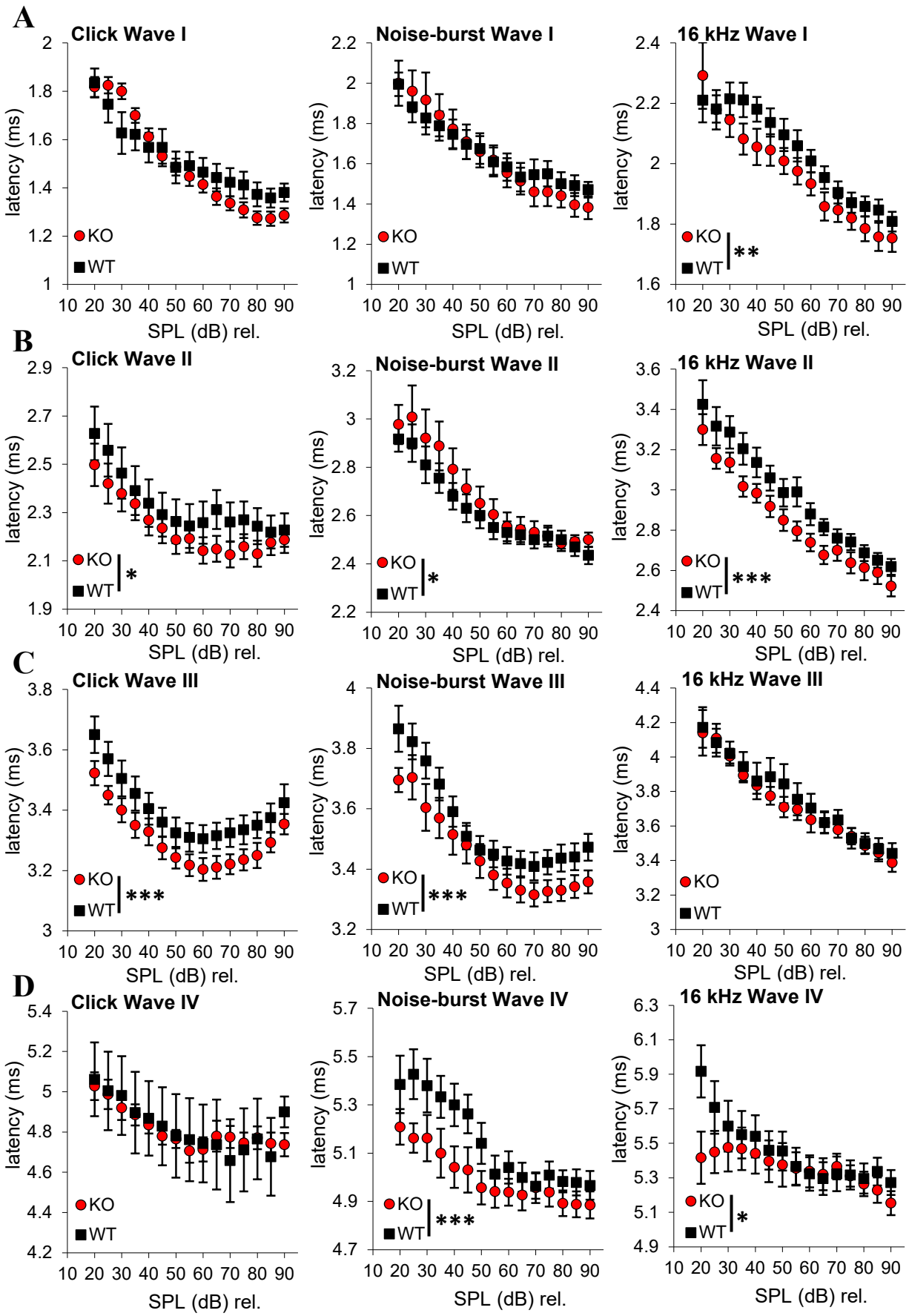
A
Click Wave I
Noise-burst Wave I
16 kHz Wave I
B
Click Wave II
Noise-burst Wave II
16 kHz Wave II
C
Click Wave III
Noise-burst Wave III
16 kHz Wave III
D
Click Wave IV
Noise-burst Wave IV
16 kHz Wave IV
latency (ms)
SPL (dB) rel.
KO
WT
*
**
***

Figure 23: Sound-evoked ABR wave I–IV latencies in Task5-KO mice.
(**A-D,** left panel) Click-, (**A-D,** middle panel) noise-burst- (**A-D**, right panel) and 16 kHz-evoked ABR wave I-IV latencies of WT [n = 6 mice, 12 ears] and Task5-KO [n = 7 mice, 14 ears] mice. Note that latency is increasing along the ascending auditory pathway. Data is displayed as mean ± SEM. * $p < 0.05$, ** $p < 0.01$ and *** $p < 0.001$.

Basic hearing function of Task5-KO and WT control mice was additionally investigated, by determining the hearing thresholds for click-, noise-burst-, 16 kHz- and frequency-specific-evoked ABRs (f-ABR) (Fig. 24). F-ABRs allow to associate the frequency specific allocation of auditory responses with the tonotopical organization of the cochlea. Thresholds of WT and Task5 deficient mice did not differ for click-, noise-burst-, and 16 kHz ABRs (Fig. 24A-C). F-ABR thresholds for the frequency range between 2 and 45.2 kHz revealed subtle deficits of Task5-KO mice at higher frequencies (Fig. 24D; $p = 0.0136$, $F = (1,238) = 6.18$; two-way ANOVA). However, differences were small (with ~9 dB being the greatest difference at 32 kHz) and post-hoc-testing did not reveal a particular stimulus frequency at which thresholds were different ($p > 0.05$, Bonferroni post-hoc-tests).

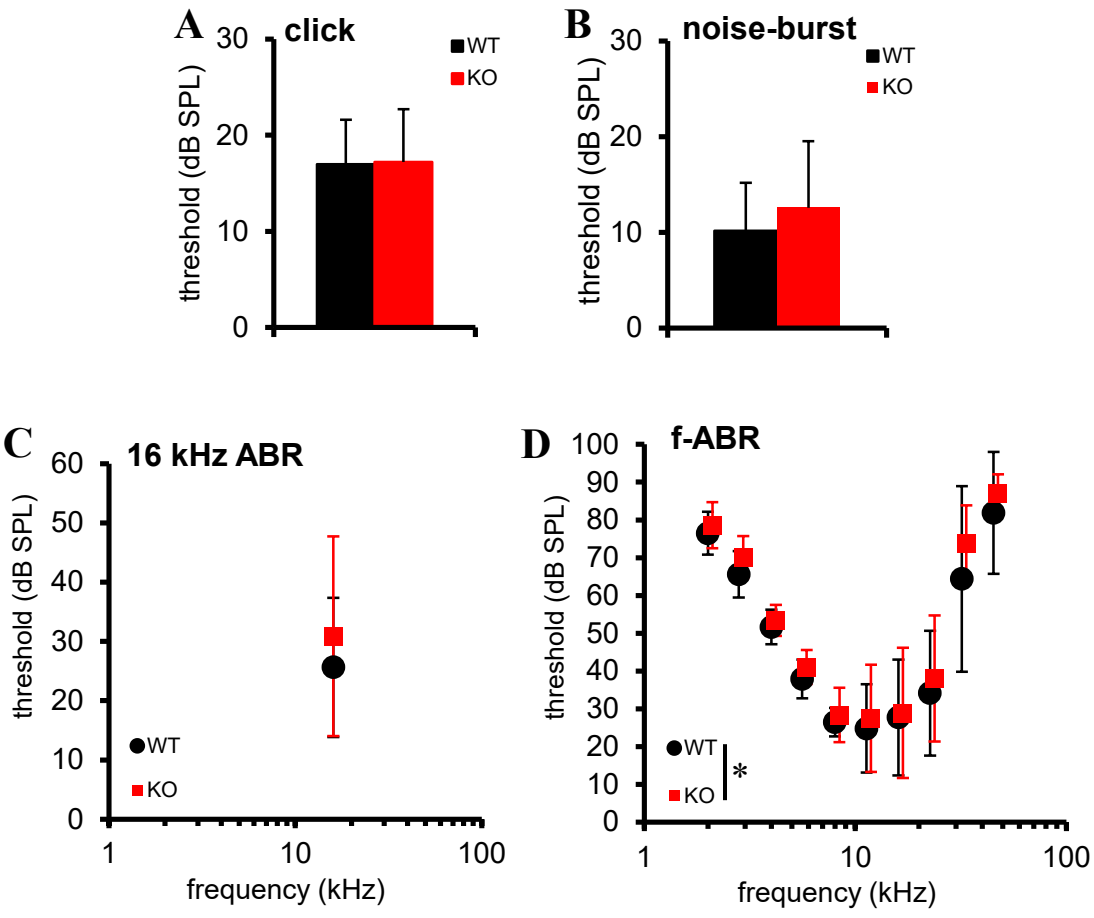

Figure 24: Hearing thresholds measured with ABR.
(**A-C**) ABR thresholds for click, noise-burst and 16 kHz display no significant differences between genotypes (n = WT [6 mice, 12 ears], KO [7 mice, 14 ears]). (**D**) Frequency specific pure tone thresholds were significantly increased in Task5-KO mice and exhibit the greatest difference (~9 dB) at 32 kHz. Data is displayed as mean ± SD. * $p < 0.05$.

3.4.2. DPOAE measurements in Task5 deficient mice

DPOAE measurements were performed as another method for hearing assessment by testing outer hair cell function in WT and Task5-KO mice (Fig. 25). Maximum DPOAE amplitudes were slightly but non-significantly reduced in Task5 deficient mice (Fig. 25A), whereas DPOAE thresholds were found to be significantly elevated in Task5-KO mice (Fig. 25B; $p = 0.0092$, $F(1,24) = 8.03$; two-way ANOVA) and most interestingly, the greatest threshold elevations were found at higher frequencies, namely at 16 kHz and 22.6 kHz (16 kHz: $p < 0.01$; 22.6 kHz: $p < 0.001$, Bonferroni post-hoc-tests). This is further corroborated by the DPOAE I/O function of emission amplitudes evoked by f2 = 22.6 kHz. I/O functions were significantly lower in KO mice (Fig. 25C; $p = 0.0078$, $F(1,23) = 8.50$; two-way repeated measures ANOVA) compared with WT control mice. Post-hoc-testing revealed significant differences at stimulus levels of 45 dB SPL and 50 dB SPL (45 dB SPL: $p < 0.001$; 50 dB SPL: $p < 0.01$, Bonferroni post-hoc-tests). At lower frequencies, 5.66 kHz and 11.3 kHz, I/O functions were hardly affected by Task5 knockout (data not shown). These findings are in agreement with the f-ABR recordings, equally revealing elevated thresholds at higher frequencies for Task5 deficient mice (Fig. 24D). To summarize, DPOAE analysis revealed comparable low frequency DPOAE thresholds between genotypes, but at the same time Task5-KO mice exhibited deficits at higher frequencies, suggesting perturbed outer hair cell function in high-frequency regions of the cochlea.

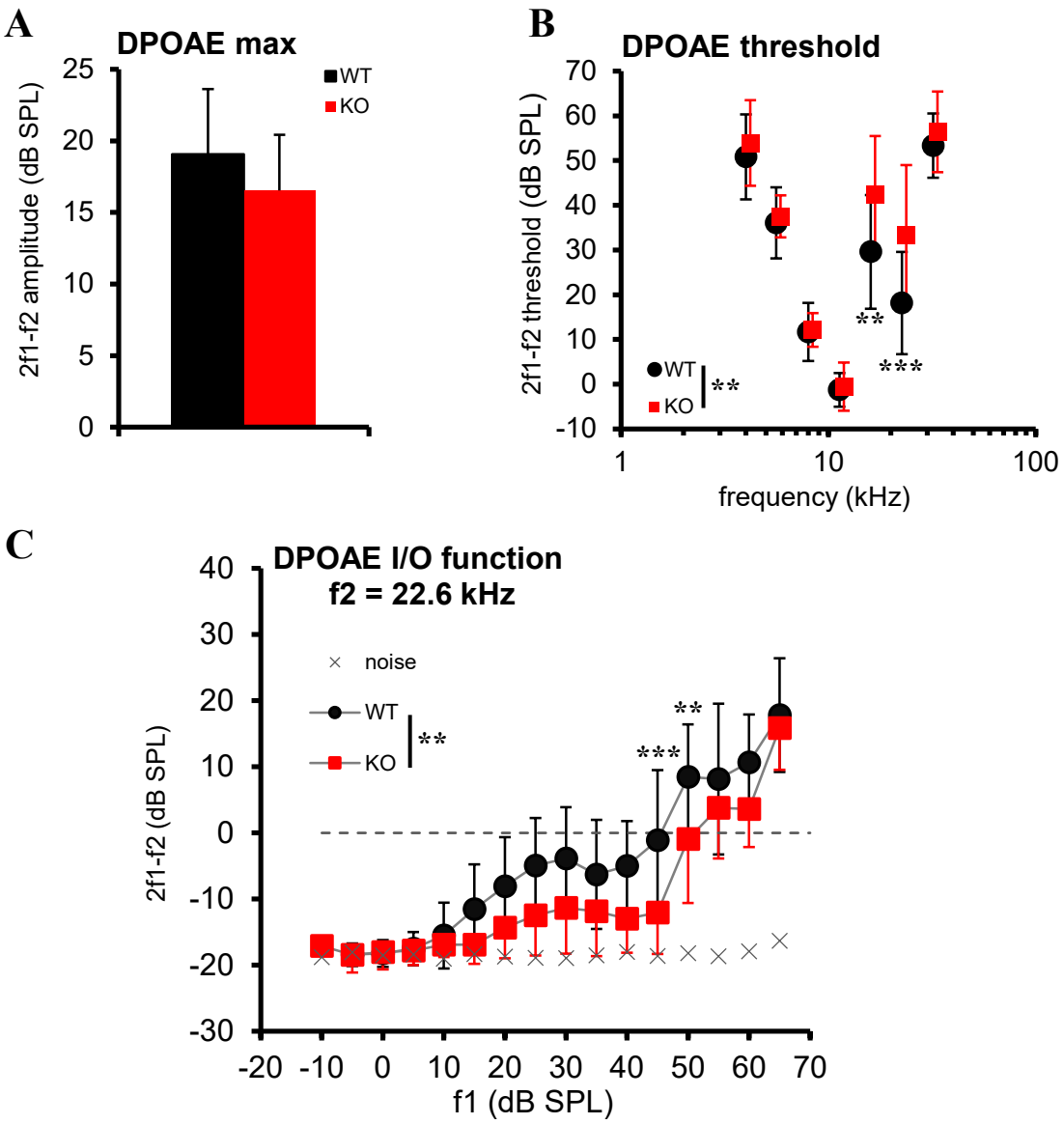

Figure 25: DPOAE measurements.
Outer hair cell function was measured by determining (**A**) DPOAE maximal amplitudes, (**B**) thresholds for the 2f1-f2 distortion product (**C**) and mean cubic DPOAE I/O functions at stimulation frequency (f2) = 22.6 kHz, revealing high frequency deficits for Task5 deficient mice. Data is displayed as mean ± SD. (n = WT [6 mice, 12 ears], KO [7 mice, 14 ears]). ** $p < 0.01$ and *** $p < 0.001$.

3.5. Evoked EPSC kinetics of GBCs

3.5.1. Evoked release upon low frequency (0.1 Hz) stimulation

The obtained results from sound-evoked ABRs, revealing significantly reduced wave I amplitudes in Task5-KO mice (Fig. 22A,E&I) and indicating reduced AN activity, raised interest for the functional integrity of information transfer via the AN. To further assess network changes and a possible involvement of Task5 in vesicular release in the VCN, the properties of AN synapses onto GBCs, known as endbulbs of Held, were examined. Therefore, EPSCs were evoked in endbulbs of Held by placing a bipolar stimulating electrode on the ANR. Evoked EPSCs were recorded from GBCs in the AVCN. Prior to high frequency stimulation, low frequency (0.1 Hz) stimulations were performed to determine if EPSC shape was affected by the absence of Task5. Figure 26A shows representative recordings of evoked EPSCs from WT and KO mice. The acquired results were not affected by Task5 deficiency. Rise- (WT = 483.5 ± 51.34 µs N=13, KO = 579.1 ± 71.52 µs N=17; p = 0.3153; unpaired t-test; Fig. 26B) and decay times (τ decay fast: WT = 0.7400 ± 0.1069 ms N=12; KO = 0.8010 ± 0.1300 ms N=16; p = 0.7329; τ decay slow: WT = 1.253 ± 0.2893 ms N=9; KO = 0.9693 ± 0.1515 ms N=15; p = 0.3479; unpaired t-test; Fig. 26C&D) were unaltered between genotypes. Mean evoked EPSC amplitudes were not significantly greater for KO mice (WT = 2.193 ± 0.3655 nA N=12; KO = 2.926 ± 0.5363 nA N=16; p = 0.3032; unpaired t-test; Fig. 26E).

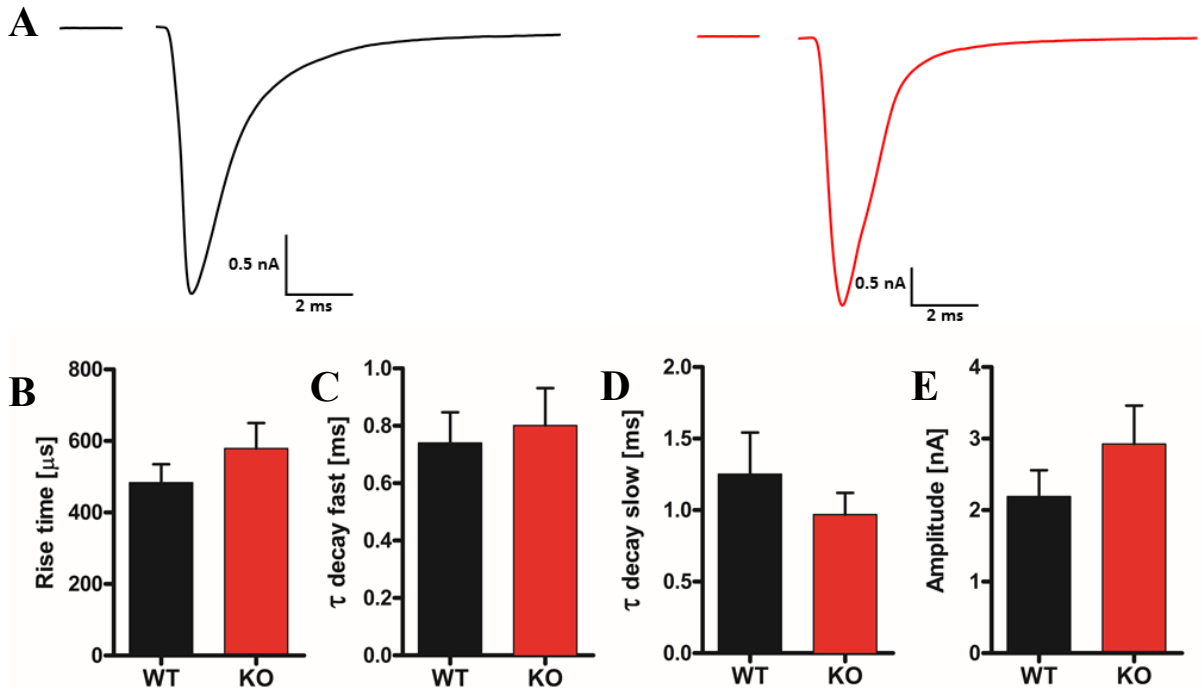

Figure 26: Properties of evoked EPSCs in GBCs.
(**A**) Representative traces of evoked EPSCs for WT (black) and Task5-KO mice (red). The stimulus artifact was removed. Average (**B**) 10–90% evoked EPSC rise time, (**C**) fast decay, (**D**) slow decay and (**E**) amplitude. (n = WT [9-13], KO [15-17]). Data is displayed as mean ± SEM.

3.5.2. STD upon high frequency stimulation

STD of bushy cells *in vitro* is reported in the literature (Wang et al., 2011). To examine STD, the response of GBCs to moderate- (10 Hz) and high frequency (100-300 Hz) ANR stimulation was determined by applying trains of stimuli. Peaks, recorded during trains of stimuli, were normalized to the amplitude of the first EPSC in each train for all stimulation frequencies. Pronounced STD was observed at all frequencies examined. The extent of depression was increased with stimulation frequency, independent of genotype (Table 4). At all tested frequencies, the extent of depression was found to be higher in KO mice compared to WT control mice, with being significantly higher at 200 Hz of stimulation, which is exemplified in representative current traces in figure 27A. The time course of depression was fit with a mono-exponential function and exhibited comparable average time constants of amplitude decay for both genotypes (Fig. 27C and Table 5). Effects of high frequency stimulation on paired pulse ratio (PPR), which was calculated as the second EPSC divided by the first EPSC response, were absent between genotypes (200 Hz: WT = 0.7267 ± 0.1836 N=12, KO = 0.5091 ± 0.09543 N=15; p = 0.2761; unpaired t-test; Fig. 27E) at all measured frequencies (data not shown for 10 Hz, 100 Hz and 300 Hz). In summary, the response to moderate stimuli was similar between Task5-KO and WT control mice. However, when challenged with high frequency stimulation trains, Task5 deficient endbulbs of Held failed to keep up consistent release and revealed greater extent of depression with being significantly enhanced at 200 Hz (Fig. 27D).

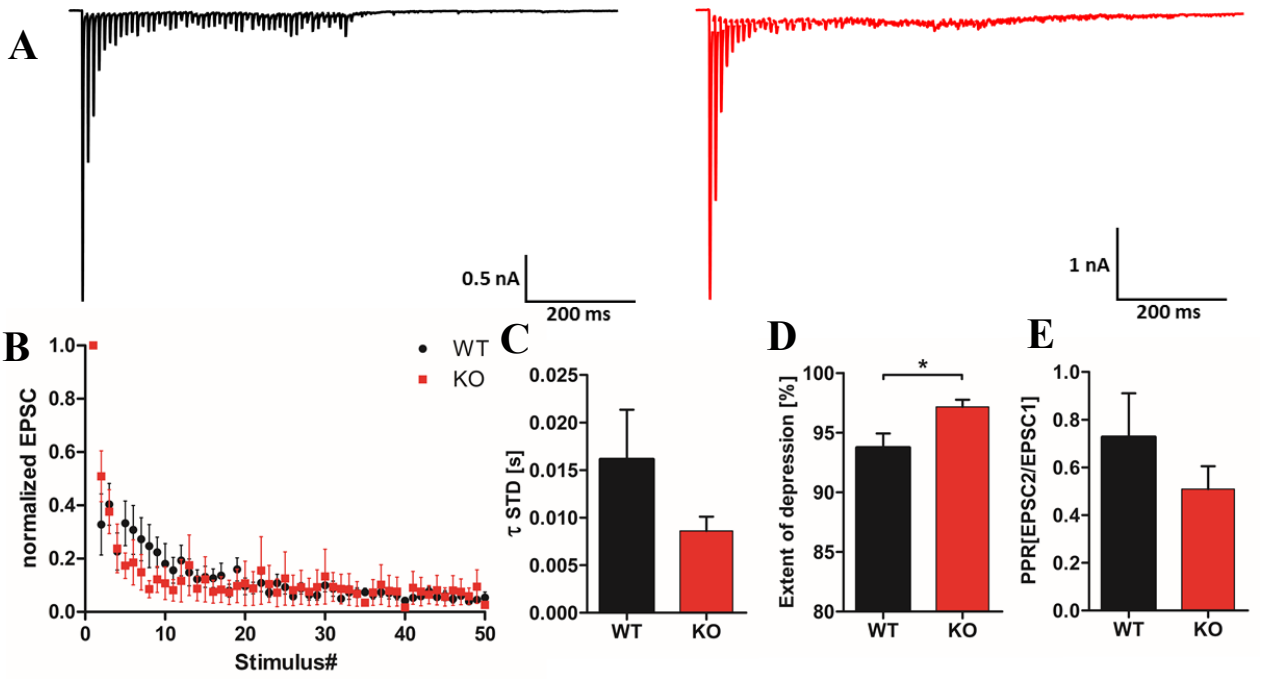

Figure 27: STD upon high-frequency stimulation of 200 Hz.
(**A**) Examples of WT (black) and Task5-KO GBCs (red) EPSCs recorded during a 200 Hz stimulus train. (**B**) Average normalized peak amplitude of evoked EPSCs at 200 Hz stimulation. Quantification of (**C**) time constant of amplitude decay, (**D**) extent of depression and (**E**) PPR when stimulated at 200 Hz. (n = WT [5-12], KO [5-15]). Data is displayed as mean ± SEM. * $p < 0.05$

Table 4: Extent of depression

Stimulation Frequency (Hz)	WT	KO	p-value
10	65.73 ± 2.205% N=7	66.38 ± 2.057% N=14	0.8452
100	90.69 ± 1.286% N=12	94.03 ± 1.103% N=14	0.0590
200	93.73 ± 1.201% N=12	97.15 ± 0.6126% N=14	0.0139
300	88.12 ± 2.596% N=6	91.55 ± 2.174% N=8	0.3282

Table 5: Amplitude decay time constant

Stimulation Frequency (Hz)	WT	KO	p-value
10	0.1923 ± 0.03040 s N=7	0.2077 ± 0.02721 s N=14	0.7316
100	0.04171 ± 0.01161 s N=12	0.02247 ± 0.004160 s N=13	0.1211
200	0.01613 ± 0.005217 s N=12	0.008612 ± 0.001496 s N=13	0.1651
300	0.003885 ± 0.001511 s N=5	0.00366 ± 0.0009070 s N=5	0.9015

During most recordings, in particular at high frequency stimulation (100-300 Hz), we observed that EPSCs did not return to baseline (Fig. 28A), which seemed to be more pronounced in cells lacking Task5. We assume that this firing behavior could indicate asynchronous release. To determine whether this form of neurotransmitter release could take place, the area under the curve (AUC) was measured at 100 Hz to determine the transferred charge. A line was placed above the EPSC train; the shaded areas highlight the shift and represent the measured AUC (Fig. 28A). Despite an obvious tendency of Task5 deficient GBCs towards increased total charge transfer, statistics failed to confirm significance (WT = 123.1 ± 34.39 pc N=11, KO = 274.7 ± 76.87 pc N=12; p = 0.0958; unpaired t-test; Fig. 28B).

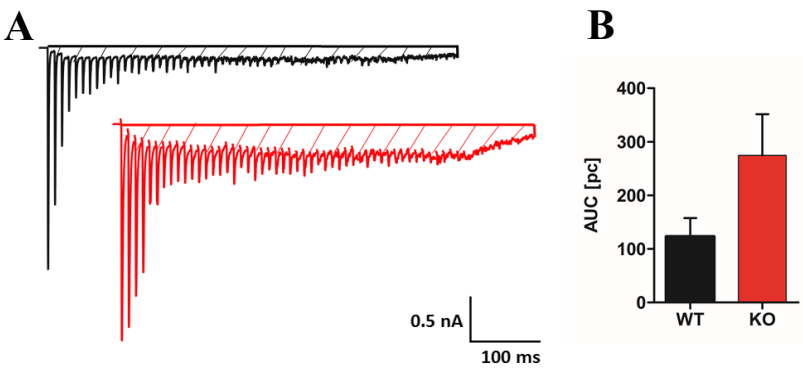

Figure 28: Release pattern at 100 Hz.
(**A**) Representative current traces of a WT (black) and Task5-KO GBC (red) recorded at 100 Hz exhibiting a downward shift of the EPSC train. The shaded areas represent (**B**) the area under the curve, revealing insignificant increase of total charge transfer in Task5 deficient GBCs. (n = WT [11], KO [12]). Data is displayed as mean ± SEM.

The increased extent of depression of Task5 deficient GBCs with increasing stimulation frequency (Table 4 and Fig. 27D) suggests that the readily releasable pool (RRP) and the vesicle replenishment rate could be affected by the absence of Task5. For that purpose, the cumulative EPSC was graphed for the 100 Hz stimulation train (Fig. 29A). Back-extrapolating the linear component allowed the calculation of the RRP size, which is the intersection of the line fit with the Y-axis, whereas the slope of the linear regression fitting represents the replenishment rate (Schneggenburger et al., 1999). Using this method, both RRP size and the replenishment rate were found to be comparable between genotypes (RRP size: WT = 6.657 ± 1.073 nA N=13, KO = 8.843 ± 1.907 N=14; p = 0.3374; Replenishment rate: WT = 0.02613 ± 0.007380 nA/ms N=13, KO = 0.02333 ± 0.007440 nA/ms N=15; p = 0.7930; unpaired t-test; Fig. 29B&C). Equally, calculation of the release probability (average value of the 1st EPSCs from the 100 Hz trains divided by the size of the RRP) reveals that the probability of neurotransmitter release is not

affected by the knockout of Task5 (WT = 0.4278 ± 0.06927 N=13, KO = 0.5570 ± 0.08444 N=15; p = 0.2563; unpaired t-test; Fig. 29D).

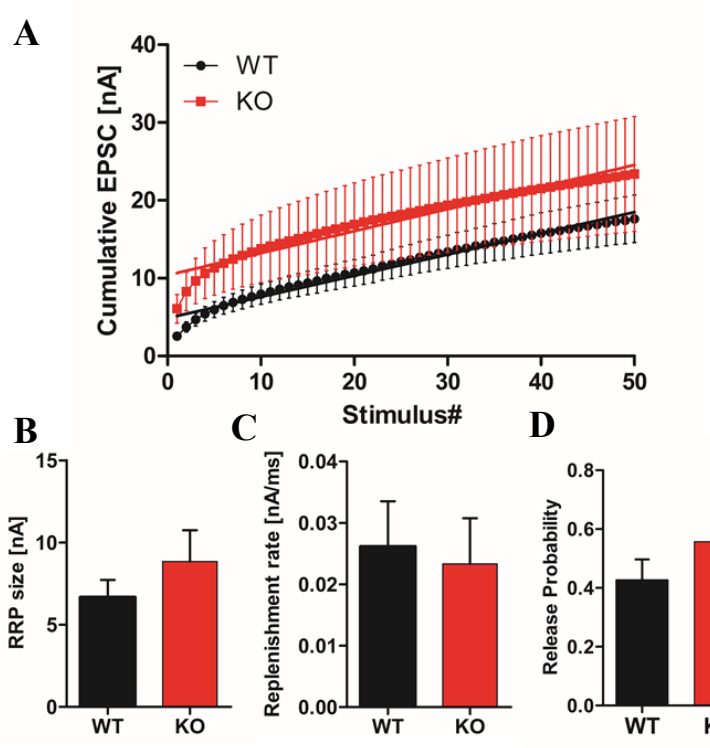

Figure 29: Determining synaptic parameters during 100 Hz stimulation trains.
(**A**) Averaged 100 Hz cumulative EPSC plotted against stimulus number. Quantification of (**B**) the RRP size (intersection with the Y-axis), (**C**) the replenishment rate (slope) and (**D**) the release probability by line fitting through the linear part of the cumulative EPSC exhibited unchanged parameters between genotypes. (n = WT [13], KO [14-15]). Data is displayed as mean ± SEM.

Synaptic recovery after STD is a crucial determinant to ensure proper synaptic transmission. This balance between RRP depletion and rapid replenishment is key to synaptic fidelity. After revealing increased STD in the AVCN, the next important question to answer was, whether synaptic recovery from depression might be as well affected by Task5 knockout. Hence, to explore the role of Task5 in vesicle replenishment, recovery kinetics were analyzed. The time course of synaptic recovery was determined with high-frequency stimulation by depleting the vesicle pool of the synapse with trains of 20 stimuli at 100 Hz and applying test pulses, given at increasing time intervals (0.01 s, 0.064 s, 0.128 s, 0.256 s, 0.512 s, 1.024 s, 2 s, 4 s, 6 s, 8 s, 10 s and 12 s; Fig. 30A). Recovery fraction was measured by normalizing the test EPSC amplitude to the first EPSC in the 100 Hz train. A double-exponential function was used to approximate the time course of recovery (Fig. 30B-D). The double-exponential time course recovered without significant difference between genotypes (τ_{fast}: WT = 0.5529 ± 0.2083 s N=8, KO = 0.5589 ± 0.5349 s N=8; p = 0.9915; τ_{slow}: WT = 3.403 ± 1.246 s N=8, KO = 2.364 ± 1.318 s N=8; p = 0.5758; unpaired t-test). Therefore, these findings suggest that Task5 knockout does not affect the vesicle resupply to active zones in response to high frequency stimulation.

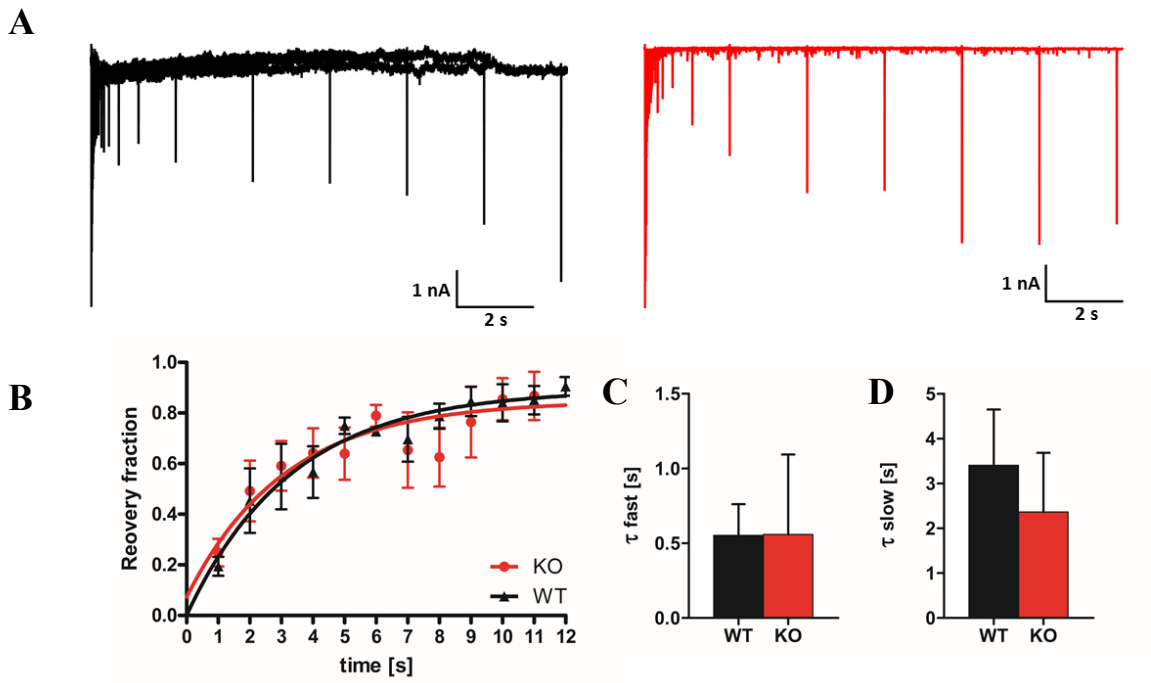

Figure 30: Recovery of readily releasable vesicle pool from synaptic depression.
(**A**) Representative current traces of a WT (black) and Task5-KO (red) mouse showing an initial depleting 100 Hz stimulus train followed by a single test pulse at increasing time intervals ranging from 0.01 s to 12 s. (**B**) Time course of recovery from synaptic depression, fitted by a double-exponential function with a fast (**C**) and a slow time constant (**D**), displaying unaltered recovery parameters between genotypes. (n = WT [8], KO [8]). Data is displayed as mean ± SEM.

4. Discussion

In the presented work, we investigated the physiological role of the K2P channel family member Task5 within the auditory brainstem, the series of nuclei with the reportedly highest Task5 expression (Karschin et al., 2001; Holt et al., 2006; Dong et al., 2009; Ehmann et al., 2013). We approached this question with two different types of genetic perturbations: shRNA-mediated knockdown of Task5 solely within the examined nucleus, and constitutive Task5 knockout resulting in complete brain wide Task5 ablation. This study is the first to report that Task5 shows some of the typical characteristics of K2P channels. To date, the classification of Task5 as a K2P channel is purely based on its 2P/4TM structure and its sequence homology to other members of this potassium channel family (Kim and Gnatenco, 2001; Ashmole et al., 2001; Karschin et al., 2001). Task5 downregulation within the VCN provided us with evidence that Task5 contributes to the phasic firing pattern in VCN neurons by adjusting cell excitability and AP waveform. In accordance with this finding, GBCs show an elevated input-output curve, meaning that GBCs elicited more APs with progressively increasing current stimulus intensity. Moreover, we found a more depolarized RMP and significantly reduced AP thresholds in GBCs. Furthermore, rescue experiments with an shRNA insensitive construct, probably resulting in Task5 overexpression, not only rescued the WT phenotype, but also exhibited a shift in the opposite direction of knockdown results. In general, the Task5 knockdown phenotype was found to be less pronounced in MNTB principal cells, which did not come as a surprise considering the lower Task5 mRNA expression in the MNTB, detected previously (Karschin et al., 2001) and confirmed here via RNAscope *in situ* hybridization.

Rather astonishing was the discrepancy between the two different genetic manipulations. We were not able to reproduce the Task5 knockdown phenotype in KO mice. The remarkable reduction of input resistance, determined from KO-GBCs, strongly indicates genetic compensation upon constitutive Task5 knockout. Nonetheless, ABR and DPOAE measurements revealed consequences of Task5 knockout on auditory function, as the acquired results revealed evidence for a reduction in auditory nerve function and deficits of outer hair cell function in the high frequency range. Finally, challenged with high frequency stimulation trains, Task5-deficient endbulbs of Held depressed to a greater extent and failed to evoke EPSCs as reliably as WTs, further corroborating the notion of perturbed auditory nerve function.

4.1. Task5 mRNA expression in the VCN and MNTB

The lack of an adequate antibody against Task5 protein limits the possibility to assess its tissue expression at the protein level. Due to this limitation, Task5 mRNA expression pattern was examined within the auditory brainstem. Previous research revealed elevated Task5 expression in brain tissue with high and restrictive expression in auditory brainstem nuclei (Karschin et al., 2001 (rat); Holt et al., 2006 (rat); Dong et al., 2009 (guinea-pig); Ehmann et al., 2013 (rat)). Our findings are partially in agreement with previous findings, as we detected Task5 expression in the VCN of WT mice at all timepoints examined. While there is general consensus about high Task5 expression in the VCN (Karschin et al., 2001; Holt et al., 2006; Dong et al., 2009), diverging expression levels are reported for the MNTB (Karschin et al., 2001; Ehmann et al. 2013). Karschin and colleagues detected high Task5 expression levels in the SOC, however, without detecting Task5 positive signal in the MNTB (Karschin et al., 2001). Ehmann et al. reported a developmental upregulation of Task5 in the SOC without determining Task5 expression in specific SOC nuclei (Ehmann et al., 2013). The results obtained within this thesis largely agree with the latter findings. Contrary to Karschin et al., Task5 expression was detected at all three timepoints (P7, P14, ~ P42) in both brainstem nuclei examined (Fig. 5&6), although to a much lower extent in the MNTB compared to the VCN. This suggests regional differences regarding the physiological role of Task5 within auditory brainstem circuits. It is quite possible, that Task5 plays only a minor role in the MNTB or possibly performs a different function. Our findings from current-clamp recordings suggest the former, which is discussed in more detail in chapter 4.3.

Moreover, the visual inspection of Task5 expression levels at the three different stages of hearing, highly suggests a trend towards the developmental upregulation of Task5 for both, the VCN and the MNTB. Task5 positive signal is rather low at pre-hearing stages with a sharp upregulation around the time of hearing onset (P10-P12). High expression levels were maintained into adult hearing. Of note, the increase in Task5 expression during postnatal maturation of the central auditory system coincides with the period of hearing onset. It is thus tempting to speculate that proper Task5 functioning requires sound-driven neuronal activity and/or vice versa. Given the developmental upregulation of Task5 mRNA expression and its reported downregulation after deafening (Holt et al., 2006; Cui et al., 2007; Dong et al., 2009), it can be assumed that Task5 could potentially be involved in the (late)-postnatal maturation of the central auditory system. Interestingly, a recent study investigating expression levels of various K2P channels in the mouse

retina obtained a similar Task5 expression pattern during postnatal development (Hughes et al., 2017). Task5 expression sharply increased at P14 with the difference that expression levels continued to increase into adulthood. Of particular note is the concordant upregulation at P14, which not only represents the timepoint shortly after hearing onset but also shortly after mice open their eyes (Rochefort et al., 2009), underscoring the coincidence of sensory input and functional Task5 activity.

4.2. Subcellular localization of Task5

To date, the subcellular localization of Task5 protein is unknown. This lack of information is largely explained by the non-availability of a reliable, specific antibody. Previous studies, aiming to determine Task5 protein localization, by expressing it in heterologous systems, were not successful (Ashmole et al., 2001; Karschin et al., 2001). However, it is important to determine its subcellular localization, since this will give hints towards the function of the protein.

One major disadvantage of previous studies was their choice to express Task5 in heterologous systems, which do not naturally express Task5. Within this study, we investigated the subcellular localization of Task5 in the rat. By doing so, it is ensured that possible interaction partners, required for Task5's proper localization, are present. Since nothing is known about interaction partners, we fused Task5 with EGFP, either c-terminally or near the second pore domain, as reported for Task3 (Zuzarte et al., 2009). Attempts to produce N-terminally tagged constructs were not successful, so far. Expression of EGFP-tagged Task5 in cultured cortical neurons and in the rat VCN, co-stained with various organelle markers, revealed no colocalization between EGFP-tagged Task5 and Tom20-labeled mitochondria and TGN38-labeled trans-Golgi network. However, a partial co-localization was observed with PDI-labeled ER, in cultured cortical neurons but not in the rat VCN (Fig. 7&8).

Typically, K2P channel trafficking to the cell membrane takes place via the ER, from which, correctly folded proteins are transported to the Golgi complex to be finally targeted to the cell membrane as a mature membrane protein (Mathie et al., 2010). A key step within this pathway is the retention of incomplete protein complexes in the ER, which is often due to insufficient binding of interaction partners at a retention motif, thereby preventing its targeting to the plasma membrane (Mathie et al., 2010). Recently, THIK2, another supposedly non-functional K2P channel, was found to be maintained in the ER due to its N-terminal ER retention motif.

However, Chatelain and colleagues were able to overcome its retention by introducing mutations within this motif that enabled its trafficking to the cell surface, ultimately leading to measurable channel activity (Chatelain et al., 2013). The partial overlap of tagged Task5 with the ER marker in cultured cortical neurons, where it is naturally not expressed, indicates that Task5 is indeed being retained in the ER, at least to a certain extent, most likely due to the presence of an N-terminal ER retention motif. Surprisingly, we did not find overlap between EGFP-tagged Task5 and PDI-labeled ER in rat VCN neurons. This suggests that Task5 successfully interacts with a yet unknown partner(s), which prevent(s) its retention within the ER. Hereby, it may be concluded that the retention motif at the N-terminus does not account for the channel inactivity of Task5.

Since dimerization is essential to form a functional K2P channel, we can only speculate whether improper assembly of the two monomers in the ER of heterologous expression systems and cortical neurons, which is highly agreed on to be the place of monomer coupling, leads to the inability of Task5 to produce measurable currents (Nagaya and Papazian, 1997). However, this does not exclude an indirect participation of Task5 in the regulation of electrical membrane properties in its native environment.

4.3. AP firing properties

4.3.1. Effects of Task5 on AP waveform and firing pattern generation

A major issue to investigate was, whether and how changes in Task5 expression levels will affect cell excitability and consequently AP waveform and firing pattern. These questions were addressed by two different genetic manipulations: either Task5 knockdown or complete deletion of Task5 by constitutive knockout. Task5 knockdown in both, the MNTB and the VCN, resulted in differences in intrinsic electrical properties and AP shape between WT and KD cells (Fig. 9-11), of which the shift towards a more positive RMP and the increase in FWHM were of particular interest. Spike broadening, visible in increased FWHM, is typically a sign of delayed repolarization. The link between K2P channels and their participation in the fast repolarization has already been made by Brickley and colleagues. They showed that knockout of Task3, Task5's closely related family member, resulted in AP broadening in cerebellar granule cells (Brickley et al., 2007). Interestingly, Task3 knockout similarly resulted in an increase of the RMP. In addition, it was recently reported that TREK1 and TRAAK, two other K2P subunits, mediate AP-repolarization in trigeminal nerve afferents (Kanda et al., 2019).

In the VCN, we further found a lower threshold to fire an AP, growing AP numbers with increasing stimulus strength and a shift from the characteristic single-spike onset- to repetitive tonic firing. This indicates the involvement of Task5 in processes that regulate the maintenance of the negative RMP, thereby limiting cell excitability. This is further strengthened by our rescue experiments, which presumably resulted in an overexpression of Task5. Here we observed a shift in the opposite direction of the KD phenotype, most visible in the re-establishment of the predominant phasic firing. Overall, the data point to increased cell excitability when Task5 expression is downregulated in the VCN, suggesting that conventional K2P channel characteristics apply to Task5 as well.

At an early stage of our investigations, it became apparent that the effects of Task5 downregulation in the MNTB are small (Fig. 10&12), when compared to the VCN (Fig. 9&11). This regional difference between the two prominent auditory brainstem nuclei can be explained by the much lower extent of Task5 mRNA detected in the MNTB.

Contrary to our expectations and rather surprisingly, we were not able to reproduce the knockdown phenotype by carrying out the same type of recordings in MNTB and the VCN neurons after constitutive Task5 knockout. Task5-KO cells exhibited no alterations from WT cells in terms of AP waveform and firing pattern (Fig. 14-17). Disagreement between results obtained by different approaches of genetic manipulation are frequently reported in the literature in a wide range of model organisms (e.g. Yang et al., 2013; Chen et al., 2014; Rossi et al., 2015; Jost and Weiner, 2015; Patrinostro et al., 2017). We believe that this discrepancy between the two different types of genetic perturbations can most likely be explained by compensatory mechanisms, although we cannot rule out a difference between rat and mouse. In line with this assumption, we found a substantial decrease in input resistance in Task5-KO GBCs (Fig. 18). This suggests an increase in the number of open channels and provides a first hint to the mechanisms underlying the conflicting results in KD and KO experiments. Viewed together, these findings indicate that complete loss of Task5 triggered a compensatory network to maintain genetic fitness (Chari et al., 2017), which was not observed after Task5 knockdown. Possible molecular mechanisms are discussed in the following chapter.

4.3.2. Potential genetic compensation in response to constitutive Task5 knockout

The divergent outcomes from knockdown and knockout approaches suggest that Task5-KO mice may have undergone genetic compensation. We hypothesized that upregulation of genes coding

for potassium channels with similar distribution pattern might be compensating for the loss of Task5. The steady-state/peak ratio of isolated outward potassium currents measured in GBCs suggests the absence of the transient outward component that is present in the majority of WT GBCs upon depolarization (Fig. 19). This initial transient component is similar to currents associated with the expression of Kv1 subunits (Rudy et al., 2009). In contrast to the two-component current recorded from WT cells, KO GBCs exhibited a single persistent non-inactivating component. This finding favors the assumption that the Kv channel population in the VCN of Task5-KO mice comprises less Kv1 subunits. We rather concluded that the sustained outward-rectifying current recorded from Task5-KO GBCs, may be attributed to the fast-activating and slowly-inactivating Kv3 channels, known to be highly expressed in these cells (Gan and Kaczmarek, 1998; Rothman and Manis, 2003a). Kv1 channels maintain the single AP response (Brew and Forsythe, 1995), whereas Kv3 channels increase the cell's firing rate (Kaczmarek and Zhang, 2017). Along those lines, GBCs from constitutive Task5-KO mice, which have a reduced Kv1 content, switch from balanced phasic-tonic WT firing to a more dominant tonic firing, although this change is not significant. This provides reasonable grounds for the assumption that the Kv channel population has undergone redistribution after Task5-KO and is now predominantly consisting of Kv3 rather than a mixture of Kv1 and Kv3 channels. Literature provides evidence for compensatory adjustment regarding Kv channels, explained by homeostatic intrinsic plasticity. Changes in synaptic input and intrinsic electric activities lead to the redistribution of the prevailing Kv channel population, enabling neurons to adapt rapidly to changing electrical input (Surmeier and Foehring, 2004; Steinert et al., 2011; Kuba et al., 2015).

Most recently and particularly interesting, Poveda and colleagues revealed upregulation of Kv1.1 and Kv3.1b in response to long-term auditory deprivation due to mechanically-induced deafness by cochlear lesions. They proposed that this upregulation may be required to compensate for the state of hyperexcitability, caused by the deafness-induced downregulation of potassium channels that are involved in maintaining the negative RMP (Poveda et al., 2020), which is probably the most prominent feature of K2P channels. As a matter of fact, previous research revealed that Task5 showed the strongest deafness-associated decrease in expression of all investigated K2P channels (Holt et al., 2006; Cui et al., 2007; Dong et al., 2009). Viewed together, this collection of findings highlights the ability of the central auditory system to adapt to new circumstances by upregulating relevant genes to compensate for the loss of others. Interestingly, the upregulation of

the channels mentioned above did not occur after short-time- (1- and 15-days post-lesion) but after long-term deafness (90 days post-lesion), which could serve as an explanation for why Task5 knockdown was not compensated in the same way as constitutive Task5 knockout.

However, there are several difficulties concerning the hypothesis of Kv3 channels, being the main determinant of the persistent single-component current phenotype of Task5-KO GBCs. Arguments against the proposed hypothesis are discussed in chapter 4.5. It should be emphasized that the composition of voltage-activated potassium channels is highly unique between cell types. Furthermore, the multiplicity of possibilities of subunits assembling to form a functional channel, endows different populations of neurons with a variety of kinetic properties due to the diversity of potassium channel isoforms (Jan and Jan, 1990; Coetzee et al., 1999). For this reason, these highly unique current properties can hardly be attributed to single channel families, unless specific blockers were applied to isolate them from one another.

We further considered the possibility of HCN channels being potentially involved in compensating for the loss of Task5. The high presence of HCN channels in the VCN in addition to overlapping electrical properties with K2P channels (Banks et al., 1993; Bal and Oertel, 2000) formed the basis for this assumption. The degree of HCN activation was assessed by determining the sag ratio, which is a characteristic feature of hyperpolarization-activated current (Wilson and Garthwaite, 2010; Cao and Oertel, 2011). Sag ratio, determined from GBCs, was found to be very comparable between genotypes (Fig. 20B), rejecting the previous hypothesis of HCN involvement in compensating for the absence of Task5. The root cause for the inconsistency between the two applied genetic perturbations remains to be further studied.

4.3.3. Technical considerations

One strength of this thesis was to approach the question of the physiological role of Task5 with two different genetic perturbations, regulating native Task5 expression to different degrees. While complete ablation of Task5 by constitutive knockout would have allowed us to gain further insight into the functional relevance of Task5, genetic compensation limited us to exploit the full potential of these investigations. Both genetic perturbations are powerful and state-of-the-art methods. However, both approaches also suffer from limitations. Apart from genetic compensation of the gene of interest in constitutive perturbations, it is not possible to determine the timepoint of functional activity of a certain protein within dynamic processes. KD experiments can partially answer the question of when a protein is functionally active, however,

KD efficiency and potential shRNA off-target effects represent various disadvantages. Particularly, if rather weak effects are expected between genotypes, complete deletion of the gene of interest may be favorable compared to knockdown on RNA level, as the latter results in residual expression of the protein of interest.

4.4. Hearing assessments

4.4.1. Auditory brainstem responses in Task5 deficient mice

The absence of measurable alterations in AP waveform generation and firing pattern does not exclude potential functional consequences of Task5 knockout on hearing performance. ABR measurements within this study provided us with novel possibilities of Task5 involvement in the central auditory system. Task5 has been previously associated with proper auditory function (Holt et al., 2006; Cui et al., 2007; Dong et al., 2009). Despite comparable hearing thresholds between genotypes for all three stimuli applied (Fig. 24A-C), suggesting rather normal and functional hearing in Task5-KO mice, we provide first evidence for a decrease of the summed response of the AN, indicated by the substantial reduction in ABR wave I amplitude growth function (Fig. 22A,E&I). A reduction was obtained for all stimuli applied. Furthermore, our data revealed alterations in the speed of transmission between genotypes (Fig. 23). The strongest alterations between genotypes were detected for wave II, reflecting activity in the CN. Furthermore, wave amplitudes differed at higher stimulus levels between genotypes, whereas latency changes were not limited to a certain stimulus level. Although hearing thresholds were found to be normal, f-ABR thresholds revealed small high-frequency hearing deficits (Fig. 24D). This is rather interesting, considering that normal hearing mice use ultrasonic frequencies (> 20 kHz) to communicate (Portfors and Perkel, 2014). Of note, Cui and colleagues reported Task5 mRNA labeling mainly in low-frequency regions of the inferior colliculus, suggesting that Task5 mRNA is more required in low-frequency regions (Cui et al., 2007). However, no such differences have been reported for other auditory brainstem nuclei and may therefore be special to the inferior colliculus.

Unexpectedly, the majority of latencies were decreased in KO mice, indicating a more rapid transmission. Previous research offers various answers for this conflicting finding. Anatomical alterations between genotypes could be one of the reasons, caused by the generators of ABR components sited closer together, shortening the distance between them and consequently the traveling time along the auditory pathway (Stockard et al., 1978). At the moment, however, we

have no evidence for this. Further causes might lie in the downregulation of inhibitory mechanisms in the central auditory pathway, which is frequently reported for the aging mammalian auditory system (e.g. Simon et al., 2004; Caspary et al., 2008), along with an equally controversial reduction in wave latencies (Boettcher et al., 1993).

4.4.2. DPOAE measurements in Task5 deficient mice

In this study, we report a potential high-frequency outer hair cell dysfunction. This is suggested by elevated DPOAE thresholds and I/O function limited to higher stimulation frequencies. Maximum DPOAE amplitudes were similar, whereas high-frequency DPOAE thresholds and I/O function obtained from Task5-KO mice exhibited major deficits (Fig. 25). This strengthened the acquired f-ABR data, which equally exhibited high-frequency deficits, but to a lesser degree. Outer hair cell function was not altered in low-frequency regions of the cochlea. Outer hair cells act as a cochlear amplifier, enabling hearing sensitivity and frequency discrimination (Fettiplace and Hackney, 2006). Task5 has been previously reported to be expressed in outer hair cells (Scheffer et al., 2015). The results obtained indicate that Task5 may affect processes that enable proper functioning of outer hair cells that are tuned to higher frequencies. We believe that motility deficits, rather than loss of outer hair cells, might contribute to deficits observed in Task5-KO mice at higher frequencies, as the loss of outer hair cells typically raises ABR thresholds (Sergeyenko et al., 2013). Considering the total set of data obtained from hearing assessments, it appears most probable that high-frequency motility deficits of outer hair cells lead to defective cochlear amplification at higher frequencies in Task5-KO mice. Further investigations are required to confirm this hypothesis.

4.5. Synaptic transmission upon constitutive Task5 knockout

AN fibers are capable of sustained firing rates of at least up to 300 Hz (Joris et al., 1994; Taberner and Liberman, 2005). Upon repetitive high-frequency stimulation, the endbulbs display prominent short-term depression due to presynaptic vesicle pool depletion (Wang and Manis, 2008; Wang et al., 2011). Constitutive Task5 knockout enhanced the rate of synaptic depression at the endbulbs of Held during high-frequency stimulus trains (Fig. 27 & Table 4), suggesting impaired transmission of temporal information in the early stages of the auditory system. Increased extent of depression was most pronounced at 200 Hz stimulation at room temperature. Apart from that, WT and Task5-KO mice showed no differences in recovery from synaptic

depression (Fig. 30) and in low-frequency evoked synaptic transmission (Fig. 26) at the endbulb of Held.

We were able to exclude a causal link between altered synaptic parameters such as RRP size or release probability (Fig. 29) and the enhanced synaptic depression after Task5 knockout. This suggests that vesicle docking and fusion at the active zones are normal in Task5-KO endbulbs (Kaeser and Regehr, 2017). However, the determination of these synaptic parameters does not provide information for a potentially enhanced exocytosis via asynchronous release. It has been reported that asynchronous release can increase the level of short-term depression (Salmasi et al., 2019). However, total charge transfer, a measure of the proportion of asynchronous release, was found to be statistically unchanged between phenotypes (Fig. 28). Even though there is no effect from a purely statistical point of view, there is clearly a trend towards enhanced asynchronous release in Task5-KO synapses. Therefore, it seems premature to completely reject a link between increased extent of depression and asynchronous release.

Since evoked synaptic depression altered responses of Task5-KO GBCs only when the ANR was challenged with high-frequency stimulation trains, the question arises whether Task5 might be involved in the adaptation of central auditory brainstem nuclei to high-frequency firing and whether the greater extent of depression of KO cells points towards developmental constraints of the central auditory system in Task5-KO mice. Several findings within this study point to a delayed or halted development of the central auditory nuclei. During postnatal maturation, the central auditory system undergoes marked changes, to meet the requirements, necessary for its remarkable temporal precision and reliability. Auditory neurons acquire their ability to sustain high-frequency activity within the first two postnatal weeks and establish mature-like firing properties immediately before hearing onset (Limb and Ryugo, 2000; Sonntag et al., 2011), at the same time Task5 is prominently upregulated. Such abilities of supporting high-frequency activity are generally associated with Kv3 channels. Earlier in the discussion (4.3.2.), we have proposed that a potential redistribution of Kv channels may contribute to the compensatory mechanisms observed in Task5-KO mice. We hypothesized that Kv3 channels outweigh Kv1 channels in a redistributed potassium channel population in the VCN of KO mice. This hypothesis needs to be reconsidered, as Kv3 channels equip neuronal populations with the ability to follow high-frequency inputs (Kaczmarek and Zhang, 2017). Kv3 channels are not only associated with the generation of high-frequency repetitive firing, but also with supporting efficient neurotransmitter

release, hence limiting short-term depression (Goldberg et al., 2005). Our results, showing enhanced synaptic depression during high-frequency stimulation, conflict with the proposed hypothesis. However, it needs to be considered that Goldberg and colleagues investigated Kv3 channels in cortical interneurons.

Within the central auditory system, it has been shown that lower levels of Kv1 cause neurons to fire multiple APs (Ishikawa et al., 2003). Thus, lower levels of Kv1 could also lead to asynchronous release, which could serve as an explanation for the enhanced STD at the endbulb-GBC synapses of Task5-KO mice during high-frequency stimulation. This would be another indication of the redistribution of Kv1 and Kv3 channels upon Task5 knockout.

It remains elusive, whether and how much Kv1 and Kv3 channels adapt to changes in Task5 expression within auditory brainstem nuclei to guarantee neuronal efficacy. Nevertheless, from the ANR stimulation experiments, we can infer that genetic compensation is neither perfect nor complete. By challenging the endbulbs with ANR high-frequency stimulation, we might have been able to overcome the limits of Task5 compensation.

4.6. Conclusions

The results obtained in this study put us one step closer to unravel the function of the K2P channel family member Task5. This was achieved by the combination of labeling techniques and electrophysiological approaches.

The determination of Task5 mRNA expression in the VCN and MNTB during postnatal development of the central auditory system, led to the discovery of distinct Task5 upregulation shortly after hearing onset (P14) and its maintenance into adult hearing. This allows us to conclude that the physiological role of Task5 becomes functionally relevant around hearing onset. Its continued expression into adult hearing supports the possibility that Task5 is required beyond hearing onset.

Investigations, regarding the subcellular localization of Task5, do not provide support for the assumption that Task5 is retained intracellularly, at least not within the cell organelles examined including the ER. From this, we can conclude that Task5 has the potential to be targeted to the plasma membrane to fulfill its physiological role.

Furthermore, findings presented here show for the first time functional roles of Task5, namely its involvement in the regulation of the RMP, the neuronal excitability and the firing pattern. How Task5 participates in these mechanisms is still speculative at this time and needs further investigations. The discrepancy between KD and KO approaches, namely the failure of reproducing the KD phenotype in constitutive Task5-KO mice, suggests that Task5 knockout triggered mechanisms of genetic compensation. Our preferred assumption that a redistribution of Kv1 and Kv3 channels predominantly compensates for Task5, is both, confirmed and weakened by the results obtained. From these contradicting data, we can conclude that a number of mechanisms contribute to this quite frequently occurring phenomenon.

The results from frequency-specific-evoked ABRs and DPOAE measurements both revealed deficits in auditory processing of Task5-KO mice in the high frequency regime. This, together with deficits in neurotransmitter release at the endbulb of Held, when challenged with high-frequency stimulation trains, points to perturbed AN function. Moreover, these findings could be indicative of a delayed postnatal maturation of auditory brainstem circuits.

When considering the entirety of the data, it becomes evident that Task5's physiological role is required for the regulation of neuronal excitability and the establishment of the typical firing pattern of auditory neurons, most likely at the critical time period of hearing onset.

4.7. Outlook

Further research is needed to determine the precise mechanisms, underlying the effects of Task5 knockout in auditory brainstem nuclei. It is important to identify Task5's intracellular partners that allow it to regulate neuronal excitability even when it is not able to form functional channels by itself in heterologous expressing systems.

Based on findings in this study, conditional gene knockout should be highly considered for future investigations. Conditional gene knockout may help to answer when exactly Task5 function becomes essential as it allows the ablation of the gene of interest at defined timepoints.

Moreover, to determine the physiological role of Task5 and how it performs its function, it is pivotal to establish a well-functioning antibody against Task5. This will be required to examine Task5 more closely within neurons, e.g. its distribution in the axonal outgrowths. Also, accurate co-expression studies could be carried out with other potassium channels and potential interaction partners, for which there are good antibodies commercially available.

Another interesting aspect will be the extension of investigations about the functional relevance of Task5 to the olfactory bulb, as Task5's expression within olfactory sensory neurons is pronounced (Karschin et al., 2001). By doing so, we can further gain knowledge about the physiological role of Task5, beyond the central auditory system.

References

Alloui, A., Zimmermann, K., Mamet, J., Duprat, F., Noël, J., Chemin, J., Guy, N., Blondeau, N., Voilley, N., Rubat-Coudert, C., Borsotto, M., Romey, G., Heurteaux, C., Reeh, P., Eschalier, A., Lazdunski, M., (2006). TREK-1, a K+ channel involved in polymodal pain perception. *The EMBO Journal*, *25*(11), 2368–2376. https://doi.org/10.1038/sj.emboj.7601116

Amin, A. S., & **Wilde**, A. A. M. (2016). Genetic Control of Potassium Channels. *Cardiac Electrophysiology Clinics*, *8*(2): 285–306. https://doi.org/10.1016/j.ccep.2016.01.003

Anthwal, N. & **Thompson**, H. (2015). The development of the mammalian outer and middle ear. *Journal of Anatomy. 228*(2), 217–232. https://doi.org/10.1111/joa.12344

Ashmole, I., Goodwin, P., & Stanfield, P. (2001). TASK-5, a novel member of the tandem pore K + channel family. *Pflügers Archiv European Journal of Physiology*, *442*(6), 828–833. https://doi.org/10.1007/s004240100620

Awatramani, G.B., Turecek, R., and Trussell, L.O. (2004). Inhibitory Control at a Synaptic Relay. *Journal of Neuroscience*, *24*(11), 2643–2647. https://doi.org/10.1523/JNEUROSCI.5144-03.2004

Bal, R., & **Oertel**, D. (2000). Hyperpolarization-Activated, Mixed-Cation Current (I_h) in Octopus Cells of the Mammalian Cochlear Nucleus. *Journal of Neurophysiology*, *84*(2), 806–817. https://doi.org/10.1152/jn.2000.84.2.806

Banks, M., & **Smith**, P. (1992). Intracellular recordings from neurobiotin-labeled cells in brain slices of the rat medial nucleus of the trapezoid body. *The Journal of Neuroscience, 12*(7), 2819–2837. https://doi.org/10.1523/JNEUROSCI.12-07-02819.1992

Banks, M. I., Pearce, R. A., & Smith, P. H. (1993). Hyperpolarization-activated cation current (Ih) in neurons of the medial nucleus of the trapezoid body: Voltage-clamp analysis and enhancement by norepinephrine and cAMP suggest a modulatory mechanism in the auditory brain stem. *Journal of Neurophysiology*, *70*(4), 1420–1432. https://doi.org/10.1152/jn.1993.70.4.1420

Bazwinsky, I., Härtig, W., & Rübsamen, R. (2008). Characterization of cochlear nucleus principal cells of Meriones unguiculatus and Monodelphis domestica by use of calcium-binding protein immunolabeling. *Journal of Chemical Neuroanatomy*, *35*(1), 158–174. https://doi.org/10.1016/j.jchemneu.2007.10.003

Bergsman, J. B., De Camilli, P., & McCormick, D. A. (2004). Multiple Large Inputs to Principal Cells in the Mouse Medial Nucleus of the Trapezoid Body. *Journal of Neurophysiology*, *92*(1), 545–552. https://doi.org/10.1152/jn.00927.2003

Boettcher, F. A., Mills, J. H., Norton, B. L., & Schmiedt, R. A. (1993). Age-related changes in auditory evoked potentials of gerbils. II. Response latencies. *Hearing Research, 71*(1–2), 146–156. https://doi.org/10.1016/0378-5955(93)90030-5

Borst, J. G. G., & **Soria van Hoeve**, J. (2012). The Calyx of Held Synapse: From Model Synapse to Auditory Relay. *Annual Review of Physiology*, *74*(1), 199–224. https://doi.org/10.1146/annurev-physiol-020911-153236

Brew, H., & **Forsythe**, I. (1995). Two voltage-dependent K+ conductances with complementary functions in postsynaptic integration at a central auditory synapse. *The Journal of Neuroscience*, *15*(12), 8011–8022. https://doi.org/10.1523/JNEUROSCI.15-12-08011.1995

Brickley, S. G., Aller, M. I., Sandu, C., Veale, E. L., Alder, F. G., Sambi, H., Mathie, A., & Wisden, W. (2007). TASK-3 Two-Pore Domain Potassium Channels Enable Sustained High-Frequency Firing in

Cerebellar Granule Neurons. *Journal of Neuroscience*, *27*(35), 9329–9340. https://doi.org/10.1523/JNEUROSCI.1427-07.2007

El-Brolosy, M. A., & **Stainier**, D. Y. R. (2017). Genetic compensation: A phenomenon in search of mechanisms. *PLOS Genetics, 13*(7), e1006780. https://doi.org/10.1371/journal.pgen.1006780

Cao, X.-J., & **Oertel**, D. (2011). The magnitudes of hyperpolarization-activated and low-voltage-activated potassium currents co-vary in neurons of the ventral cochlear nucleus. *Journal of Neurophysiology*, *106*(2), 630–640. https://doi.org/10.1152/jn.00015.2010

Caspary, D. M., Ling, L., Turner, J. G., & Hughes, L. F. (2008). Inhibitory neurotransmission, plasticity and aging in the mammalian central auditory system. *Journal of Experimental Biology*, *211*(11), 1781–1791. https://doi.org/10.1242/jeb.013581

Chari, S., Marier, C., Porter, C., Northrop, E., Belinky, A., & Dworkin, I. (2017). Compensatory evolution via cryptic genetic variation: Distinct trajectories to phenotypic and fitness recovery [Preprint]. *Evolutionary Biology*. https://doi.org/10.1101/200725

Chatelain, F. C., Bichet, D., Feliciangeli, S., Larroque, M.-M., Braud, V. M., Douguet, D., & Lesage, F. (2013). Silencing of the Tandem Pore Domain Halothane-inhibited K^+ Channel 2 (THIK2) Relies on Combined Intracellular Retention and Low Intrinsic Activity at the Plasma Membrane. *Journal of Biological Chemistry*, *288*(49), 35081–35092. https://doi.org/10.1074/jbc.M113.503318

Chen, X., Grandont, L., Li, H., Hauschild, R., Paque, S., Abuzeineh, A., Rakusová, H., Benkova, E., Perrot-Rechenmann, C., & Friml, J. (2014). Inhibition of cell expansion by rapid ABP1-mediated auxin effect on microtubules. *Nature*, *516*(7529), 90–93. https://doi.org/10.1038/nature13889

Coetzee, W. A., Amarillo, Y., Chiu, J., Chow, A., Lau, D., McCORMACK, T., Morena, H., Nadal, M. S., Ozaita, A., Pountney, D., Saganich, M., Miera, E. V.-S., & Rudy, B. (1999). Molecular Diversity of K+ Channels. *Annals of the New York Academy of Sciences*, *868*(1 MOLECULAR AND), 233–255. https://doi.org/10.1111/j.1749-6632.1999.tb11293.x

Cui, Y. L., Holt, A. G., Lomax, C. A., & Altschuler, R. A. (2007). Deafness associated changes in two-pore domain potassium channels in the rat inferior colliculus. *Neuroscience*, *149*(2), 421–433. https://doi.org/10.1016/j.neuroscience.2007.05.054

Czirják, G., & **Enyedi**, P. (2001). Formation of Functional Heterodimers between the TASK-1 and TASK-3 Two-pore Domain Potassium Channel Subunits. *Journal of Biological Chemistry, 277*(7), 5426–5432. https://doi.org/10.1074/jbc.m107138200

Djillani, A., Mazella, J., Heurteaux, C., & Borsotto, M. (2019). Role of TREK-1 in Health and Disease, Focus on the Central Nervous System. *Frontiers in Pharmacology*, *10*, 379. https://doi.org/10.3389/fphar.2019.00379

Dong, S., Mulders, W. H. A. M., Rodger, J., & Robertson, D. (2009). Changes in neuronal activity and gene expression in guinea-pig auditory brainstem after unilateral partial hearing loss. *Neuroscience*, *159*(3), 1164–1174. https://doi.org/10.1016/j.neuroscience.2009.01.043

Doyle, D. A. (1998). The Structure of the Potassium Channel: Molecular Basis of K+ Conduction and Selectivity. *Science*, *280*(5360), 69–77. https://doi.org/10.1126/science.280.5360.69

Dresbach, T., Hempelmann, A., Spilker, C., tom Dieck, S., Altrock, W. D., Zuschratter, W., Garner, C. C., & Gundelfinger, E. D. (2003). Functional regions of the presynaptic cytomatrix protein bassoon: Significance for synaptic targeting and cytomatrix anchoring. *Molecular and Cellular Neuroscience*, *23*(2), 279–291. https://doi.org/10.1016/S1044-7431(03)00015-0

Duprat, F. (1997). TASK, a human background K+ channel to sense external pH variations near physiological pH. *The EMBO Journal*, *16*(17), 5464–5471. https://doi.org/10.1093/emboj/16.17.5464

Egger V. & **Feldmeyer** D. Electrical activity of neurons. *Book chapter for Neurosciences, Springer* (Hrsg. C.G.Galizia & P.M.Lledo; 2013)

Ehmann, H., Hartwich, H., Salzig, C., Hartmann, N., Clément-Ziza, M., Ushakov, K., Avraham, K. B., Bininda-Emonds, O. R. P., Hartmann, A. K., Lang, P., Friauf, E., & Nothwang, H. G. (2013). Time-dependent Gene Expression Analysis of the Developing Superior Olivary Complex. *Journal of Biological Chemistry*, *288*(36), 25865–25879. https://doi.org/10.1074/jbc.M113.490508

Enyedi, P., & **Czirják**, G. (2010). Molecular Background of Leak K $^{+}$ Currents: Two-Pore Domain Potassium Channels. *Physiological Reviews*, *90*(2), 559–605. https://doi.org/10.1152/physrev.00029.2009

Enyedi, P., & **Czirják**, G. (2015). Properties, regulation, pharmacology, and functions of the K2P channel, TRESK. *Pflügers Archiv - European Journal of Physiology*, *467*(5), 945–958. https://doi.org/10.1007/s00424-014-1634-8

Feliciangeli, S., Chatelain, F. C., Bichet, D., & Lesage, F. (2015). The family of K 2P channels: Salient structural and functional properties: The family of K 2P channels. *The Journal of Physiology*, *593*(12), 2587–2603. https://doi.org/10.1113/jphysiol.2014.287268

Felix, R. A., Gourévitch, B., & Portfors, C. V. (2018). Subcortical pathways: Towards a better understanding of auditory disorders. *Hearing Research*, *362*, 48–60. https://doi.org/10.1016/j.heares.2018.01.008

Fettiplace, R., & **Hackney**, C. M. (2006). The sensory and motor roles of auditory hair cells. *Nature Reviews Neuroscience*, *7*(1), 19–29. https://doi.org/10.1038/nrn1828

Franzen, D. L., Gleiss, S. A., Berger, C., Kümpfbeck, F. S., Ammer, J. J., & Felmy, F. (2015). Development and modulation of intrinsic membrane properties control the temporal precision of auditory brain stem neurons. *Journal of Neurophysiology*, *113*(2), 524–536. https://doi.org/10.1152/jn.00601.2014

Friauf, E., Fischer, A. U., & Fuhr, M. F. (2015). Synaptic plasticity in the auditory system: A review. *Cell and Tissue Research*, *361*(1), 177–213. https://doi.org/10.1007/s00441-015-2176-x

Gan, L., & **Kaczmarek**, L. K. (1998). When, where, and how much? Expression of the Kv3.1 potassium channel in high-frequency firing neurons. *Journal of Neurobiology, 37*:69–79. https://doi.org/10.1002/(SICI)1097-4695(199810)37:1<69::AID-NEU6>3.0.CO;2-6

Gittelman, J. X., & **Tempel**, B. L. (2006). Kv1.1-Containing Channels Are Critical for Temporal Precision During Spike Initiation. *Journal of Neurophysiology*, *96*(3), 1203–1214. https://doi.org/10.1152/jn.00092.2005

Goldberg, E.M., Watanabe, S., Chang, S.Y., Joho, R.H., Huang, Z.J., Leonard, C.S., and Rudy, B. (2005). Specific functions of Synaptically Localized Potassium Channels in Synaptic Transmission at the Neocortical GABAergic Fast-Spiking Cell Synapse. *Journal of Neuroscience*. 25, 5230–5235. https://doi.org/10.1523/JNEUROSCI.0722-05.2005

Goldstein, S. A. N., Price, L. A., Rosenthal, D. N., & Pausch, M. H. (1996). ORK1, a potassium-selective leak channel with two pore domains cloned from Drosophila melanogaster by expression in Saccharomyces cerevisiae. *Proceedings of the National Academy of Sciences*, *93*(23), 13256–13261. https://doi.org/10.1073/pnas.93.23.13256

Grimm, D., Kay, M. A., & Kleinschmidt, J. A. (2003). Helper virus-free, optically controllable, and two-plasmid-based production of adeno-associated virus vectors of serotypes 1 to 6. *Molecular Therapy*, *7*(6), 839–850. https://doi.org/10.1016/S1525-0016(03)00095-9

Grothe, B., Vater, M., Casseday, J. H., & Covey, E. (1992). Monaural interaction of excitation and inhibition in the medial superior olive of the mustached bat: An adaptation for biosonar. *Proceedings of the National Academy of Sciences*, *89*(11), 5108–5112. https://doi.org/10.1073/pnas.89.11.5108

Grothe, Benedikt, Pecka, M., & McAlpine, D. (2010). Mechanisms of Sound Localization in Mammals. *Physiological Reviews*, *90*(3), 983–1012. https://doi.org/10.1152/physrev.00026.2009

Guéguinou, M., Chantôme, A., Fromont, G., Bougnoux, P., Vandier, C., & Potier-Cartereau, M. (2014). KCa and Ca2+ channels: The complex thought. *Biochimica et Biophysica Acta (BBA) - Molecular Cell Research*, *1843*(10), 2322–2333. https://doi.org/10.1016/j.bbamcr.2014.02.019

Gutman, G. A., Chandy, K. G., Grissmer, S., Lazdunski, M., Mckinnon, D., Pardo, L. A., Robertson, G. A., Rudy, B., Sanguinetti, M. C., Stühmer, W., & Wang, X. (2005). International Union of Pharmacology. LIII. Nomenclature and Molecular Relationships of Voltage-Gated Potassium Channels. *Pharmacological Reviews*, *57*(4), 473–508. https://doi.org/10.1124/pr.57.4.10

Hamann, M., Billups, B., & Forsythe, I. D. (2003). Non-calyceal excitatory inputs mediate low fidelity synaptic transmission in rat auditory brainstem slices. *European Journal of Neuroscience*, *18*(10), 2899–2902. https://doi.org/10.1111/j.1460-9568.2003.03017.x

Harrison, J. M., & **Irving**, R. (1965). The anterior ventral cochlear nucleus. *The Journal of Comparative Neurology*, *124*(1), 15–41. https://doi.org/10.1002/cne.901240103

Harrison, J. M., & **Warr**, W. B. (1962). A study of the cochlear nuclei and ascending auditory pathways of the medulla. *The Journal of Comparative Neurology*, *119*(3), 341–379. https://doi.org/10.1002/cne.901190306

Heurteaux, C., Guy, N., Laigle, C., Blondeau, N., Duprat, F., Mazzuca, M., Lang-Lazdunski, L., Widmann, C., Zanzouri, M., Romey, G., Lazdunski, M., (2004). TREK-1, a K+ channel involved in neuroprotection and general anesthesia. *The EMBO Journal, 23*(13), 2684–2695. https://doi.org/10.1038/sj.emboj.7600234

Heurteaux, C., Lucas, G., Guy, N., El Yacoubi, M., Thümmler, S., Peng, X.-D., Noble, F., Blondeau, N., Widmann, C., Borsotto, M., Gobbi, G., Vaugeois, J.-M., Debonnel, G., & Lazdunski, M. (2006). Deletion of the background potassium channel TREK-1 results in a depression-resistant phenotype. *Nature Neuroscience*, *9*(9), 1134–1141. https://doi.org/10.1038/nn1749

Hoffpauir, B. K., Grimes, J. L., Mathers, P. H., Spirou, G.A. (2006). Synaptogenesis of the calyx of Held: rapid onset of function and one-to-one morphological innervation. *The Journal of Neuroscience*, *26*(20): 5511–5523. https://doi.org/10.1523/jneurosci.5525-05.2006

Hoffpauir, B. K., Kolson, D. R., Mathers, P. H., & Spirou, G. A. (2010). Maturation of synaptic partners: Functional phenotype and synaptic organization tuned in synchrony: Coordinated maturation of synaptic partners. *The Journal of Physiology*, *588*(22), 4365–4385. https://doi.org/10.1113/jphysiol.2010.198564

Holt, A. G., Asako, M., Keith Duncan, R., Lomax, C. A., Juiz, J. M., & Altschuler, R. A. (2006). Deafness associated changes in expression of two-pore domain potassium channels in the rat cochlear nucleus. *Hearing Research*, *216–217*, 146–153. https://doi.org/10.1016/j.heares.2006.03.009

Honoré, E. (2007). The neuronal background K2P channels: Focus on TREK1. *Nature Reviews Neuroscience*, *8*(4), 251–261. https://doi.org/10.1038/nrn2117

Hughes, S., Foster, R. G., Peirson, S. N., & Hankins, M. W. (2017). Expression and localisation of two-pore domain (K2P) background leak potassium ion channels in the mouse retina. *Scientific Reports*, *7*(1), 46085. https://doi.org/10.1038/srep46085

Huguet, G., Meng, X., & **Rinzel**, J. (2017). Phasic Firing and Coincidence Detection by Subthreshold Negative Feedback: Divisive or Subtractive or, Better, Both. *Frontiers in Computational Neuroscience*, *11*. https://doi.org/10.3389/fncom.2017.00003

Ishikawa, T., Nakamura, Y., Saitoh, N., Li, W.-B., Iwasaki, S., & Takahashi, T. (2003). Distinct Roles of Kv1 and Kv3 Potassium Channels at the Calyx of Held Presynaptic Terminal. *The Journal of Neuroscience, 23*(32), 10445–10453. https://doi.org/10.1523/JNEUROSCI.23-32-10445.2003

Jan, L. Y., & **Jan**, Y. N. (1990). How might the diversity of potassium channels be generated? *Trends in Neurosciences*, *13*(10), 415–419. https://doi.org/10.1016/0166-2236(90)90123-R

Jentsch, T. J. (2000.). Neuronal KCNQ potassium channels: physiology and role in disease. *Nature Reviews Neuroscience,1*(1):21–30. https://doi.org/10.1038/35036198

Johnston, J., Forsythe, I. D., & Kopp-Scheinpflug, C. (2010). SYMPOSIUM REVIEW: Going native: voltage-gated potassium channels controlling neuronal excitability: K^+ channels and auditory processing. *The Journal of Physiology*, *588*(17), 3187–3200. https://doi.org/10.1113/jphysiol.2010.191973

Joris, P. X., Carney, L. H., Smith, P. H., & Yin, T. C. (1994). Enhancement of neural synchronization in the anteroventral cochlear nucleus. I. Responses to tones at the characteristic frequency. *Journal of Neurophysiology*, *71*(3), 1022–1036. https://doi.org/10.1152/jn.1994.71.3.1022

Jost, A. P.-T., & **Weiner**, O. D. (2015). Probing Yeast Polarity with Acute, Reversible, Optogenetic Inhibition of Protein Function. *ACS Synthetic Biology*, *4*(10), 1077–1085. https://doi.org/10.1021/acssynbio.5b00053

Kaczmarek, L. K., & **Zhang**, Y. (2017). Kv3 Channels: Enablers of Rapid Firing, Neurotransmitter Release, and Neuronal Endurance. *Physiological Reviews*, *97*(4), 1431–1468. https://doi.org/10.1152/physrev.00002.2017

Kaeser, P. S., & **Regehr**, W. G. (2017). The readily releasable pool of synaptic vesicles. *Current Opinion in Neurobiology*, *43*, 63–70. https://doi.org/10.1016/j.conb.2016.12.012

Kanda, H., Ling, J., Tonomura, S., Noguchi, K., Matalon, S., & Gu, J. G. (2019). TREK-1 and TRAAK Are Principal K+ Channels at the Nodes of Ranvier for Rapid Action Potential Conduction on Mammalian Myelinated Afferent Nerves. *Neuron*, *104*(5), 960-971.e7. https://doi.org/10.1016/j.neuron.2019.08.042

Kandler, K., & **Friauf**, E. (1995). Development of Electrical Membrane Properties and Discharge Characteristics of Superior Olivary Complex Neurons in Fetal and Postnatal Rats. *European Journal of Neuroscience*, *7*(8), 1773–1790. https://doi.org/10.1111/j.1460-9568.1995.tb00697.x

Karschin, C., Wischmeyer, E., Preisig-Müller, R., Rajan, S., Derst, C., Grzeschik, K.-H., Daut, J., & Karschin, A. (2001). Expression Pattern in Brain of TASK-1, TASK-3, and a Tandem Pore Domain K+ Channel Subunit, TASK-5, Associated with the Central Auditory Nervous System. *Molecular and Cellular Neuroscience*, *18*(6), 632–648. https://doi.org/10.1006/mcne.2001.1045

Ketchum, K. A., Joiner, W. J., Sellers, A. J., Kaczmarek, L. K., & Goldstein, S. A. N. (1995). A new family of outwardly rectifying potassium channel proteins with two pore domains in tandem. *Nature*, *376*(6542), 690–695. https://doi.org/10.1038/376690a0

Kim, D., & **Gnatenco**, C. (2001). TASK-5, a New Member of the Tandem-Pore K+ Channel Family. *Biochemical and Biophysical Research Communications*, *284*(4), 923–930. https://doi.org/10.1006/bbrc.2001.5064

Kim, Y., Bang, H., & Kim, D. (2000). TASK-3, a New Member of the Tandem Pore K(+) Channel Family. *Journal of Biological Chemistry. 275*(13), 9340–9347. https://www.jbc.org/content/275/13/9340

Klugmann, M., Wymond Symes, C., Leichtlein, C. B., Klaussner, B. K., Dunning, J., Fong, D., Young, D., & During, M. J. (2005). AAV-mediated hippocampal expression of short and long Homer 1 proteins differentially affect cognition and seizure activity in adult rats. *Molecular and Cellular Neuroscience*, *28*(2), 347–360. https://doi.org/10.1016/j.mcn.2004.10.002

Koay, G., Heffner, R. S., & Heffner, H. E. (2002). Behavioral audiograms of homozygous medJ mutant mice with sodium channel deficiency and unaffected controls. *Hearing Research, 171*(1–2): 111–118. https://doi.org/10.1016/s0378-5955(02)00492-6

Koch, U., Braun, M., Kapfer, C., & Grothe, B. (2004). Distribution of HCN1 and HCN2 in rat auditory brainstem nuclei. *European Journal of Neuroscience*, *20*(1), 79–91. https://doi.org/10.1111/j.0953-816X.2004.03456.x

Körber, C., Dondzillo, A., Eisenhardt, G., Herrmannsdörfer, F., Wafzig, O., & Kuner, T. (2014). Gene expression profile during functional maturation of a central mammalian synapse. *European Journal of Neuroscience*, *40*(6), 2867–2877. https://doi.org/10.1111/ejn.12661

Kopp-Scheinpflug, C., Lippe, W. R., Dörrscheidt, G. J., & Rübsamen, R. (2003). The Medial Nucleus of the Trapezoid Body in the Gerbil Is More Than a Relay: Comparison of Pre- and Postsynaptic Activity. *JARO - Journal of the Association for Research in Otolaryngology*, *4*(1), 1–23. https://doi.org/10.1007/s10162-002-2010-5

Kuang, Q., Purhonen, P., & Hebert, H. (2015). Structure of potassium channels. *Cellular and Molecular Life Sciences*, *72*(19), 3677–3693. https://doi.org/10.1007/s00018-015-1948-5

Kuba, H., Yamada, R., Ishiguro, G., & Adachi, R. (2015). Redistribution of Kv1 and Kv7 enhances neuronal excitability during structural axon initial segment plasticity. *Nature Communications*, *6*(1), 8815. https://doi.org/10.1038/ncomms9815

Kulesza, R. J., & **Grothe**, B. (2015). Yes, there is a medial nucleus of the trapezoid body in humans. *Frontiers in Neuroanatomy*, *9*. https://doi.org/10.3389/fnana.2015.00035

Lesage, F., Guillemare, E., Fink, M., Duprat, F., Lazdunski, M., Romey, G., & Barhanin, J. (1996a). A pH-sensitive Yeast Outward Rectifier K Channel with Two Pore Domains and Novel Gating Properties. *Journal of Biological Chemistry*, *271*(8), 4183–4187. https://doi.org/10.1074/jbc.271.8.4183

Lesage, F., Guillemare, E., Fink, M., Duprat, F., Lazdunski, M., Romey, G., & Barhanin, J. (1996b). TWIK-1, a ubiquitous human weakly inward rectifying K+ channel with a novel structure. *The EMBO Journal*, *15*(5), 1004–1011. https://doi.org/10.1002/j.1460-2075.1996.tb00437.x

Lesage, F., Reyes, R., Fink, M., Duprat, F., Guillemare, E., & Lazdunski, M. (1996c). Dimerization of TWIK-1 K+ channel subunits via a disulfide bridge. *The EMBO Journal*, *15*(23), 6400–6407. https://doi.org/10.1002/j.1460-2075.1996.tb01031.x

Lesage, Florian, & **Lazdunski**, M. (2000). Molecular and functional properties of two-pore-domain potassium channels. *American Journal of Physiology-Renal Physiology*, *279*(5), F793–F801. https://doi.org/10.1152/ajprenal.2000.279.5.F793

Limb, C. J., & **Ryugo**, D. K. (2000). Development of Primary Axosomatic Endings in the Anteroventral Cochlear Nucleus of Mice. *Journal of the Association for Research in Otolaryngology*, *1*(2), 103–119. https://doi.org/10.1007/s101620010032

Lotshaw, D. P. (2007). Biophysical, pharmacological, and functional characteristics of cloned and native mammalian two-pore domain K+ channels. *Cell Biochemistry and Biophysics*, *47*(2), 209–256. https://doi.org/10.1007/s12013-007-0007-8

MacKenzie, G., Franks, N. P., & Brickley, S. G. (2015). Two-pore domain potassium channels enable action potential generation in the absence of voltage-gated potassium channels. *Pflügers Archiv - European Journal of Physiology*, *467*(5), 989–999. https://doi.org/10.1007/s00424-014-1660-6

Madry, C., Kyrargyri, V., Arancibia-Cárcamo, I. L., Jolivet, R., Kohsaka, S., Bryan, R. M., & Attwell, D. (2018). Microglial Ramification, Surveillance, and Interleukin-1β Release Are Regulated by the Two-Pore Domain K+ Channel THIK-1. *Neuron*, *97*(2), 299-312.e6. https://doi.org/10.1016/j.neuron.2017.12.002

Manis, P., & **Marx**, S. (1991). Outward currents in isolated ventral cochlear nucleus neurons. *The Journal of Neuroscience*, *11*(9), 2865–2880. https://doi.org/10.1523/JNEUROSCI.11-09-02865.1991

Mathie, A., A. Rees, K., F. El Hachmane, M., & L. Veale, E. (2010). Trafficking of Neuronal Two Pore Domain Potassium Channels. *Current Neuropharmacology*, *8*(3), 276–286. https://doi.org/10.2174/157015910792246146

Melcher, J. R., & **Kiang**, N. Y. S. (1996). Generators of the brainstem auditory evoked potential in cat III: Identified cell populations. *Hearing Research, 93*(1–2), 52–71. https://doi.org/10.1016/0378-5955(95)00200-6

Müller, M.K., Jovanovic, S., Keine, C., Radulovic, T., Rübsamen, R., Milenkovic, I., (2019). Functional Development of Principal Neurons in the Anteroventral Cochlear Nucleus Extends Beyond Hearing Onset. *Frontiers in Cellular Neuroscience, 13*. https://doi.org/10.3389/fncel.2019.00119

Nagaya, N., & **Papazian**, D. M. (1997). Potassium channel α and β subunits assemble in the endoplasmic reticulum. *Journal of Biological Chemistry. 272*(5)*,* 3022–3027. https://doi.org/10.1074/jbc.272.5.3022

Nakamura, P. A., & **Cramer**, K. S. (2011). Formation and maturation of the calyx of Held. *Hearing Research*, *276*(1–2), 70–78. https://doi.org/10.1016/j.heares.2010.11.004

Nicol, M. J., & **Walmsley**, B. (2002). Ultrastructural basis of synaptic transmission between endbulbs of Held and bushy cells in the rat cochlear nucleus. *The Journal of Physiology*, *539*(3), 713–723. https://doi.org/10.1113/jphysiol.2001.012972

Nothwang, H. G., Ebbers, L., Schlüter, T., & Willaredt, M. A. (2015). The emerging framework of mammalian auditory hindbrain development. *Cell and Tissue Research, 361*(1), 33–48. https://doi.org/10.1007/s00441-014-2110-7

O'Connell, A. D., Morton, M. J., & Hunter, M. (2002). Two-pore domain K+ channels—Molecular sensors. *Biochimica et Biophysica Acta (BBA) - Biomembranes*, *1566*(1–2), 152–161. https://doi.org/10.1016/S0005-2736(02)00597-7

Oertel, D. (1991). The role of intrinsic neuronal properties in the encoding of auditory information in the cochlear nuclei. *Current Opinion in Neurobiology*, *1*(2), 221–228. https://doi.org/10.1016/0959-4388(91)90082-I

Oertel, D. (1999). The role of timing in the brain stem auditory nuclei of vertebrates. *Annual Review of Physiology*, *61*(1), 497–519. https://doi.org/10.1146/annurev.physiol.61.1.497

O'Neil, J. N., Connelly, C. J., Limb, C. J., & Ryugo, D. K. (2011). Synaptic morphology and the influence of auditory experience. *Hearing Research*, *279*(1–2), 118–130. https://doi.org/10.1016/j.heares.2011.01.019

Osen, K. K. (1969). Cytoarchitecture of the cochlear nuclei in the cat. *The Journal of Comparative Neurology*, *136*(4), 453–483. https://doi.org/10.1002/cne.901360407

Patel, A. J., & **Honoré**, E. (2001). Properties and modulation of mammalian 2P domain K+ channels. *Trends in Neurosciences*, *24*(6), 339–346. https://doi.org/10.1016/S0166-2236(00)01810-5

Patel, A. J., Honoré, E., Lesage, F., Fink, M., Romey, G., & Lazdunski, M. (1999). Inhalational anesthetics activate two-pore-domain background K+ channels. *Nature Neuroscience*, *2*(5), 422–426. https://doi.org/10.1038/8084

Patel, A. J., Maingret, F., Magnone, V., Fosset, M., Lazdunski, M., & Honoré, E. (2000). TWIK-2, an Inactivating 2P Domain K^+ Channel. *Journal of Biological Chemistry*, *275*(37), 28722–28730. https://doi.org/10.1074/jbc.M003755200

Patrinostro, X., O'Rourke, A. R., Chamberlain, C. M., Moriarity, B. S., Perrin, B. J., & Ervasti, J. M. (2017). Relative importance of β_{cyto}—And γ_{cyto} -actin in primary mouse embryonic fibroblasts. *Molecular Biology of the Cell*, *28*(6), 771–782. https://doi.org/10.1091/mbc.e16-07-0503

Portfors, C. V., & **Perkel**, D. J. (2014). The role of ultrasonic vocalizations in mouse communication. *Current Opinion in Neurobiology*, *28*, 115–120. https://doi.org/10.1016/j.conb.2014.07.002

Poveda, C. M., Valero, M. L., Pernia, M., Alvara, J. C., Ryugo, D. K., Merchan, M. A., & Juiz, J. M. (2020). Expression and Localization of Kv1.1 and Kv3.1b Potassium Channels in the Cochlear Nucleus and Inferior Colliculus after Long-Term Auditory Deafferentation. *Brain Sciences*, *10*(1), 35. https://doi.org/10.3390/brainsci10010035

Rajan, S., Wischmeyer, E., Xin Liu, G., Preisig-Müller, R., Daut, J., Karschin, A., & Derst, C. (2000). TASK-3, a novel tandem pore domain acid-sensitive K+ channel. An extracellular histiding as pH sensor. *Journal of Biological Chemistry*, *275*(22), 16650–16657. https://doi.org/10.1074/jbc.M000030200

Rajan, S., Preisig-Müller, R., Wischmeyer, E., Nehring, R., Hanley, P. J., Renigunta, V., Musset, B., Schlichthörl, G., Derst, C., Karschin, A., & Daut, J. (2002). Interaction with 14-3-3 proteins promotes functional expression of the potassium channels TASK-1 and TASK-3. *The Journal of Physiology, 545*(1), 13–26. https://doi.org/10.1113/jphysiol.2002.027052

Rhode, W. S., Oertel, D., & Smith, P. H. (1983). Physiological response properties of cells labeled intracellularly with horseradish peroxidase in cat ventral cochlear nucleus. *The Journal of Comparative Neurology*, *213*(4), 448–463. https://doi.org/10.1002/cne.902130408

Richter, E. A., Norris, B. E., Fullerton, B. C., Levine, R. A., & Kiang, N. Y. S. (1983). Is there a medial nucleus of the trapezoid body in humans? *American Journal of Anatomy*, *168*(2), 157–166. https://doi.org/10.1002/aja.1001680205

Roberts, M. T., Seeman, S. C., & Golding, N. L. (2014). The relative contributions of MNTB and LNTB neurons to inhibition in the medial superior olive assessed through single and paired recordings. *Frontiers in Neural Circuits*, *8*. https://doi.org/10.3389/fncir.2014.00049

Rochefort, N. L., Garaschuk, O., Milos, R.-I., Narushima, M., Marandi, N., Pichler, B., Kovalchuk, Y., & Konnerth, A. (2009). Sparsification of neuronal activity in the visual cortex at eye-opening. *Proceedings of the National Academy of Sciences*, *106*(35), 15049–15054. https://doi.org/10.1073/pnas.0907660106

Rossi, A., Kontarakis, Z., Gerri, C., Nolte, H., Hölper, S., Krüger, M., & Stainier, D. Y. R. (2015). Genetic compensation induced by deleterious mutations but not gene knockdowns. *Nature*, *524*(7564), 230–233. https://doi.org/10.1038/nature14580

Rothman, J. S., Young, E. D., & Manis, P. B. (1993). Convergence of auditory nerve fibers onto bushy cells in the ventral cochlear nucleus: Implications of a computational model. *Journal of Neurophysiology*, *70*(6), 2562–2583. https://doi.org/10.1152/jn.1993.70.6.2562

Rothman, Jason S., & **Manis**, P. B. (2003a). Differential Expression of Three Distinct Potassium Currents in the Ventral Cochlear Nucleus. *Journal of Neurophysiology*, *89*(6), 3070–3082. https://doi.org/10.1152/jn.00125.2002

Rothman, Jason S., & **Manis**, P. B. (2003b). Kinetic Analyses of Three Distinct Potassium Conductances in Ventral Cochlear Nucleus Neurons. *Journal of Neurophysiology*, *89*(6), 3083–3096. https://doi.org/10.1152/jn.00126.2002

Rudy B., Maffie J., Amarillo Y., Clark B., Goldbrg E.M., Jeong H.Y., Kruglikov I., Kwon E., Nadal M., Zagha E. (2009) Structure and function of voltage-gated K+ channels: Kv1 to Kv9 subfamilies. *Squire LR, editor. Encyclopedia of neuroscience*, volume 10. Oxford: Academic Press; pp. 397–425.

Rusu, S. I., & **Borst**, J. G. G. (2011). Developmental changes in intrinsic excitability of principal neurons in the rat medial nucleus of the trapezoid body. *Developmental Neurobiology*, *71*(4), 284–295. https://doi.org/10.1002/dneu.20856

Rüttiger, L., Zimmermann, U., & Knipper, M. (2017). Biomarkers for Hearing Dysfunction: Facts and Outlook. *ORL*, *79*(1–2), 93–111. https://doi.org/10.1159/000455705

Salmasi, M., Loebel, A., Glasauer, S., & Stemmler, M. (2019). Short-term synaptic depression can increase the rate of information transfer at a release site. *PLOS Computational Biology*, *15*(1), e1006666. https://doi.org/10.1371/journal.pcbi.1006666

Sätzler, K., Söhl, L. F., Bollmann, J. H., Borst, J. G. G., Frotscher, M., Sakmann, B., & Lübke, J. H. R. (2002). Three-Dimensional Reconstruction of a Calyx of Held and Its Postsynaptic Principal Neuron in the Medial Nucleus of the Trapezoid Body. *The Journal of Neuroscience*, *22*(24), 10567–10579. https://doi.org/10.1523/JNEUROSCI.22-24-10567.2002

Scheffer, D. I., Shen, J., Corey, D. P., & Chen, Z.-Y. (2015). Gene Expression by Mouse Inner Ear Hair Cells during Development. *Journal of Neuroscience*, *35*(16), 6366–6380. https://doi.org/10.1523/JNEUROSCI.5126-14.2015

Schneggenburger, R., Meyer, A. C., & Neher, E. (1999). Released Fraction and Total Size of a Pool of Immediately Available Transmitter Quanta at a Calyx Synapse. *Neuron, 23*(2), 399–409. https://doi.org/10.1016/S0896-6273(00)80789-8

Schneggenburger, R., & **Forsythe**, I. D. (2006). The calyx of Held. *Cell and Tissue Research*, *326*(2), 311–337. https://doi.org/10.1007/s00441-006-0272-7

Sergeyenko, Y., Lall, K., Liberman, M. C., & Kujawa, S. G. (2013). Age-Related Cochlear Synaptopathy: An Early-Onset Contributor to Auditory Functional Decline. *Journal of Neuroscience*, *33*(34), 13686–13694. https://doi.org/10.1523/JNEUROSCI.1783-13.2013

Simon, H., Frisina, R. D., & Walton, J. P. (2004). Age reduces response latency of mouse inferior colliculus neurons to AM sounds. *The Journal of the Acoustical Society of America*, *116*(1), 469–477. https://doi.org/10.1121/1.1760796

Smith, P. H., Joris, P. X., Carney, L. H., & Yin, T. C. T. (1991). Projections of physiologically characterized globular bushy cell axons from the cochlear nucleus of the cat. *The Journal of Comparative Neurology*, *304*(3), 387–407. https://doi.org/10.1002/cne.903040305

Smith, P. H., Joris, P. X., & Yin, T. C. T. (1993). Projections of physiologically characterized spherical bushy cell axons from the cochlear nucleus of the cat: Evidence for delay lines to the medial superior olive. *The Journal of Comparative Neurology*, *331*(2), 245–260. https://doi.org/10.1002/cne.903310208

Sonntag, M., Englitz, B., Typlt, M., & Rubsamen, R. (2011). The Calyx of Held Develops Adult-Like Dynamics and Reliability by Hearing Onset in the Mouse In Vivo. *Journal of Neuroscience*, *31*(18), 6699–6709. https://doi.org/10.1523/JNEUROSCI.0575-11.2011

Spirou, G. A., Rager, J., & Manis, P. B. (2005). Convergence of auditory-nerve fiber projections onto globular bushy cells. *Neuroscience*, *136*(3), 843–863. https://doi.org/10.1016/j.neuroscience.2005.08.068

Steinert, J. R., Robinson, S. W., Tong, H., Haustein, M. D., Kopp-Scheinpflug, C., & Forsythe, I. D. (2011). Nitric Oxide Is an Activity-Dependent Regulator of Target Neuron Intrinsic Excitability. *Neuron*, *71*(2), 291–305. https://doi.org/10.1016/j.neuron.2011.05.037

Stockard, J.J., Stockard, J.E., Sharbrough, F.W., (1978). Nonpathologic Factors Influencing Brainstem Auditory Evoked Potentials. *American Journal of EEG Technology, 18*(4), 177–209. https://doi.org/10.1080/00029238.1978.11106793

Surmeier, D. J., & **Foehring**, R. (2004). A mechanism for homeostatic plasticity. *Nature Neuroscience*, *7*(7), 691–692. https://doi.org/10.1038/nn0704-691

Taberner, A. M., & **Liberman**, M. C. (2005). Response Properties of Single Auditory Nerve Fibers in the Mouse. *Journal of Neurophysiology*, *93*(1), 557–569. https://doi.org/10.1152/jn.00574.2004

Tritsch, N. X., Yi, E., Gale, J. E., Glowatzki, E., & Bergles, D. E. (2007). The origin of spontaneous activity in the developing auditory system. *Nature, 450*(7166), 50–5. https://doi.org/10.1038/nature06233

Trussell, L. O. (1999). Synaptic mechanisms for coding timing in auditory neurons. *Annual Review of Physiology*, *61*(1), 477–496. https://doi.org/10.1146/annurev.physiol.61.1.477

Valenzuela, D.M., Murphy, A.J., Frendewey, D., Gale, N.W., Economides, A.N., Auerbach, W., Poueymirou, W.T., Adams, N.C., Rojas, J., Yasenchak, J., Chernomorsky, R., Boucher, M., Elsasser, A.L., Esau, L., Zheng, J., Griffiths, J.A., Wang, X., Su, H., Xue, Y., Dominguez, M.G., Noguera, I., Torres, R., Macdonald, L.E., Stewart, A.F., DeChiara, T.M., Yancopoulos, G.D. (2003). High-throughput engineering of the mouse genome coupled with high-resolution expression analysis. *Nature Biotechnology, 21*(6), 652–659. https://doi.org/10.1038/nbt822

Vega-Saenz de Miera, E., Lau, D. H. P., Zhadina, M., Pountney, D., Coetzee, W. A., & Rudy, B. (2001). KT3.2 and KT3.3, Two Novel Human Two-Pore K $^{+}$ Channels Closely Related to TASK-1. *Journal of Neurophysiology*, *86*(1), 130–142. https://doi.org/10.1152/jn.2001.86.1.130

von Gersdorff, H., & **Borst**, J. G. G. (2002). Short-term plasticity at the calyx of held. *Nature Reviews Neuroscience*, *3*(1), 53–64. https://doi.org/10.1038/nrn705

Wang, L.-Y., Gan, L., Forsythe, I. D., & Kaczmarek, L. K. (1998). Contribution of the Kv3.1 potassium channel to high-frequency firing in mouse auditory neurones. *The Journal of Physiology, 509*(1), 183–194. https://doi.org/10.1111/j.1469-7793.1998.183bo.x

Wang, Y., & **Manis**, P. B. (2008). Short-Term Synaptic Depression and Recovery at the Mature Mammalian Endbulb of Held Synapse in Mice. *Journal of Neurophysiology*, *100*(3), 1255–1264. https://doi.org/10.1152/jn.90715.2008

Wang, Y., O'Donohue, H., & Manis, P. (2011). Short-term plasticity and auditory processing in the ventral cochlear nucleus of normal and hearing-impaired animals. *Hearing Research*, *279*(1–2), 131–139. https://doi.org/10.1016/j.heares.2011.04.018

Wang, F., Flanagan, J., Su, N., Wang, L.-C., Bui, S., Nielson, A., Wu, X., Vo, H.-T., Ma, X.-J., & Luo, Y. (2012). RNAscope. *The Journal of Molecular Diagnostics, 14(*1), 22–29. https://doi.org/10.1016/j.jmoldx.2011.08.002

Warrier, C., Wong, P., Penhune, V., Zatorre, R., Parrish, T., Abrams, D., & Kraus, N. (2009). Relating Structure to Function: Heschl's Gyrus and Acoustic Processing. *Journal of Neuroscience*, *29*(1), 61–69. https://doi.org/10.1523/JNEUROSCI.3489-08.2009

Warth, R., Barriere, H., Meneton, P., Bloch, M., Thomas, J., Tauc, M., Heitzmann, D., Romeo, E., Verrey, F., Mengual, R., Guy, N., Bendahhou, S., Lesage, F., Poujeol, P., & Barhanin, J. (2004). Proximal renal tubular acidosis in TASK2 K+ channel-deficient mice reveals a mechanism for stabilizing

bicarbonate transport. *Proceedings of the National Academy of Sciences*, *101*(21), 8215–8220. https://doi.org/10.1073/pnas.0400081101

Wernick, J. S., & **Starr**, A. (1968). Binaural interaction in the superior olivary complex of the cat: An analysis of field potentials evoked by binaural-beat stimuli. *Journal of Neurophysiology*, *31*(3), 428–441. https://doi.org/10.1152/jn.1968.31.3.428

Williams, S., Bateman, A., & O'Kelly, I. (2013). Altered Expression of Two-Pore Domain Potassium (K2P) Channels in Cancer. *PLoS ONE*, *8*(10), e74589. https://doi.org/10.1371/journal.pone.0074589

Wilson, G. W., & **Garthwaite**, J. (2010). Hyperpolarization-activated ion channels as targets for nitric oxide signalling in deep cerebellar nuclei: NO and HCN channel function in deep cerebellar nuclei. *European Journal of Neuroscience*, *31*(11), 1935–1945. https://doi.org/10.1111/j.1460-9568.2010.07226.x

Wimmer, V. C., Nevian, T., & Kuner, T. (2004). Targeted in vivo expression of proteins in the calyx of Held. *Pflügers Archiv - European Journal of Physiology*. https://doi.org/10.1007/s00424-004-1327-9

Wolter, S., Möhrle, D., Schmidt, H., Pfeiffer, S., Zelle, D., Eckert, P., Krämer, M., Feil, R., Pilz, P. K. D., Knipper, M., & Rüttiger, L. (2018). GC-B Deficient Mice With Axon Bifurcation Loss Exhibit Compromised Auditory Processing. *Frontiers in Neural Circuits*, *12*, 65. https://doi.org/10.3389/fncir.2018.00065

Wright, S. H. (2004). Generation of resting membrane potential. *Advances in Physiology Education*, *28*(4), 139–142. https://doi.org/10.1152/advan.00029.2004

Wu, S.H., & **Oertel**, D. (1984). Intracellular injection with horseradish peroxidase of physiologically characterized stellate and bushy cells in slices of mouse anteroventral cochlear nucleus. *The Journal of Neuroscience*, *4*(6): 1577–1588. https://doi.org/10.1523/jneurosci.04-06-01577.1984

Wu, S.H. & **Oertel**, D. (1987) Maturation of synapses and electrical properties of cells in the cochlear nuclei. *Hearing Research, 30*(1), 99–110. https://doi.org/10.1016/0378-5955(87)90187-0

Wu, S. H., & **Kelly**, J. B. (1993). Response of neurons in the lateral superior olive and medial nucleus of the trapezoid body to repetitive stimulation: Intracellular and extracellular recordings from mouse brain slice. *Hearing Research, 68*(2), 189–201. https://doi.org/10.1016/0378-5955(93)90123-i

Yang, H., & **Xu-Friedman**, M. A. (2008). Relative Roles of Different Mechanisms of Depression at the Mouse Endbulb of Held. *Journal of Neurophysiology*, *99*(5), 2510–2521. https://doi.org/10.1152/jn.01293.2007

Yang, H., & **Xu-Friedman**, M. A. (2009). Impact of Synaptic Depression on Spike Timing at the Endbulb of Held. *Journal of Neurophysiology*, *102*(3), 1699–1710. https://doi.org/10.1152/jn.00072.2009

Yang, X., Cao, P., & Sudhof, T. C. (2013). Deconstructing complexin function in activating and clamping Ca2+-triggered exocytosis by comparing knockout and knockdown phenotypes. *Proceedings of the National Academy of Sciences*, *110*(51), 20777–20782. https://doi.org/10.1073/pnas.1321367110

Zook, J. M., & **DiCaprio**, R. A. (1988). Intracellular labeling of afferents to the lateral superior olive in the bat Eptesicus fuscus. *Hearing Research*, *34*(2): 141–147. https://doi.org/10.1016/0378-5955(88)90101-3

Zuzarte, M., Heusser, K., Renigunta, V., Schlichthörl, G., Rinné, S., Wischmeyer, E., Daut, J., Schwappach, B., & Preisig-Müller, R. (2009). Intracellular traffic of the K^+ channels TASK-1 and TASK-3: Role of N- and C-terminal sorting signals and interaction with 14-3-3 proteins: Intracellular traffic of TASK-1 and TASK-3. *The Journal of Physiology*, *587*(5), 929–952. https://doi.org/10.1113/jphysiol.2008.164756

Acknowledgements

First, I would like to thank Prof. Dr. Thomas Kuner for giving me the opportunity to conduct my dissertation in his laboratory and providing all the equipment needed to complete this project.

In particular, I would like to thank Dr. Christoph Körber for providing this interesting project. Working on this project has advanced my scientific, and above all, my personal development. Furthermore, I am very grateful for the supervision, guidance and all the fruitful discussions during the course of this research.

I am grateful to all members of the DFG Priority Programme 1608 for funding and especially for making it possible to collaborate with Prof. Dr. Lukas Rüttiger, whom I am very grateful for the help with the hearing assessments.

I would also like to thank Prof. Dr. Christoph Schuster, Prof. Dr. Stephan Frings and Dr. Kevin Allen for agreeing to be members in my committee and for participating in the evaluation of this thesis.

Many thanks to Claudia Kocksch, Michaela Kaiser, Marion Schmitt and Gerald Bendner for excellent technical support. Furthermore, I want to thank Claudia, Michaela and Marion for the stimulating conversations and advices during the last years. A big thank you to Ursel Lindenberger for her administrative work. I also would like to thank all the former and current members in the Kuner lab for creating a great working atmosphere.

I am especially grateful for the friendships I made in the course of the PhD thesis. Maja, Areej, Rafaela and Sailaja, I want to thank you guys for the great lab-time together, for all the laughs, for the support, for having an open ear for my worries and problems and for the fun time outside of lab.

Lastly, my biggest and most important thanks go to my parents and sister, who are always there for me, even during my grumpy moments. There are not enough words to thank you for your constant support and love.